FORENSIC APPLICATIONS OF RAMAN SPECTROSCOPY

Grant Thomson

Submitted in accordance with the requirements for the degree of Doctor of Philosophy.

The University of Leeds,
Department of Physics and Astronomy,
Molecular Physics and Instrumentation Group.

September 2002

The candidate confirms that the work submitted is his own and that appropriate credit has been given where reference has been made to the work of others.

ACKNOWLEDGEMENTS

I wish to thank the following;

- My supervisors Professor David Batchelder and Professor Richard Lacey.
- My parents, family and friends for their support.
- Professor Ewan Smith, Ruth Kier, Calum McHugh, Clare Mclaughlin, Ailie McCabe and Gareth Codd at the Strathclyde University, Pure and Applied Chemistry Department for their contributions to the SERRS projects.
- All and sundry at Renishaw Spectroscopy Products Division. Principally Professor David Pitt, Dr. Bob Bennet, Dr. Brian Smith, Dr. David Cutler, Dr. Ian Hayward and Dr. Mike Claybourne.
- Dr. Kurt Baldwin, for our many reviews on the meaning of life, the importance of copious amounts of beer and women, and his monumental efforts in reviewing this work.
- Denise McKeown, Sandra McAskill, Sarah Lamping and Dr. Tracy Hart for their support whilst I stayed at PSDB.
- Redwood for the gaming masterpiece that is Command & Conquer; Red Alert, and anyone who dared play into the early hours of cold, dark Saturday mornings against me.

ABSTRACT

The forensic applications of Raman spectroscopy have been explored and extended using the development of novel sampling techniques and task-specific instrumentation described in this thesis.

The phenomenon of Raman scattering, enhanced Raman scattering and their relevance in forensic investigations was reviewed. Particular emphasis was placed on current applications, experimental considerations relevant to in-situ Raman sampling and the deficiencies of instrumentation commercially available at the time. It was concluded that the development of novel, optimised instrumentation was essential in the application of Raman spectroscopy to portable forensic applications.

The feasibility of achieving molecularly-specific and sensitive detection of TNT vapour using waveguide-enhanced, surface-enhanced resonance Raman spectroscopy was investigated using reference spectra measured using a calibrated optical system provided by a collaborator. Improvements in signal-to-noise ratio afforded by employing waveguide-enhanced sampling, higher excitation power, long integration times and an improved spectrometer design were modelled, experimentally verified, and used to predict a detection limit of 10^{-16}g for saturated vapour-phase TNT. The theoretical performance of the optical instrument is described and verified using experimentally measured data.

The feasibility of conducting specific and sensitive long-range stand-off covert observation operations against unsuspecting targets in compliance with the UK Regulation of Investigative Powers act was established using a task-optimised laboratory simulation. Using a 5mW visible excitation, short integration times (under 20s) and multiplex detection it was possible to detect and identify a tagged object from a range of up to 50m. The feasibility study yielded a robust prototype handheld system comprising a modified telephoto camera with the integrated

capability of sample discrimination using Raman spectroscopy. The instrument design is described.

CONTENTS PAGE

LIST OF ILLUSTRATIVE MATERIAL

LIST OF TABLES

LIST OF ABBREVIATIONS AND PARAMETERS

Parameter	Definition/ Abbreviation
Chapter 2	
P	Transition dipole moment
β	Hyper-polarisability
χ	Second-order hyper-polarisability
ω	Angular frequency of electric field
θ	Angle between dipole axis and point at r
ε_0	Permittivity of free space
c	Light velocity in vacuum
r	Distance of point from dipole
$\Im$	Average value of Poynting vector
Φ	Power
d	Average diameter of molecular dipole
E	Magnitude of incident electric field & energy density
ν	Frequency of incident electric field
ν_k	Vibrational frequency of k^{th} normal vibrational mode
α	Molecular polarisability
N	Number of atoms comprising sample molecule
Q_k	Vibrational coordinate of normal vibrational mode
ϕ	Vibrational wavefunction
Θ	Rotational wavefunction
a	Mean polarisability
γ	Anisotropy
σ	Scattering cross section
Chapter 3	
α_{ex}	Sample linear absorptivity at excitation wavelength
α_k	Sample linear absorptivity at Raman-shifted wavelength
d	Sample path length
n_R	Sample refractive index at Raman-shifted wavelength
Q	Internal field factor
Ω	Solid angle of microscope objective collection aperture
τ	Instrument transmissivity
L_R	Source radiance
N_{dark}	Dark noise
J_D	Dark current density
A_D	Pixel area

T_{int}	Integration time
q	Electron charge in coulombs
k	Boltzmann's constant
N_{read}	Read noise
N_{ADC}	Quantisation noise
U_{lim}	Maximum detector sampling spatial frequency
D_{pixel}	Pixel width in dispersive axis
MTF	Modulation transfer function
CTE	Charge transfer efficiency
DIFF	Diffusivity
α_{abs}	Silicon absorption coefficient
L_D	Diffusion length
N_{TRANS}	Number of charge transfers
β	Spectral width of spectral feature
$\Delta\beta$	Spectral bandwidth of detector element
Δx	Pixel width (D_{pixel})
x	Image width of spectral feature

Chapter 5

A	Optical fibre core area
NA	Numerical aperture
ϕ	Laser power
τ	Integration time
$\Delta\beta$	Pixel bandwidth
MTF	Modulation transfer function
u	Object distance
v	Image distance
f	lens focal length
D	Camera lens aperture diameter
M	Magnification

Chapter 1

Forensic Applications of Raman Spectroscopy

1.1 Introduction

The Explosives, Weapons and Drugs Department (EWD) of the Police Science Development Branch (PSDB) was established following an escalation in terrorist violence on the UK mainland during the 1980's. As an executive branch of the Home Office, UK, the primary aim of the group is to research and improve technologies used to detect and identify explosives, weapons and drugs in real-world situations and to advise the bodies responsible for the requisition of instrumentation suited for forensic investigation and public safety.

The detection of explosive materials and illicit materials is an extremely relevant analytical problem requiring highly sensitive and specific methods for its solution. Explosives must be detected at ultra-low levels and are often present within complex matrices, which must not affect the detection of the explosive. Highly specific techniques are also essential in preventing illicit materials being concealed using masking materials or confused with legitimate materials. The in-situ, non-destructive identification of illicit materials at a crime scene is becoming increasingly important in the successful prosecution of criminals.

At the time this project began (1998), the application of Raman spectroscopy to forensically-interesting applications was limited to laboratory-based projects, such as the analysis of paint chips and gun-shot residues taken from crime scenes. Most commercially-available instruments were research-grade systems, requiring a dedicated laboratory, and skilled operators. At the time only one commercial source claimed to provide a field-portable Raman spectrograph[1-2].

The use of 1064nm-wavelength excited FT-Raman spectroscopy was reported in the identification of military grade explosives[3]. Subsequent papers have reported Raman spectra from an increased range of materials including explosives[4-10], clothing fibres[11], gunshot residues[12-13], narcotics[14-15], by-products of explosive and narcotic manufacture[16], metabolites of narcotic ingestion[17], chemical weapons[18-19], poisons[20], hair[21], lipsticks[22] and forged documents[23]. Novel sampling techniques and the recent development of compact, low-power, laser sources have enabled Raman to be deployed as an in-situ diagnostic technique[24-27]. Raman spectroscopy is ideally suited to the field of forensic investigation for the following reasons;

- Raman spectroscopy enables the highly specific discrimination between different molecules using their distinct molecular characteristics.

- Raman spectra can be acquired from forensically interesting materials in very short experimental time without sample preparation. Non-fluorescing samples

may be identified in seconds at the crime-scene using low-power, near-infrared, air-cooled lasers.

- Raman spectroscopy is an optical technique, with spectral features that are generally invariant under different laser excitations for transparent samples. Excitation using a visible laser can be used to probe samples wrapped in optically-transparent packaging. Evidence gathered from the crime scene can be placed within tamper-evident bags and studied without opening them. This aids the prosecution process.

- Raman spectroscopy is generally a non-destructive form of testing and leaves the sample invariant.

- Excitation can be delivered to the sample using a microscope. Individual particles with diameters in the sub-micron range can be investigated.

- A Raman spectrometer can be coupled to a confocal microscope to enable depth profiling through a sample. This enables, for example, an investigation of layers of paint obtained from cars or ink layers in suspect documents.

- Excitation can be delivered to, and collected from, the sample using optical fibres. This enables the study of in-situ samples buried in confined spaces.

- The instrumentation requires only electrical power and does not require expendable fuel items such as an inert carrier gas, or liquid nitrogen cooling. The instrumentation is physically robust and could be used in a portable application.

The application of Raman spectroscopy to forensic applications is however encumbered by several fundamental issues.

- The scattering cross-section of the Raman effect is weak compared to fluorescence and UV absorption. A combination of high excitation power and a sensitive, thermoelectrically-cooled detector is required to enable the detection of Raman spectra in short periods. The use of a detector, sensitive to the visible spectrum, precludes the use of Raman as a standoff sampling technique using safe excitation sources.

- Certain materials exhibit fluorescence, a non-molecularly specific emission, with an intensity which can be of several orders of magnitude greater than Raman scattering. The intensity of fluorescence, associated with an interferent molecule, may be sufficient to mask the Raman spectrum. The sampling of large volumes of unknown species, contaminated with fluorescence interferants, may prove unfeasible.

The motivation for this thesis stems from the inability of currently available forensic technologies to identify specific materials with an appropriate sensitivity non-destructively. This thesis describes the development of novel Raman instrumentation, specific to well-defined tasks, required to complement or extend the capabilities of the current framework of technologies used with forensic applications. The justification of the work detailed in this thesis must be reflected by the number of portable Raman-forensic analyser instruments which are now commercially-available.

In Chapter 2, the fundamental theory of Raman scattering is reviewed, concentrating on the scattering interaction between molecules and light from a semi-classical model. Non-linear techniques such as Resonance and Surface-Enhanced Raman spectroscopy are described, with particular emphasis placed on the instrumental parameters necessary to perform them.

Chapter 3 identifies the technical challenges that have historically prevented Raman spectroscopy from realising its potential as an in-situ non-destructive sample analyser. The core developments of Raman instrumentation are reviewed from this perspective. Each project undertaken in this thesis was subjected to a preliminary period of feasibility testing. With little information available in the literature concerning the scattering efficiencies of forensically-interesting materials, preliminary testing was performed using a Renishaw System 1000 Raman Microscope. The signal-to-noise ratio of measurements obtained from such testing were appropriately modified to

simulate conditions expected from novel instrument designs. Chapter 3 presents an appraisal of these instruments, and expands upon the use of alternative components that could improve their sensitivity. A review of commercially-available portable Raman instrumentation is presented, which identifies the limitations of the technology and justifies the development of novel instrumentation. The development of miniaturised instruments, specific to a well-defined task, is the primary focus of this thesis.

In Chapter 4, the development of a TNT explosive vapour-phase detector based on the use of Surface Enhanced Resonance Raman spectroscopy (SERRS) is described. The characterisation of parameters important to the design of a wet-chemistry flow cell, incorporating a Teflon AF liquid-core optical waveguide to maximise the sample volume, is described. An instrument design is presented, corresponding to the evolution of technology during the period of this investigation and are compared.

In Chapter 5, the feasibility of detecting and identifying a highly-scattering, SERRS-active, proprietary dye at long stand-off distance is presented. The dependence of spectral signal-to-noise with increased stand-off is modelled and used to predict limits of detection.

The design of alternative instruments, designed and implemented during this project are included in the appendices, in addition to novel developments in Raman sampling.

1.2 References

1. OceanOptics, RS 2000 Raman Spectrograph

2. R.H. Clarke, S. Londe, W.R. Premasiri, Journal of Raman Spectroscopy, 1999, Volume 30, pp 827-832.

3. J. Akhavan, Spectrochimica Acta 1991, Volume 47A, No. 9/10 pp 1247-1250.

4. P.C. White, Scientific Justice, 2000, Volume 40, pp 113-119.

5. C.M. Hodges, J. Akhaven, Spectrochimica Acta, 1990, Volume 46, pp 303-307.

6. H.S. Sands, I.P. Hayward, T.E Kirkbride, Journal of Forensic Science, 1998, Volume 43, pp 509-513.

7. N. Gupta, R. Dahmani, Spectrochimica Acta A, 2000, Volume 56, pp 1453-1456.

8. D.N. Batchelder, C. Cheng, I.P. Hayward, The Proceedings of Contraband and Cargo Inspection Technology, Washington DC, 1992, pp 73-75.

9. C. Cheng, T.E Kirkbride, D.N. Batchelder, Journal of Forensic Science, 1995, Volume 40, pp 31-37.

10. K. McNesby, J.E. Wolfe, J.B. Morris, Journal of Raman Spectroscopy, 1994, Volume 25, pp 75-87.

11. I.P. Keen, G.W White, P.M. Fredericks, Journal of Forensic Science, 1998, Volume 43, pp 82-89.

12. A.H. Kuptsov, Journal of Forensic Science, 1994, Volume 39, pp 305-318.

13. S. Stich, D. Bard, L. Gros L, Journal of Raman Spectroscopy, 1998, Volume 29, pp 787-790.

14. A. G Ryder, G.M O'Connor, T.J Glynn, Journal of Forensic Science, 1999, Volume 44, pp 1013-1019.

15. N.T. Kawai, J.A. Janni, Spectroscopy, 2000, Volume 15 p 32.

16. J.M. Sylvia, J.A. Janni, J.D. Klein, Analytical Chemistry, 2000, Volume 72, pp 5834-5840.

17. X. Dou, Y. Yamaguchi, H. Yamamoto, Vibrational Spectroscopy, 1996, Volume 13, pp 83-89.

18. S. Christensen, K. Kate, The 22nd Army Science Conference, Baltimore, MD, 2000.

19. S. Christensen, B. MacIver, L. Procell, Applied Spectroscopy, 1999, Volume 53, pp 850-855.

20. V.A. Narayanan, N.A Stump, G.D. Del Cul, Journal of Raman Spectroscopy, 1999, Volume 30, pp 435-439.

21. A.S. Wilson, H.G.M. Edwards, D.W. Farwell, et al, Journal of Raman Spectroscopy, 1999, Volume 30, pp 367-373.

22. C. Rodger, V. Rutherford, D. Broughton, Analyst, 1998, Volume 123, pp 1823-1826.

23. M. Claybourne, M. Ansell, Scientific Justice, 2000, Volume 40, pp 261-271.

24. T. Ikeda, H. Tashiro, Y. Ozaki, Institute of Physics Conference Series, 2000, Volume 165, pp 81-82.

25. M.D. Ray, A.J. Sedlacek, M.Wu, Review of Scientific Instruments, 2000, Volume 71, pp 3485-3489.

26. D.L. Dickensheets, D.D. Wynn-Williams, G.M Howell, Journal of Raman Spectroscopy, 2000, pp 633-635.

27. B.M. Cullum, J. Mobley, Z.M. Chi, Review of Scientific Instruments, 2000, Volume 71, pp 1602-1607.

Chapter 2

Light Scattering by Molecules

2.1 Introduction

When light is incident onto a molecule, a small proportion, typically 1 in 10^{10} photons, is inelastically scattered and appears at shifted frequencies. This is the Raman effect.

The first unaccountable observations of the Raman effect were reported by Lommel in 1878 as anomalous fluorescence scattering[1]. Sample-specific bands were identified with a wavenumber shift that was invariant to changes in the excitation wavelength.

The inelastic scattering of light by molecules was predicted in 1923 by Smekal[2]. Prior research using infrared absorption spectroscopy indicated that molecules exhibit a complex and highly specific vibrational fingerprint. It was proposed that the change in molecular polarisability during molecular vibrations would impart ro-vibrationally-specific information to the inelastically scattered light. This was included as a modification to the Kramers-Heisenberg theory of dispersion for molecular scattering phenomena in 1925[3].

The first qualitative observation of inelastic scattering was reported in 1928 by Raman and Krishnan[4]. The first quantitative observations of Raman spectra were reported concurrently by Raman and Krishnan[5], Cabannes[6], Landsberg and Mandelstram[7], and Rocard[8] later that year. The practical implications of Raman spectroscopy as an analytical technique were reviewed in Chapter 1. The fundamental principles of Raman scattering, from the basis of a molecular-electromagnetic field interaction, are presented in this chapter.

2.2 Electric Dipole Scattering

The scattering of light by an anisotropic molecule of average diameter d, when irradiated by a monochromatic electromagnetic field, E, of wavelength, λ, is treated in the Rayleigh regime[9] such that $d \prec \lambda/20$. For small molecules and visible excitation, the electric field intensity is approximately constant across the molecule. The incident electric field polarises molecular charge and induces an oscillating dipole moment, P, according to;

$$P = \alpha \cdot E + \tfrac{1}{2}\beta : EE + \tfrac{1}{6}\chi \vdots EEE \qquad 2.1$$

where α is the molecular polarisability that reflects the ability of the electric field to displace molecular charge. The terms β and χ are higher order hyper-polarisability

tensors that can be ignored under low irradiance. Scattering arising from induced magnetic dipoles and electric quadrupoles is considered negligible.

An oscillating electric dipole, with amplitude p_0, is shown in figure 2.1 in a Cartesian coordinate system with unit vectors **i**, **j**, and **k** along the x, y and z axes exposed to an electric field, Ex.

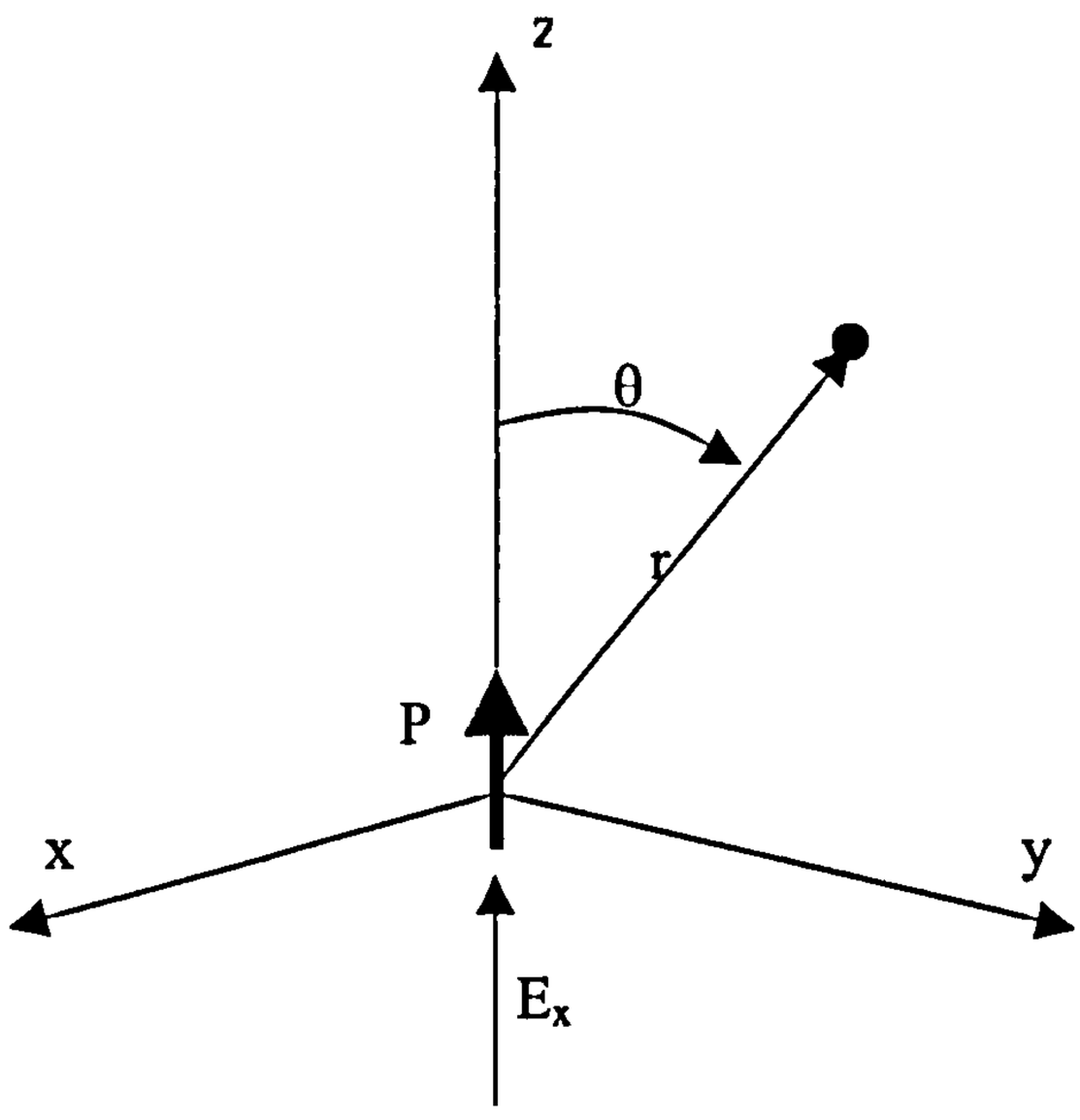

Figure 2.1 Electric dipole source.

The oscillating electric dipole is a source of electromagnetic radiation with electric field intensity, $\underline{E}$, at a point $\underline{r}$, where r is the distance from the dipole and θ is the angle subtended by the dipole axis;

$$E = \frac{-\omega^2 p \sin\theta j}{4\pi\varepsilon_0 c^2 r} \qquad 2.2$$

The instantaneous value of the Poynting vector, $\Im$, the average power per unit area associated with the radially propagating radiation is;

$$\overline{\Im} = \frac{\omega^4 {p_0}^2 \sin^2\theta}{32\pi^2\varepsilon_0 c^3 r^2} \qquad 2.3$$

The average of the Poynting vector may be used to calculate the average power, $d\Phi$, per unit area, dA of a surface using;

$$d\Phi = \left|\overline{\Im}\right| dA$$

$$\Phi = \frac{4\pi^3 c \nu^4 {p_0}^2}{3\varepsilon_0} \qquad 2.4$$

Where ν is the angular frequency of the radiation in absolute wavenumbers. The radiant intensity, I, of the scattering dipole in a particular direction is given by;

$$I = \frac{\pi^2 c \nu^4 {p_0}^2 \sin^2\theta}{2\varepsilon_0} \qquad 2.5$$

In quantum mechanical terms, the transition dipole moment amplitude, P_0, associated with the transition from an initial state i to a final state f, described by the wavefunctions, ψ_i and ψ_f respectively is given by;

$$\left[P_o^{(1)}\right]_{fi} = \langle \psi_f | \alpha | \psi_i \rangle . E_0 \qquad 2.6$$

where the integration is performed over all coordinate space. Because of the vector nature of P and E and the tensor α, the individual components of the dipole moment are given by;

$$\begin{aligned}
\left[P_{x0}\right]_{fi} &= \left\{\left[\alpha_{xx}\right]_{fi} E_{x0} + \left[\alpha_{xy}\right]_{fi} E_{y0} + \left[\alpha_{xz}\right]_{fi} E_{z0}\right\} \\
\left[P_{y0}\right]_{fi} &= \left\{\left[\alpha_{yx}\right]_{fi} E_{x0} + \left[\alpha_{yy}\right]_{fi} E_{y0} + \left[\alpha_{yz}\right]_{fi} E_{z0}\right\} \\
\left[P_{z0}\right]_{fi} &= \left\{\left[\alpha_{zx}\right]_{fi} E_{x0} + \left[\alpha_{zy}\right]_{fi} E_{y0} + \left[\alpha_{zz}\right]_{fi} E_{z0}\right\}
\end{aligned} \qquad 2.7$$

where the components $\left[\alpha_{ij}\right]_{fi}$ are the matrix elements of the polarisability tensor, α, for the transition f↔i and are defined as;

$$\left[\alpha_{xy}\right]_{fi} = \left\langle \psi_f \middle| \alpha_{xy} \middle| \psi_i \right\rangle \qquad \textbf{2.8}$$

The following semi-classical model is based on Placzek's polarisability theory which applies to vibrational and rotational transitions induced by incident radiation in molecules which remain in non-degenerate electronic ground states. Provided the excitation frequency is larger than any vibrational or rotational frequency of the molecule and much smaller than any electronic transition then the molecular wavefunctions ψ may be resolved into a product of vibrational and rotational wavefunctions. Hence equation 2.8 becomes;

$$\left[\alpha_{xy}\right]_{fi} = \left\langle \phi_f \Theta_f \middle| \alpha_{xy} \middle| \phi_i \Theta_i \right\rangle \qquad \textbf{2.9}$$

where ϕ_f, ϕ_i are vibrational wavefunctions and Θ_f and Θ_i are rotational wavefunctions.

The components $\left[\alpha_{xy}\right]$ of the polarisability tensor, described in a laboratory-fixed frame of reference are sensitive to both molecular vibration and rotation. Under rotation of the frame of reference to molecular-fixed coordinate system with x',y',z' the polarisability components are modified according to;

$$\left[\alpha_{xy}\right]_{fi} = \sum_{x'y'} \left\langle \phi_{v^f} \left| \alpha_{x'y'} \right| \phi_{v^I} \right\rangle \left\langle \Theta_{R^f} \left| \cos(xx') \cos(yy') \right| \Theta_{R^I} \right\rangle$$

2.10

where ν^f, ν^I are vibrational quantum numbers, R^f, R^i are rotational quantum numbers and xx', yy' is the angle between two coordinate systems.

Although the tensor components of α are altered on rotation, specific combinations remain invariant. These are the mean polarisability a and anisotropy, γ, defined by;

$$a = \tfrac{1}{3}\left(\alpha_{xx} + \alpha_{yy} + \alpha_{zz}\right)$$

$$\gamma = \tfrac{1}{2}\left\{\left(\alpha_{xx} - \alpha_{yy}\right)^2 + \left(\alpha_{yy} - \alpha_{zz}\right)^2 + \left(\alpha_{zz} - \alpha_{xx}\right)^2 + 6\left(\alpha^2{}_{xy} + \alpha^2{}_{xy} + \alpha^2{}_{xy}\right)\right\}$$

2.11

The tensor $\alpha_{x'y'}$ is a function of vibrational coordinates. In an N-atomic, non-linear molecule, there are $J = 3N - 6$ vibrational degrees of freedom ($J = 3N - 5$ in a linear molecule). Each degree of freedom is described by a vibrational normal mode, K. Each normal mode has a distinct vibrational frequency, ν_k, and a series of vibrational energy levels, separated by energy $\Delta E = h\nu_k$. The relative motions of atoms along the K^{th} normal mode of vibration, from equilibrium position, Q_{eq}, induce a change in $\alpha_{x'y'}$. This may be expanded using a Taylor series;

$$\alpha_{x'y'} = (\alpha_{x'y'})_0 + \sum_k \left(\frac{\partial \alpha_{x'y'}}{\partial Q_k}\right)_0 Q_k + \ldots\ldots \qquad \textbf{2.12}$$

In the electrical and mechanical harmonic oscillator approximation, the induced dipole moment is given by;

$$P(t) = \alpha_0 E_0 \cos(2\pi\nu_0 t) + \sum_{k=1}^{J} \left(\frac{\partial \alpha_{ij}}{\partial Q_k}\right)_0 \cos(2\pi\nu_k t) E_0 \cos(2\pi\nu_0 t) \qquad \textbf{2.13}$$

The first term, scattered at the frequency of the incident radiation, is called Rayleigh scattering. Using the trigonometric substitution, $\cos a \cos b = \frac{1}{2}\{\cos(a+b) + \cos(a-b)\}$, an additional 2J scattering frequencies appear in the second term, accounting for J modes of oscillation, shifted symmetrically about the Rayleigh scattered wavelength. These correspond to Stokes (red-shifted) and anti-Stokes (blue-shifted) scattered radiation respectively. The presence of these additional frequency components is manifest as frequency components in the dipole oscillation and thus as wavelength-shifted, scattered electromagnetic radiation.

The vibrational wavefunctions are expanded into a product of harmonic oscillator wavefunctions for each of the normal vibrational modes. Equation 2.13 becomes;

$$\left[\alpha_{x'y'}\right]_{v^f v^i} = \left(\alpha_{x'y'}\right)_0 \left\langle \prod_k \phi_{v_k{}^f}(Q_k) \middle| \prod_k \phi_{v_k{}^i}(Q_k) \right\rangle + \sum_k \left(\frac{\partial \alpha_{x'y'}}{\partial Q_k}\right)_0 \left\langle \prod_k \phi_{v_k{}^f}(Q_k) \middle| Q_k \middle| \prod_k \phi_{v_k{}^i}(Q_k) \right\rangle$$

where

$$\left\langle \phi v_k{}^f(Q_k) \middle| \phi v_k{}^i(Q_k) \right\rangle = \begin{Bmatrix} 0 \Leftrightarrow v_k{}^f = v_k{}^i \\ 1 \Leftrightarrow v_k{}^f \neq v_k{}^i \end{Bmatrix}$$

$$\left\langle \phi v_k{}^f(Q_k) \middle| Q_k \middle| \phi v_k{}^i(Q_k) \right\rangle = \begin{Bmatrix} 0 \Leftrightarrow v_k{}^f = v_k{}^i \\ \left(v_k{}^i + 1\right)^{\frac{1}{2}} b_{v^k} \Leftrightarrow v_k{}^f = v_k{}^i + 1 \\ \left(v_k{}^i\right)^{\frac{1}{2}} b_{v_k} \Leftrightarrow v_k{}^f = v_k{}^i - 1 \end{Bmatrix}$$

2.14

Rayleigh scattering occurs when the transition begins and ends in the same vibrational state. Raman scattering occurs when the vibrational quantum number changes by unity and also requires $\left(\frac{\partial \alpha_{x'y'}}{\partial Q_k}\right)_0 \neq 0$. The extension of this model to an anharmonic oscillator allows for vibrational state transitions greater than unity.

For a freely rotating sample, comprising an assembly of N freely rotating molecules, the determination of scattering intensities is achieved, ignoring the fine rotational structure,

by averaging over all the possible molecular orientations with respect to the electric field vector.

The intensity of scattered radiation is directly proportional to the square of a space-averaged tensor, $\bar{\alpha}$, which has components;

$$\left[\overline{\alpha_{yx}}\right]^2 = \left[\overline{\alpha_{yz}}\right]^2 = \left[\overline{\alpha_{zx}}\right]^2 = \tfrac{1}{15}\gamma^2$$
$$\left[\overline{\alpha_{xx}}\right]^2 = \left[\overline{\alpha_{yy}}\right]^2 = \left[\overline{\alpha_{zz}}\right]^2 = \tfrac{1}{45}\left(45a^2 + 4\gamma^2\right)$$
$$\left[\overline{\alpha_{xx}\alpha_{yy}}\right] = \left[\overline{\alpha_{yy}\alpha_{zz}}\right] = \left[\overline{\alpha_{zz}\alpha_{xx}}\right] = \frac{45a^2 - 2\gamma^2}{45}$$
$$\left[\overline{\alpha_{xx}\alpha_{xy}}\right] = 0$$

2.15

In the simplified geometry illustrated in figure 2.2, the sample is illuminated along the z-axis and collection is achieved in the y-z scattering plane. This is an approximation; the complications arising from the focussing of the light on the sample are reviewed elsewhere[10].

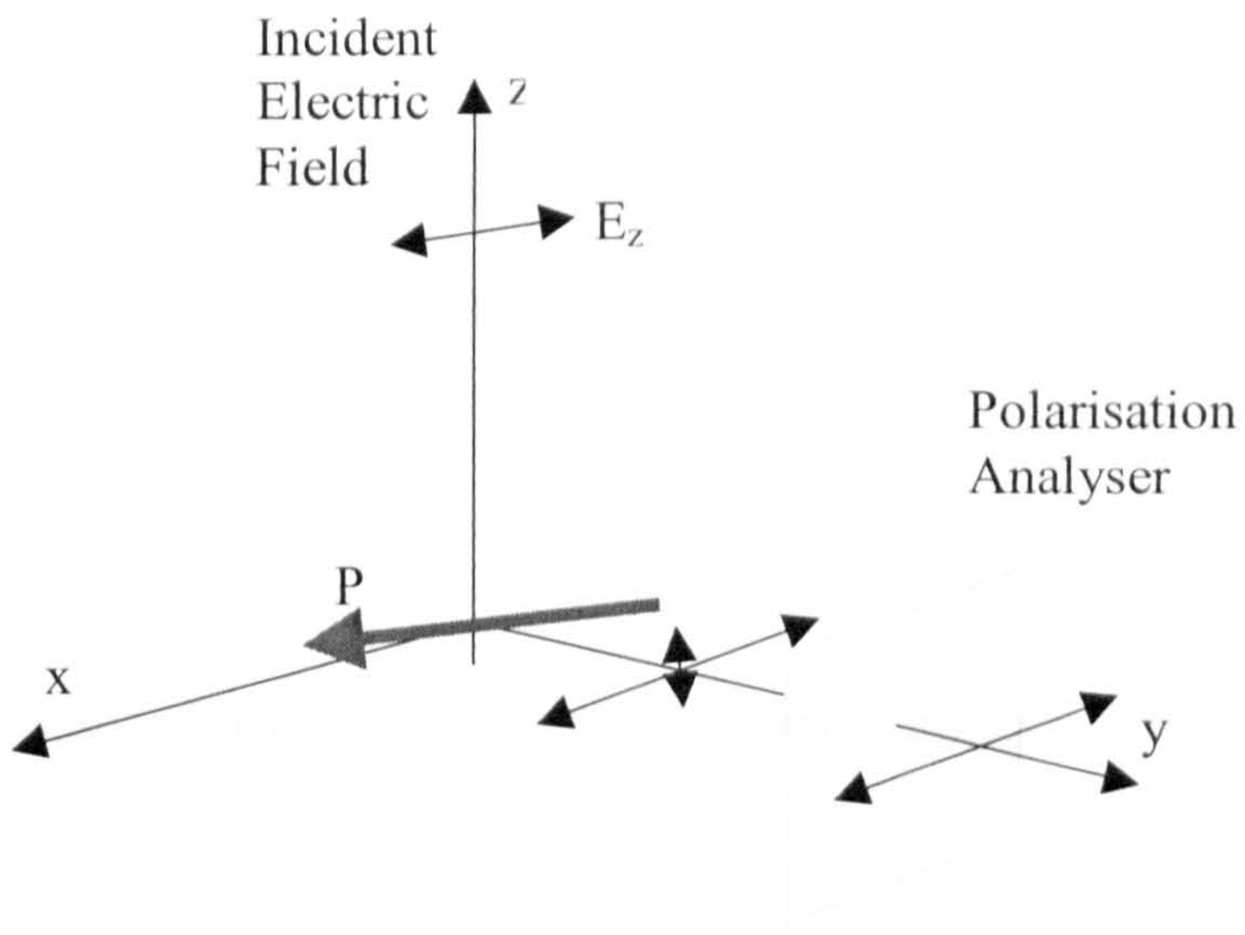

Figure 2.2 Raman scattering from a randomly oriented molecule

The typical space-averaged square of a Stokes transition moment amplitude is given by;

$$\left[\overline{P_{y0}^{(1)}}\right]^2_{v_{k+1}{}^i v_k{}^i} = \left(v_k{}^i + 1\right) b_{v_k}{}^2 \left\{\left(\overline{\alpha'_{yy}}\right)_k^2\right\} E_{y0}{}^2 \qquad \textbf{2.16}$$

Using the squared, space-averaged, derived tensor component and accounting for the Boltzmann distribution of molecules in the sample, the radiant intensity of scattering observed in the y-direction parallel and perpendicularly polarised to the excitation field is;

$$ {}^{I}I_{\parallel}\left(\tfrac{\pi}{2}\right)=\frac{hN(\nu_0-\nu_k)^4(\gamma')^2\Im}{240\varepsilon_0\nu_k'\left(1-\exp\left[\frac{-hc\nu_k}{kT}\right]\right)} $$

$$ {}^{I}I_{\underline{I}}\left(\tfrac{\pi}{2}\right)=\frac{hN(\nu_0-\nu_k)^4\left\{45a_k'^2+4(\gamma')^2\right\}\Im}{720\varepsilon_0\nu_k'\left(1-\exp\left[\frac{-hc\nu_k}{kT}\right]\right)} $$

2.17

The ratio of these intensities is known as the depolarisation ratio, ρ;

$$ \rho=\frac{{}^{I}I_{\parallel}\left(\tfrac{\pi}{2}\right)}{{}^{I}I_{\underline{I}}\left(\tfrac{\pi}{2}\right)}=\frac{3\gamma'^2}{45a'^2+4\gamma'^2} $$

2.18

The symmetry properties of a normal vibration can be determined using the depolarisation ratio. For totally symmetric vibrations, $0\le\rho\le\frac{3}{4}$, and non-totally symmetric vibrations, $\rho=\frac{3}{4}$.

An important consequence of equation 2.17 is that the Raman scattering intensity observes a λ^{-4} dependence and is directly proportional to the number of molecules in the sample. In addition, the scattering intensity observes a temperature dependence. Shifting to shorter wavelengths, particularly in the UV, affords an enhanced scattering compared to infrared excitation.

2.3 Scattering Efficiency

The comparison between Raman and Rayleigh scattering, fluorescence and general absorption, emission processes is achieved using a scattering cross-section, σ, to relate the number of photons, n_p, scattered by a sample to the incident power density, ε;

$$P = \sigma\varepsilon \qquad \textbf{2.19}$$

σ has units of watts/m^2. The differential scattering cross section, $\frac{\partial\sigma}{\partial\Omega}$, relates the scattering cross section to an angular dependence. In a standard Raman experiment, the scattering cross section of a molecule is particularly weak, typically $10^{-29}m^2$. Typical [11] values for Rayleigh and fluorescence range from 10^{-26} - 10^{-19} m^2 respectively.

2.4 Resonance Raman Spectroscopy

When the excitation wavelength approaches that of an electronic transition of a molecule chromophore, then that electronic state submits an enhanced contribution to Raman scattering beyond the usual λ^{-4} dependence. Enhancement factors greater than 10^6 have been reported enabling low concentration samples to be studied[12]. The

relationship between excitation wavelength and the enhancement factor is shown in an excitation plot, which is related to the electronic absorption spectrum of the material.

Resonance Raman (RR) is similar to fluorescence in that a molecule is promoted from a ground to an excited electronic state but differs in that it is a scattering process, with a time scale of the order of 10^{-14}s. In addition to Resonance Raman and fluorescence, the sample can absorb the excitation flux and dissipate it as heat.

There are two types of Resonance Raman Scattering;

- Pre-resonance Raman Scattering; The excitation wavelength lies within the wings of an absorption band.
- Rigorous Raman Scattering; The excitation source wavelength coincides with an absorption vibrational structure of the sample.

The quantum mechanical treatment of conventional Raman scattering (CRS) using the time-independent Kramers-Heisenberg-Dirac relation fails under resonance conditions as the polarisability tensor elements increase without bounds. This was remedied by the addition of a damping term, $i\Gamma$, to the denominators, where Γ represents the width of the absorption band due to the transition to the electronic excited state, ψ_r. The molecular polarisability becomes;

$$\alpha_{ij} = \frac{1}{\hbar}\left\{\frac{\langle\psi_f|P_p|\psi_r\rangle}{\omega_{fr} - \omega_0 - i\Gamma} + \frac{\langle\psi_f|P_p|\psi_r\rangle}{\omega_{fi} + \omega_0 - i\Gamma}\right\} \qquad \textbf{2.20}$$

In the adiabatic Born-Oppenheimer approximation, the eigenfunctions describing the unperturbed molecule are expressed as products of functions of electronic, rotational and vibrational states. Assuming the molecule begins in the ground vibrational state, ψ_I and the Raman transition begins and ends in the ground electronic state, g, then since the electron dipole moment operator, M, acts only on the electronic wavefunction, equation 2.12 becomes[10];

$$\left(\alpha_{xy}\right)_{fi} = A + B + \ldots$$

where $A = \sum_{e,v_e} \frac{M^e{}_{0x} M^e{}_{0y}}{\hbar\omega_{ri} - \hbar\omega_0 - i\Gamma} \langle\psi_f|\psi_e\rangle\langle\psi_e|\psi_i\rangle$

$$B = \sum_{e,v_e} \frac{M^e{}_{0x}\left(\frac{\partial M^e{}_{0y}}{\partial Q}\right)_0}{\hbar\omega_{ri} - \hbar\omega_0 - i\Gamma} \langle\psi_f|\psi_e\rangle\langle\psi_e|Q|\psi_i\rangle + \sum_{e,v_e} \frac{\left(\frac{\partial M^e{}_{0x}}{\partial Q}\right)_0 M^e{}_{0y}}{\hbar\omega_{ri} - \hbar\omega_0 - i\Gamma} \langle\psi_f|Q|\psi_e\rangle\langle\psi_e|\psi_i\rangle \qquad \textbf{2.21}$$

The equation decomposes into expressions involving only vibrational wavefunctions, whilst the electronic wavefunctions are in M^e, which is the pure electronic transition moment connecting the ground state with the electronic excited state.

M^e, a function of nuclear coordinate, is expanded into a Taylor series about the equilibrium position. The numerator of the A-term comprises the product of the electronic transition moment, $M^e_{0,}$, and the product of the two vibrational overlap integrals. This implies that the A-term scattering predominates over B-term scattering for symmetric vibrations where the equilibrium position of the excited state is displaced relative to the ground state. For other vibrational modes, the A-term vanishes.

Enhancement via B-term scattering occurs for non-totally symmetric vibrations occurring between two electronic excited states. It's numerator comprises Q-dependent vibration overlap integrals such that, even for undisplaced excited geometry, it is non vanishing. In addition, comprises a vibronic coupling Hamiltonian. This is non-vanishing if normal coordinates of the proper symmetry are chosen.

2.5 Surface Enhanced Raman Scattering (SERS) and Surface Enhanced Resonance Raman Scattering (SERRS)

The anomalous scattering intensity of pyridine adsorbed onto an electrochemically roughened silver electrode surface was reported in 1974[13]. The observed spectra were

ascribed to that of the adsorbed pyridine since the vibrational band positions were slightly shifted with respect to the bulk free spectra. Although originally attributed to an increased surface concentration of pyridine, subsequent studies[14,15] identified an increase in the Raman scattering cross section by 4-5 orders of magnitude.

SERS has been reported from a wide range of metals, principally the noble metals; gold, silver and copper. In all instances, a well defined metal structure is required. Typical SERS substrates include;

- Mechanically and electrochemically roughened surfaces.[16,17,18]
- Vacuum deposited metallic films on insulating surfaces.[19,20,21,22]
- Laser ablation of metal surfaces into solution.[23]
- Lithographically etched surfaces such as island posts and grating structures.[24]
- Colloidal suspensions of metal particles produced by chemical reduction.[25,26,27]

The emphasis in this thesis is on the use of colloidal suspensions of silver nanoparticles. The interest in SERS originates from the molecular-specificity that arises from spectra that can be obtained at low concentrations. The detection of a single molecule of a Cyanine dye in silver colloid has been reported[28]. In addition, SERS offers experimental advantages over CRS:[29,30,31]

- Energy transfer processes between the adsorbate and the metal structure efficiently quench fluorescence that otherwise obscures Raman spectra.
- The technique affords selectivity from adsorbed molecules in the presence of a bulk material.
- Selection rules for SERS are relaxed from CRS. Vibrational bands are observed in the adsorbed species that are not present in the free material. This is a short-range effect.
- SERS is strongly depolarised, even for vibrational bands that are highly polarised in the free material.
- Overtones are weak or not typically observed in SERS.
- SERS excitation spectra exhibit broad resonances.

The development of SERS as a quantitative analytical technique is limited by the variation in band intensities due to orientation effects of the adsorbate at the sample surface and the surface structure repeatability. In the context of colloidal substrates, the sample is also often found to induce concentration-dependent colloid aggregation, which alters the enhancement factor. Linearity of response with sample concentration is typically limited to 2 to 3 decades of concentration.

When the excitation wavelength is in resonance with an electronic transition of the adsorbate, an additional enhancement is observed. This is the Surface Enhanced

Resonance Raman effect (SERRS). Both resonance and surface enhanced Raman scattering processes occur in SERRS, but they are not independent factors.

2.5.1 Surface Enhancement Theory

The origins of SERS and SERRS spectroscopy have been the subject of many debates. The intensity of Raman scattering is directly proportional to the square of the product of the molecular polarisability and the electric field strength. Surface enhancement is attributed to an enhancement of either or both of these parameters. Enhancement models are divided into electromagnetic[31-35] and chemical charge-transfer mechanisms[36-37] according to which parameter is enhanced.

Electromagnetic interactions between the molecule and substrate are believed to play a major role in SERS. These propose a resonant interaction between the electromagnetic field and surface plasmon-polariton type resonances on a non-flat metal surface. A surface plasmon is a wave of charge oscillation on the surface of a conductive particle. At the plasmon resonance frequency, the metal particle becomes highly polarisable, resulting in large field-induced polarisation and large localised fields. A molecule placed at the metal surface or in close proximity experiences an enhanced electromagnetic field. This increases the Raman scattering intensity, which additionally excites further surface plasmons.

SERS enhancement factors have been presented for a variety of structured systems, including single particles, considering principally the dipole-mode excitation of the particles. Further models account for the rigorous consideration of all modes. Systems involving a plurality of structured systems involving particles, regularly repeating structures such as islands and grating structures have similarly been presented.

In the simplest system[31], a single metal particle of diameter, d, and dielectric constant $\varepsilon(\omega)$, is considered with a Raman scattering molecule in close proximity as shown in figure 2.3. The system is embedded in a medium of dielectric constant ε_0. In the Rayleigh limit, the primary exciting field, $E(\omega_0, r)$, for a Raman scatterer at a point r from the centre of the sphere is given by the sum of the incident field E_i and the field of a dipole, $P(\omega_0)$ induced at the sphere centre. The dipole is given;

$$P(w_0) = \left(\frac{d}{2}\right)^3 g_0 E(w_0, r)$$

where $g_0 = \dfrac{\dfrac{\varepsilon(w_0)}{\varepsilon_0(w_0) - 1}}{\varepsilon_0(w_0) + 2}$ **2.22**

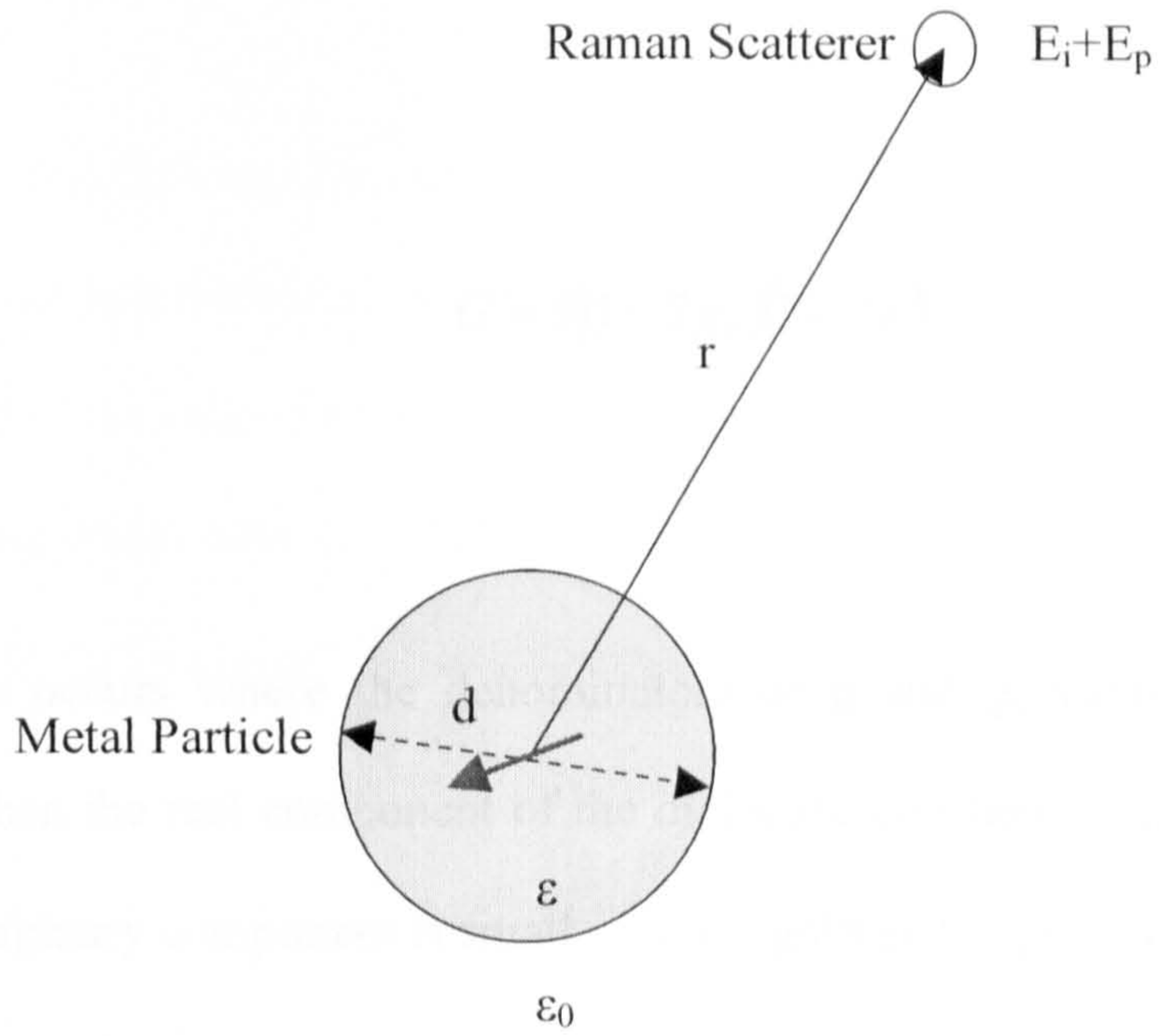

Figure 2.3 Small particle approximation for SERS

The primary field forces the charge in the molecule at r to oscillate at a Raman shifted frequency, ω_s, where $\omega_s=\omega_0\pm\omega_k$, with a dipole moment, $P(\omega_s)$. The total Raman emission is given by the coherent addition of the field of $P(\omega_S)$ and a dipole P located at the sphere centre.

$$g=\frac{\dfrac{\varepsilon(w)}{\varepsilon_0(w)-1}}{\dfrac{\varepsilon(w)}{\varepsilon_0(w)+2}} \qquad \textbf{2.23}$$

where E is the field of $P(\omega)$ at the sphere centre and $P(\omega)$ represents the "antennae effect" of the sphere. The enhancement factor, G, for an adsorbed molecule and under the most favourable conditions, is given;

$$G = 5\left|(1+2g_0)(1+2g)\right|^2 \qquad 2.24$$

Resonance occurs where the denominators of g and g_0 vanish. This condition is fulfilled when the real component of the dielectric constant of the metal is equal to –2 and the imaginary component is small. Silver, gold and copper fulfil these conditions at visible frequencies.

This model implies that the magnitude of enhancement falls for high frequency molecular vibrations, which fall out of resonance with the surface plasmons. In colloidal suspensions, aggregation extends the collective plasmon resonance into the near infrared and so this effect is reduced.

Particle shape has been found to be extremely relevant in the determination of enhancement factors. Highly prolate and oblate particles give rise to greater enhancements[38]. Other types of electromagnetic enhancement include the "lightning rod effect", caused by highly needle-shaped particles, vary the resonant frequency. Polarisation of the surface by dipole induced fields in adsorbed molecules, the image effect and Fresnel reflection effects are other electromagnetic effects proposed to afford enhancement.

The chemical effect was first used by Billman to explain SERS via an enhancement of the molecular polarisability. It was proposed that enhancement could only occur when an adsorbate molecule adsorbed to a feature of atomic scale roughness[36]. The chemical effect is associated with the overlap of metal and adsorbate electronic wav efunctions, leading to ground state and light-induced charge transfer processes.

The polarisability of the adsorbate molecule is increased due to an interaction with the metal surface. Complexation of the adsorbate with the surface occurs via adatoms or clusters of particles and implies a short-range interaction. An electron from the metal tunnels into the charge-transfer excited state of the adsorbed molecule. The resulting negative ion has different equilibrium geometry from the original neutral adsorbate. The electron returns to the metal, which leads to a vibrationally excited neutral molecule and emission of Raman scattered light.

The reader is referred to the literature reviews for a more comprehensive explanation[38].

2.6 References

1. E. Lommell, Wiedemanns Annual de Physique, 1878, Volume 3, p 251.

2. A. Smekal, Naturwiss, 1923, Volume 11, p 873.

3. H.A. Kramers, W. Heisenberg, Zeitshift Physik, 1925, Volume 31, p 681.

4. C.V. Raman, K.S. Krishnan, Nature, 1928, Volume 121, p501.

5. C.V. Raman, K.S. Krishnan, Indian Journal of Physics, 1928, Volume 2, p 387.

6. J. Cabannes, Compte Rendu Academy of Science (Paris), 1928, Volume 186, p 1201.

7. G. Landsberg, L. Mandelstam, Naturwiss, 1928, Volume 16, p 557-772.

8. Y. Rocard, Compte Rendu Academy of Science (Paris), 1928, Volume 186, p 1107.

9. D.A. Long, *Raman Spectroscopy,* McGraw-Hill International Book Company, London, UK, 1977.

10. B. Schrader, *Infrared and Raman Spectroscopy,*VCH Verlagsgellschaft mbH, Cambridge, UK, 1995.

11. C.L. Stevenson, T. Vo-Dinh, *Signal expressions in Raman spectroscopy.* In Laserna J.J (Editor) *Modern Techniques in Raman spectroscopy,* John Wiley & Sons, Chichester, UK, 1996.

12. J. Behringer, *Observed Resonance Raman Spectra.* In Szymanski H.A (Editor), *Raman Spectroscopy : Theory and Practise.* Volume 1, Plenum Press, New York, (1967)

13. M. Fleischmann, P.J. Hendra, A.J. McQuillan, Chemical Physics Letters, (1974), Volume 26, pp 163-166.

14. D.L. JeanMarie, R.P. Van Duyne, Journal of Electroanalytical Chemistry, 1977, Volume 84, p1.

15. M.G. Albrecht, J.A. Creighton, Journal of American Chemical Society, 1977, Volume 99, p 5215.

16. R.K. Chang, B.L. Laube, CRC Critical Review of Solid State Matter Science, 1984, Volume 12, pp 1-73.

17. E. Koglin, J.M. Sequaris, Topics in Current Chemistry, 1986, Volume 134, pp 1-57.

18. E. Roth, G.A. Hope, Applied Spectroscopy, 1993, Volume 47, p 1794.

19. T.J. Wood, M.V. Klein, Journal of Vacuum Science and Technology, 1979, Volume 16, p 459.

20. C. Chen, E. Burstein, Solid State Communication, 1979, Volume 32, p 63.

21. P.F Liao, Chemical Physics Letters 1981,Volume 82, p 355.

22. M. Meier, Journal of Physical Chemistry, 1985, Volume 89, pp 1843-1846.

23. J. Neddersen, Applied Spectroscopy, 1993, Volume 47, p 1959-1964.

24. A. Girlando, M. Philpott, Journal of Chemical Physics, 1980, Volume 72, p 5187.

25. C. Chen, E. Burstein, Surface Science, 1980, Volume 101, p 363.

26. J.A. Creighton, Journal of the Chemical Society, Faraday Transactions, 1979, Volume II75, p 790.

27. P.C. Lee, D. Meisel, Journal of Chemical Physics, 1988, Volume 86, p 3391.

28. K. Kneipp, H. Kneipp, Applied Spectroscopy, 1998, Volume 52, p 175.

29. C. McLaughlin, Ph.D thesis (2001), Strathclyde University. *Development and Evaluation of Surface-enhanced Resonance Raman Scattering (SERRS) Spectroscopy for Quantitative Analysis.*

30. W. Suetaka, *Surface Infrared and Raman Spectroscopy; Methods and Applications*, Plenum Press, New York, USA, 1995.

31. J.J Gerstan, A. Nitzan, Surface Science, 1985, Volume 158, pp 165-182.

32. R.K. Chang, T.E. Furtak (Editors), *Surface Enhanced Raman Scattering,* Plenum Press, New York, USA, 1982.

33. T.E. Furtak, J. Reyes, Surface Science, 1980, Volume 93, pp 351-382.

34. J.J. Gerstan, A. Nitzan, Journal of Chemical Physics, 1980, Volume 73, pp 3023-3037.

35. M. Kerker, H. Chew, Applied Optics, 1980, Volume 19, pp 4159-4173.

36. A. Otto, J. Billman, I. Pockrand, Physical Review Letters, 1980, Volume 45, pp 40-46.

37. H. Ueba, Surface Science, 1983, Volume 131, pp 347-366.

38. A. Otto, *Light Scattering in Solids*, Volume 54, Cardona M., Guntherodt G., (Editors), Springer-Verlag, New York, USA, 1984.

Chapter 3

Review of Raman Instrumentation

3.1 Introduction

The first recognised observation of the Raman effect was reported in 1928[1]. Sunlight, collected using a telescope, was focussed through an optically transparent liquid. It was observed that when a pair of complementary filters were placed prior to the sample, the track of the light was extinguished. However, when the second filter was placed after the liquid, the track was restored, indicating that the sample had modified the light.

A basic block representation of a Raman spectrograph is shown in figure 3.1.

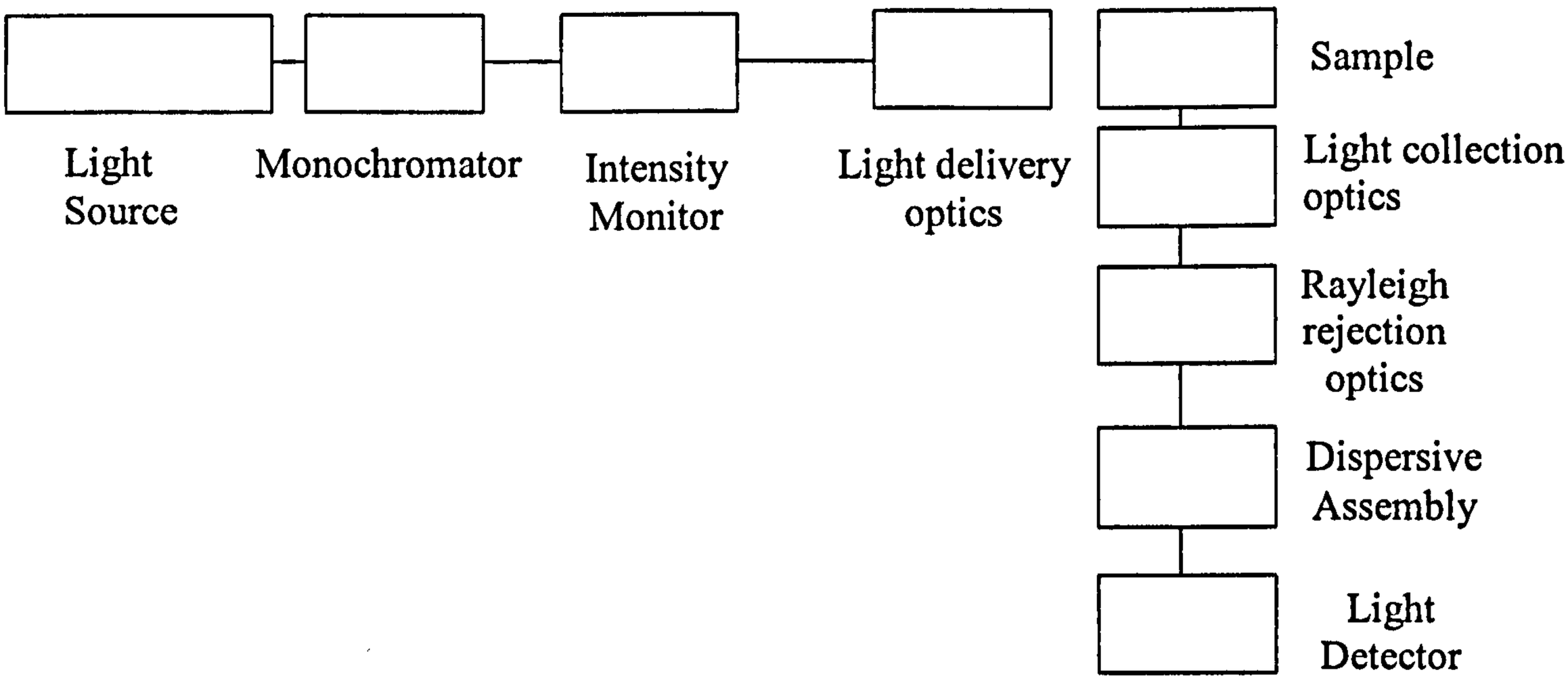

Figure 3.1 Raman spectrograph functional components

Early Raman instruments employed elemental gas-discharge excitation sources[2-4]. These were made obsolete in 1962 with the advent of the pulsed[5] and continuous-wave[6] laser. These enabled higher excitation powers to be delivered to samples down to the diffraction limit (≈1μm diameter). These large sources were often unstable, requiring an intensity monitor to normalise the recorded spectra. The instrumentation usually required water-cooling and was expensive in terms of electrical consumption and maintenance[7].

Scattered light was typically collected at 90° to the excitation direction. This is not directly suited to compact remote forensic sampling which ideally would originate and collect Raman scattered light from the same point so that a single operator could

perform the measurement. The rejection of Rayleigh scattered light in early Raman instruments was achieved through many methods[8-12]. The most common was to use a combination of diffraction gratings to disperse the scattered light and physically mask the Rayleigh scattered flux. This necessitated a large number of optical components, reduced the instrument transmissivity and increased the sampling time. Stray light, generated by each component was also a significant problem. The use of large numbers of optical components also introduced eccentric thermal and mechanical stability issues and reduced the repeatability of Raman spectroscopy.

The earliest Raman spectrograph used a photographic plate as a multiplex detector and a densitometer to record spectral intensities[13]. The early electronic detectors employed photomultiplier tubes, which were expensive, fragile and required Peltier cooling to maintain a constant low-noise performance. The use of a single element detector implied that spectra were recorded by mechanically scanning the Raman spectrum.

An example of a Raman spectrograph is shown in figure 3.2 and illustrates the complexity of this instrumentation.

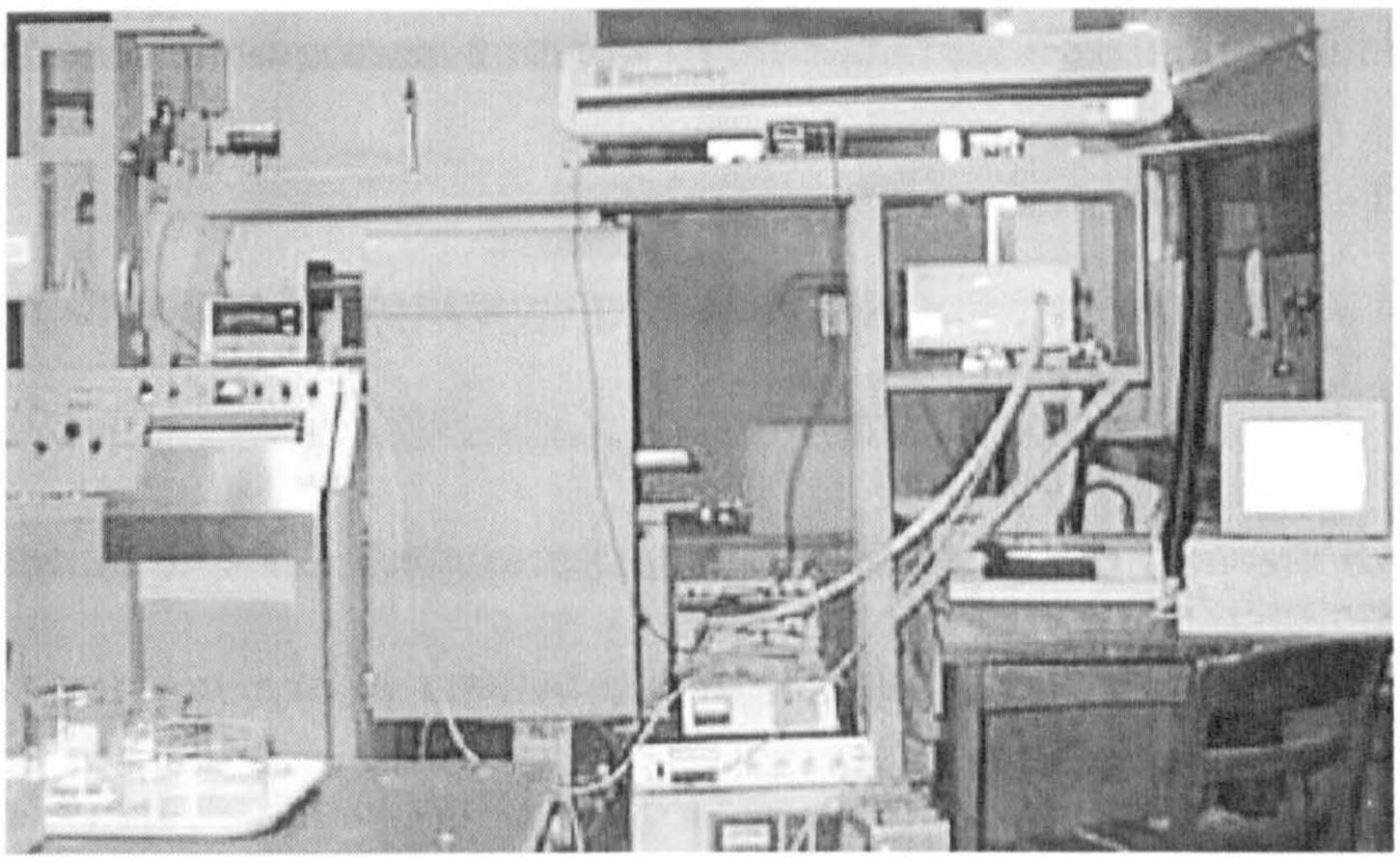

Figure 3.2 Cary Model-81 Raman Spectrograph

The early Raman instruments were large, expensive, unstable, and impractical for routine rapid forensic investigations. In conclusion, the use of Raman spectroscopy in forensic applications is a novel undertaking, challenged by many commercial, technical and physical problems associated with instrumentation, samples, sampling and the presumed limited skills of the intended user. At the time this thesis was written, only one commercial manufacturer claimed to provide a portable Raman instrument, illustrating the non-trivial nature of this work. The performance of the OceanOptics S2000 Raman spectrograph is reviewed, with particular emphasis on its short comings! In addition, the Renishaw System 1000 Raman microprobe is reviewed, since it features strongly in the feasibility studies described in this thesis. Although not described, a portable Raman analyser was developed for Renishaw Spectroscopy Products Division and some commercial advertising is shown in appendix A. The aim of this chapter is to

review the technical challenges presented by typical forensically-interesting materials and applications and to present a review of relevant research and instrumentation.

3.2 Forensic Samples

In-situ sampling presents the greatest technical challenge to forensic Raman sampling. Ideally the sample would be studied at long standoff from the instrument; enabling the operator to remain safe whilst investigating dangerous samples. Samples would be analysed without interference from ambient lighting or sample fluorescence. Sampling would be achieved in a class 1 laser environment; enabling safe operation for the user. Samples would be analysed in short integration times and identified automatically. In this section, these requirements are investigated, with an emphasis on reviewing the relevant published research and the instrumentation necessary to perform them.

3.2.1 Fluorescence

Real-world forensic samples, such as retrieved drugs caches or composite military-grade explosives, are highly inhomogeneous, comprising the Raman-active material embedded or mixed with typically fluorescent excipient or binder materials. This presents the single most challenging technical problem in developing an in-situ Raman analyser. The uncertainty associated with the measurement of intense sample fluorescence may prevent the identification of weak Raman spectral peaks. Sample

fluorescence is a problem estimated to be observed in approximately 80% of all possible Raman-active materials.[14]

There has been a variety of methods practiced in reducing fluorescence from bulk samples. These include;

- Photobleaching[15]
- Anti-stokes Raman spectroscopy[16]
- Addition of fluorescence quenching agents[17]
- Raman difference spectroscopy[18]
- Time or phase resolved methods[19]
- Non-linear techniques[20]
- SERS / SERRS[21]
- Confocal Raman microscopy[22]

Most of these techniques are difficult to implement practically, necessitating complex and delicate optical arrangements whilst others are incompatible with legal systems that prevent contamination of crime scene samples.

Laser excitation wavelengths from 50nm to 2000nm have been applied to Raman spectroscopy and the use of non-visible excitation has been demonstrated in overcoming fluorescence issues. The application of a particular laser wavelength is dependent upon the λ^{-4} Raman scattering dependence and the detector sensitivity. Most, if not all,

current scientific Raman instrumentation employs silicon-based multiplexed detection. A range of common systems is illustrated in figure 3.3.

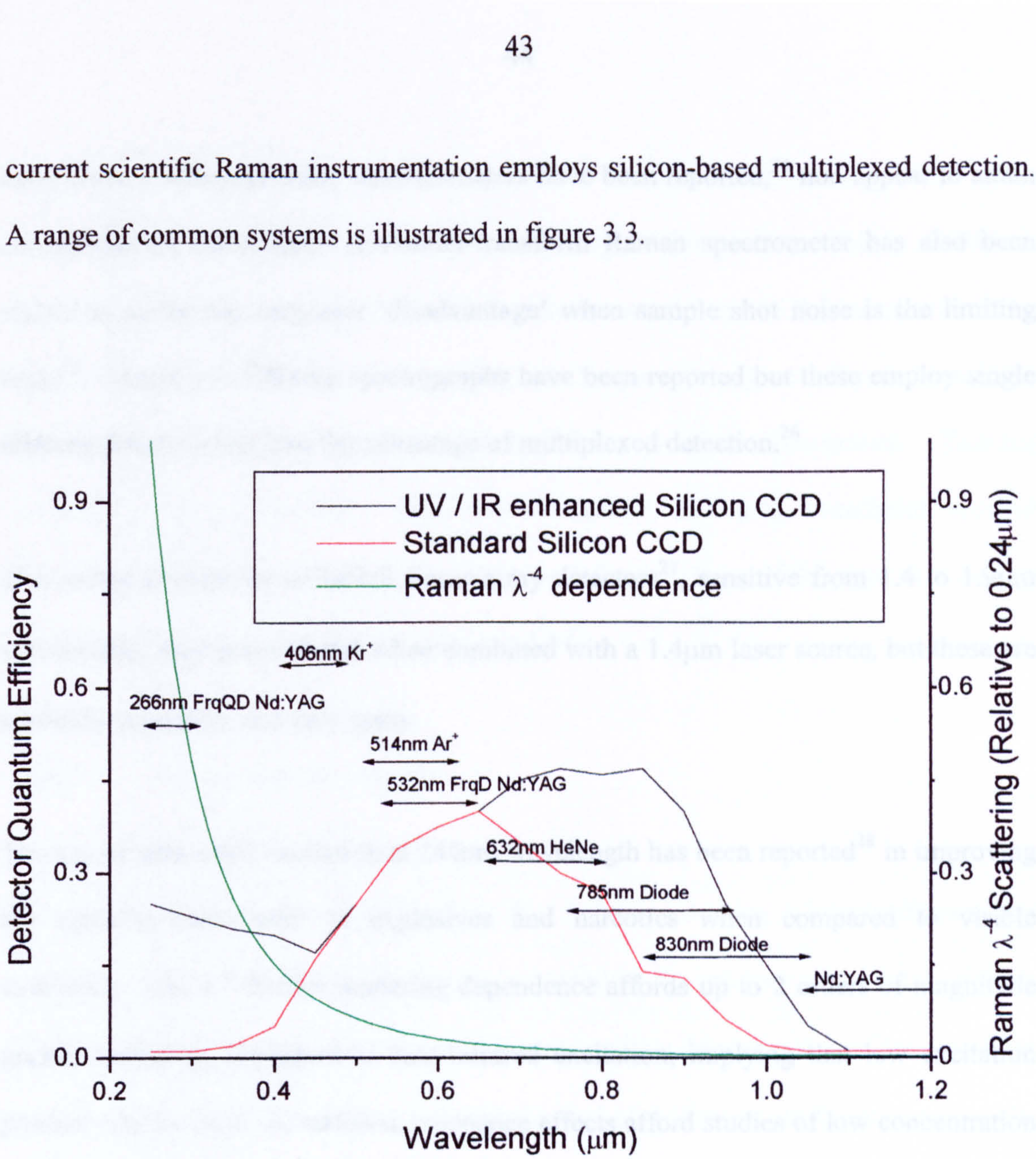

Figure 3.3 Typical silicon-based detection Raman systems

Fourier-transform Raman spectroscopy has demonstrated the advantage of near-infrared excitation at 1064nm over visible excitation[23] by exciting the sample beneath the lowest electronic transition and reducing the fluorescence cross section. The λ^{-4} Raman scattering dependence, however, implies that large excitation powers (≈1W) are required to achieve adequate signal-to-noise ratios. This has led to accidents involving explosives[14]. Fourier-transform Raman spectrometers usually have moving optical

components. Although static interferometers have been reported,[24] non appear to attain an appropriate resolution. A Fourier-transform Raman spectrometer has also been shown to suffer the Jacquinot 'disadvantage' when sample shot noise is the limiting noise[25]. Dispersive 1064nm spectrographs have been reported but these employ single element detectors and lose the advantage of multiplexed detection.[26]

The recent availability of InGaS linear array detectors[27], sensitive from 1.4 to 1.9μm wavelengths may prove useful when combined with a 1.4μm laser source, but these are currently expensive and very noisy.

The use of ultraviolet excitation at 244nm wavelength has been reported[28] in improving the signal-to-noise ratio of explosives and narcotics when compared to visible excitation. The λ^{-4} Raman scattering dependence affords up to 2 orders of magnitude greater scattering compared to near-infrared excitation, implying that low excitation powers may be used. In addition, resonance effects afford studies of low concentration samples[29]. In many samples, the use of 244nm excitation largely eliminates fluorescence from the Raman spectrum. The fluorescence is still present, but is shifted to longer wavelengths than the Raman scattered spectrum. The recent availability of solid state, diode pumped, UV lasers may eventually make in-situ UV Raman studies feasible.[30]

At present, the most commercially-viable partial solution to fluorescence is to use a high-power near-infrared excitation source in conjunction with a silicon-based CCD detector. Exposing the sample to the laser prior to acquiring a spectrum often enables

an extent of photobleaching that may improve the detection performance. Diode lasers have been evaluated for Raman use[31-32], affording excitation from 630nm to 850nm wavelength. Using a deep-depletion CCD detector would enable Raman spectra to be recorded up to 2500cm^{-1}, encompassing the fingerprint region of most materials currently associated with clandestine drugs and explosives manufacture. Thermal instability, current instability, sensitivity to optical feedback, broadband spectral emissions and an anamorphic beam output are all disadvantages of this type of laser, but many commercial sources are becoming available.

3.2.2 Signal-to-Noise Ratio

In figure 3.4, an incident excitation flux, Φ_{ex}, is focussed using a lens to illuminate a sample scattering volume that can be approximated by the product of the depth of field, l, and the area of the focussed laser, πr^2. A more precise determination of the scattering volume is given elsewhere[33]. A correctly designed Raman analyser matches the collection volume of the instrument to the illuminated scattering volume.

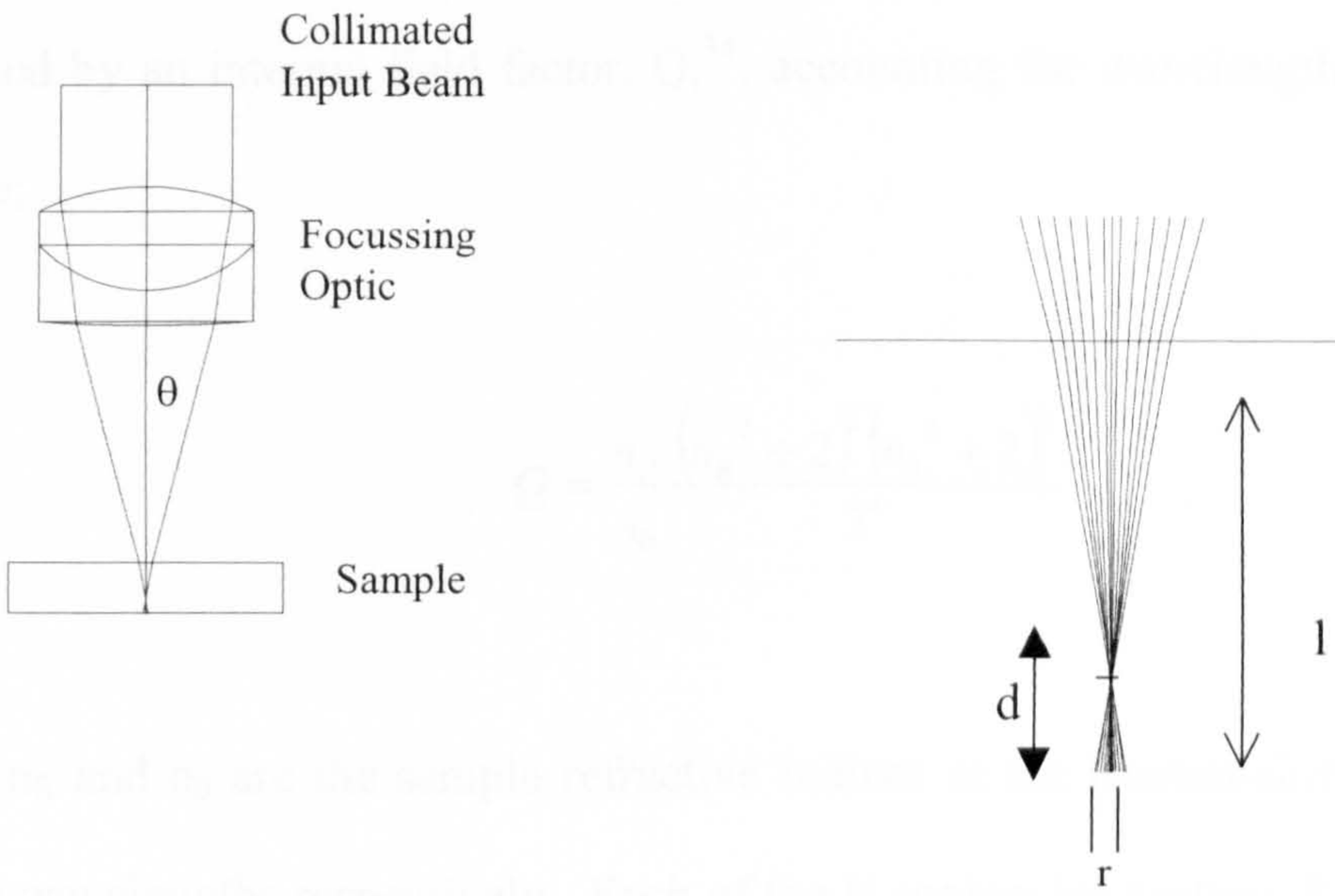

Figure 3.4 Raman scattering

Rays are incident onto the sample surface within a cone of semi-angle, θ, defined by the numerical aperture of the focussing lens. Each ray strikes the sample-air interface, undergoing refraction and reflection. The rays penetrate the sample with an intensity, I, which decays according to equation 3.1.

$$I = I_0 e^{-\alpha_{ex} l} \qquad \textbf{3.1}$$

where α_{ex} is the linear absorptivity, including the effects of scattering induced by sample inhomogeneities, at the excitation wavelength. The distance l is the effective path length through the sample. Raman scattered flux, Φ_R, generated in the sample, is similarly attenuated on its path back to the collection optic, characterised by a linear absorptivity, α_R. In a sample with a highly wavelength-dependent refractive index, the

rays are refracted from the excitation path. The collection numerical aperture is modified by an internal field factor, Q,[34], accounting for wavelength dispersion in the sample;

$$Q = \frac{n_R}{n_0}\frac{\left(n_R^{\,2}+2\right)^2\left(n_0^{\,2}+2\right)^2}{3^4} \qquad \textbf{3.2}$$

where n_R and n_0 are the sample refractive indices at the Raman-shifted and Rayleigh-shifted wavelengths respectively. Each of the N molecules scatters Raman-shifted light into a 4π sr solid angle, with a scattering cross section, $\frac{\partial\sigma}{\partial\Omega}$, as derived in Chapter 2. It has been shown[34] that the total collected radiant flux, Φ_R, is given by;

$$L_R = \left(\frac{\Phi_{ex}}{\pi r^2}\right).d.\left(\frac{\partial\sigma}{\partial\Omega}\right).(\nu_0-\nu_R)^4.\rho_N.Q.\frac{1}{\alpha_0+\alpha_R}\left(1-\exp^{-(\alpha_0+\alpha_R)d}\right) \qquad \textbf{3.3}$$

Where ρ_N, is the molecular number density, d is the depth of field of the system and ν_0 and ν_R are the excitation and Raman-shifted wavelengths in wavenumbers respectively. Ignoring issues of polarisation and the presumed isotropic scattering characteristics of a Raman-active sample; the integrated intensity of a spectral function, $\Phi_R(\lambda)$, collected from an analyte of radiance, $L_R(\lambda)$, over an illuminated area, A and a small solid angle, Ω is given by;

$$\Phi_R(\lambda) = \iint L_R(\lambda) d\Omega dA \qquad \textbf{3.4}$$

The number of photoelectrons recorded, η_{PE}, by a discrete element detector (or a single pixel in an array detector) of bandwidth λ_2-λ_1 is given by;

$$\eta_{PE}(\lambda) = t_{\text{int}} \int_{\lambda_1}^{\lambda_2} \left[g(\lambda) \otimes \left(\Phi_R(\lambda) \tau_{sys}(\lambda) Q_{CCD}(\lambda) \right) \right] d\lambda \qquad \textbf{3.5}$$

where t_{int} is the experiment integration time, $\tau_{sys}(\lambda)$ is the wavelength-dependent system transmissivity, $Q_{CCD}(\lambda)$ is the wavelength-dependent detector quantum efficiency, $\Phi_R(\lambda)$ is the wavelength spectral profile of the spectral feature and $g(\lambda)$ is the spectrograph point-spread function.

The definition of signal-to-noise ratio is critical and follows the methodology of Stevenson and Vo-Dinh[35]. A single spectral feature may be represented by figure 3.5. A Raman band is centred at x_0 cm^{-1}, with a width, w, on a linear background I_B. The intensity of the Raman band, I_S, corresponds to the background-subtracted height of the peak at its centre.

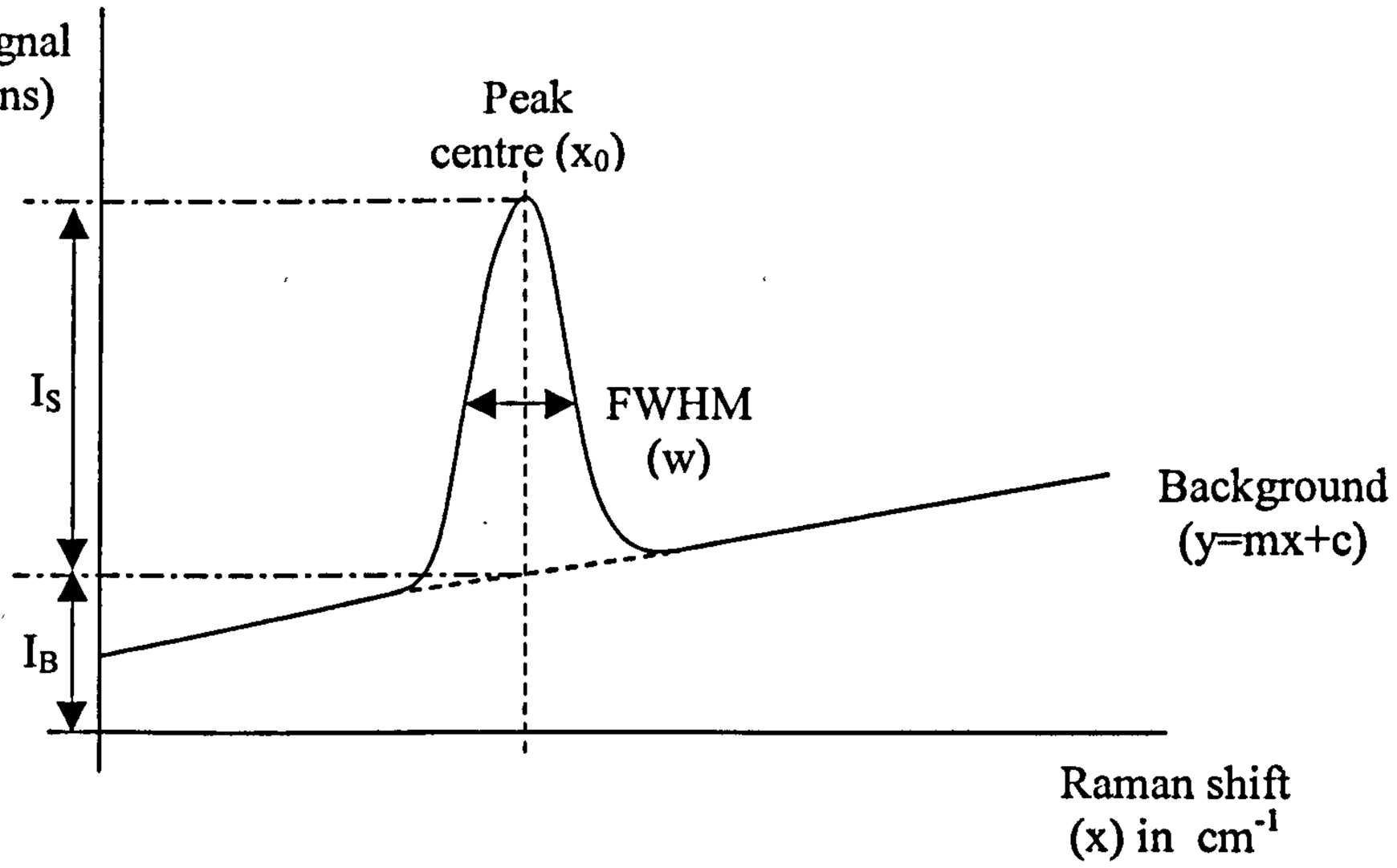

Figure 3.5 Modelled spectral peak

In a system where the "shot-noise" or "photon-noise" associated with the background is the determining noise contribution, the signal-to-noise ratio of the peak is given by[35];

$$SNR = \frac{I_S}{\sqrt{I_S + I_N{}^2 + 2(I_B)}} \qquad 3.5$$

Where I_S is the background-subtracted peak intensity, I_B is the background baseline height and I_N is the detector read-out noise. (All heights are in photon counts.)

3.2.3 Trace Detection Studies

In trace-detection forensic applications, the concentration of Raman-active material present within the instrument sampling volume may be too low to enable adequate spectra to be recorded using safe laser excitation powers and short integration times.

The use of Raman spectroscopy in vapour sampling applications is typically limited to Raman LIDAR[36] instruments where the volume of sampling material is made extremely large to compensate for a low sample concentration. This is typically used in environmental monitoring, but could conceivably be applied to remotely identifying forensically-relevant factory emissions. The use of a long optical path with high laser power is not suited to vapour detection applications in public areas for safety reasons.

An alternative method for performing Raman trace detection is to use SERS or SERRS to substantially increase the Raman scattering cross section of the target material. This is especially applicable to situations involving limited volumes of sample. Examples of SERS analysers for environmental contamination monitoring, detecting metabolites of narcotics ingestion, and explosives vapours have been reported[37-39]. This forms the focus of Chapter 4. Under well-defined experimental conditions, SERS or SERRS is difficult to perform and has specific experimental characteristics. These are;

- For solution studies, the sample is mixed with a bulk medium with a high extinction coefficient. The sampling arrangement must be carefully designed to maximise the scattered light collected without significant sample self-

absorption. Sample absorption can give rise to heat generation and thermal lensing.

- Fluorescence quenching may be observed at low sample concentrations. Spectral peaks are typically present, superimposed on a broadband luminescent spectral background. This precludes the use of a multiplexed interferometer-based instrumentation due to the Jacquinot disadvantage.

- The observed enhancement of Raman scattering is related to the sample-induced colloid aggregation, which alters the colloid extinction. In addition, the colloid aggregation is highly dependent on sample temperature, pH and other sampling conditions.

- The excitation wavelength must coincide simultaneously with the colloid plasma resonance frequency. For gold and silver colloids, this precludes the use of near-infrared excitation, particularly the 1064nm wavelength commonly found in FT-Raman instruments.

- The bandwidths of spectral features are considerably broadened with respect to conventional Raman spectra. This has been ascribed to the presence of a population of active sites, with different binding attributes and co-ordination geometry. The consequence of this is that the resolution requirement for a SERS/SERRS spectrograph is not so high.

The function of SERS and SERRS analysis can be achieved using a specialised instrument designed for this type of Raman spectroscopy.

3.3 Sampling Issues

Delivering the excitation onto the sample and collecting the scattered light safely, whilst maintaining sampling flexibility, is technically difficult. There are many examples of Raman spectrographs coupled to optical-microscopes and these are not suited to in-situ analysis of bulk samples. The use of high numerical aperture telescopes[36], achromatic lenses[23] and microscope objectives[22] have been reported in the collection of Raman scattered light over 9 decades of sampling distances. In general, the excitation powers required to overcome the intrinsically small Raman scattering cross section of most materials are not safe and therefore long standoff detection shall not be considered as a means for sampling in this thesis. The feasibility of a standoff SERRS analyser is described in Chapter 5.

The use of optical fibres to perform remote Raman measurements in hostile environments has been reported from many sources[40-41] and is ideally suited to forensic screening applications. Real-world samples are often located in hazardous and difficult to access environments.

3.3.1 Remote Raman Optical Probes

The distinction between optical probe (optrode) designs arises from whether or not the distal end of the optical fibre (end closest to sample) directly illuminates the sample, or indirectly using additional optical components.

Direct-coupled probe designs are diverse and differ according to the number of optical fibres used to collect the Raman scattered light. An example of a direct-coupled probe is shown in figure 3.6[42]. Illumination of the sample is achieved using the central fibre. Raman scattered light is collected in 180° backscattering geometry using the angled ring of optical fibres.

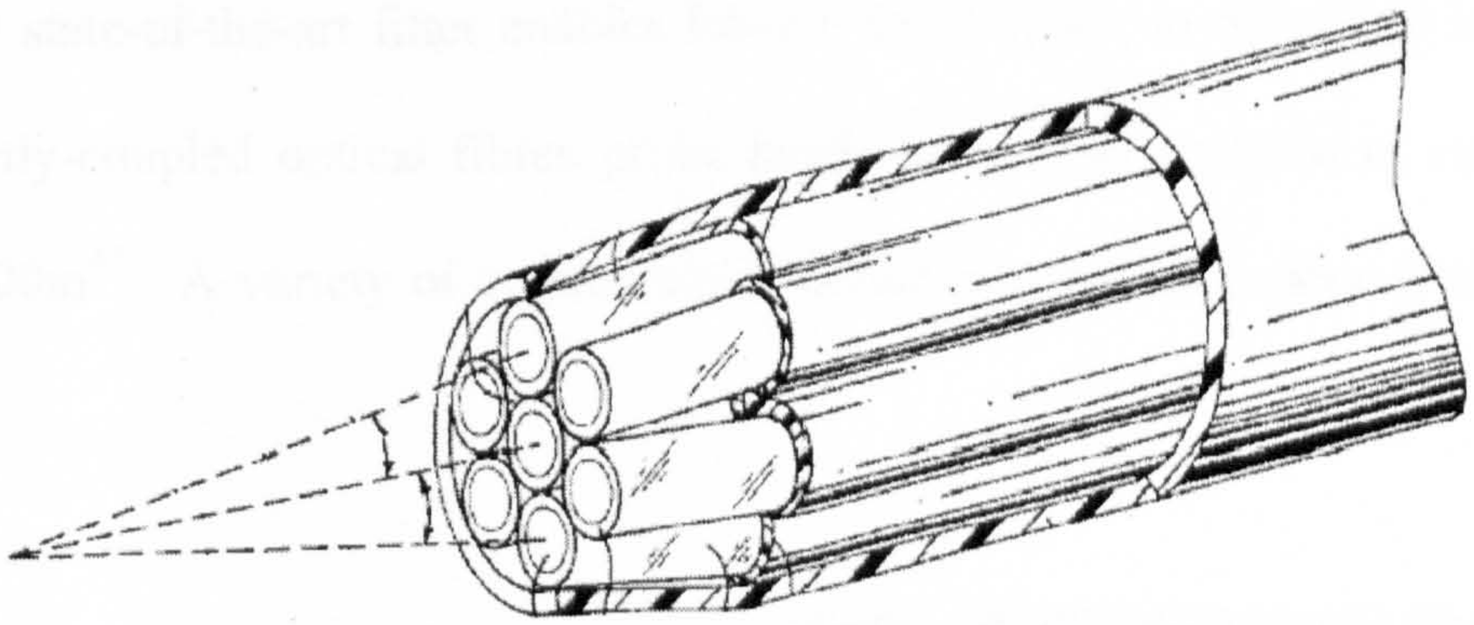

Figure 3.6 Visionex direct-coupled optical-fibre probe[41]

Direct-coupled probes may be dipped into liquids but are easily contaminated unless sampling is performed through an impermeable membrane.[43]

The use of ancillary optics to optimise the coupling of the laser to the sample has resulted in many indirect-coupled probe designs[44-46]. In general, the distal end of the laser delivery optical fibre is collimated and bandpass filtered to attenuate fibre-generated Raman and fluorescence. The filtered and collimated laser light is reflected off a notch or longpass filter into the rear aperture of a focussing objective lens. Short focal length lenses achieve a small depth of field, which makes sampling difficult. Collected scattered light returns along the optical path as a collimated beam. The intensity of Rayleigh scattered light is attenuated typically to 1 in 10^8 photons by a pair of notch filters. The Raman scattered light is focussed into a second optical fibre which is coupled to a spectrograph. In forensic applications, there are sufficient Raman bands

beyond the typical 200cm^{-1} notch filter cutoff to enable sample identification. The current state-of-the-art filter enables Raman shifts down to 50cm^{-1} to be investigated. Indirectly-coupled optical fibres probe heads have been reported in remote sampling over 200m[47]. A variety of commercially obtainable optical probes is shown in figure 3.7.

A

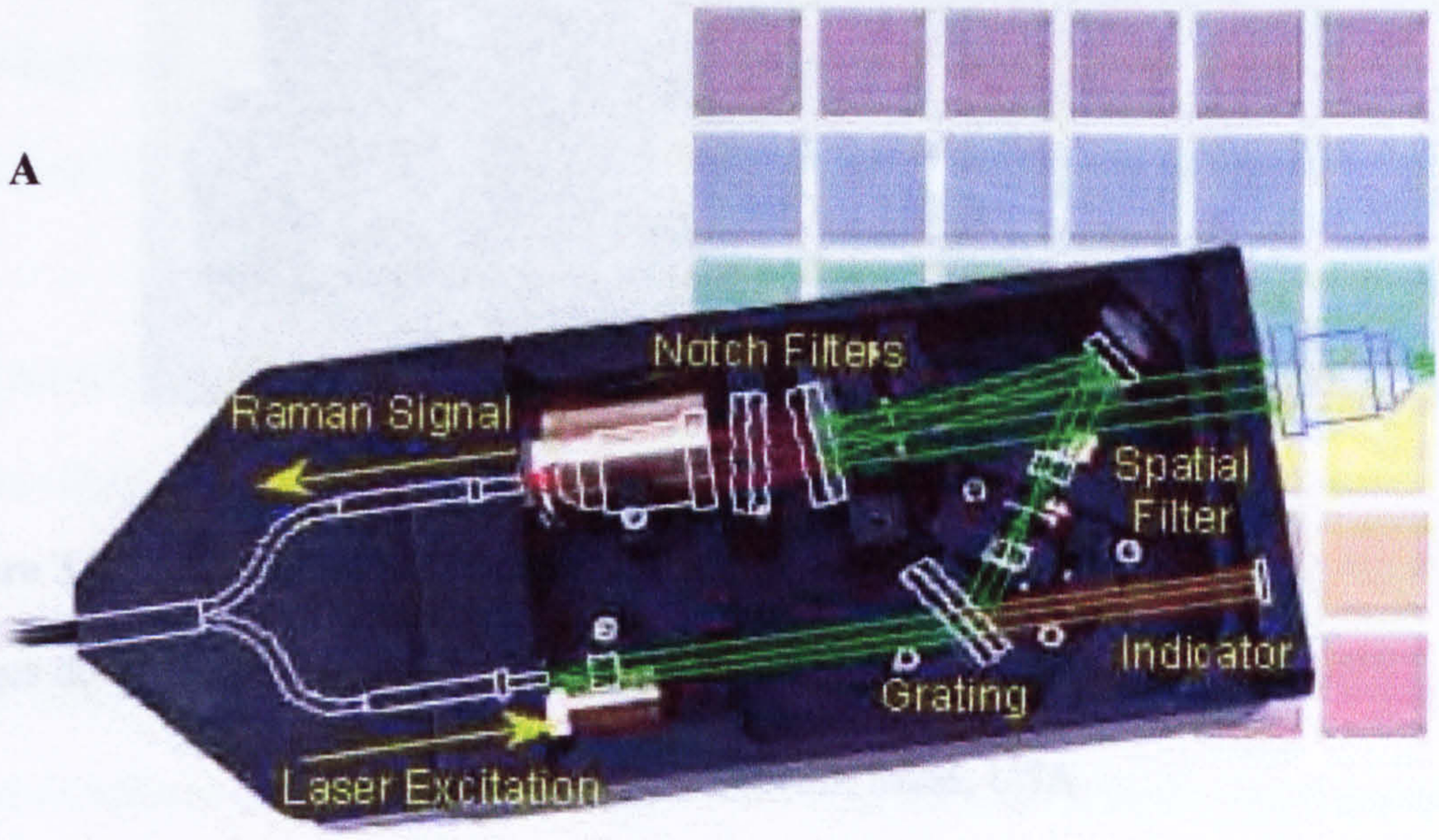

B

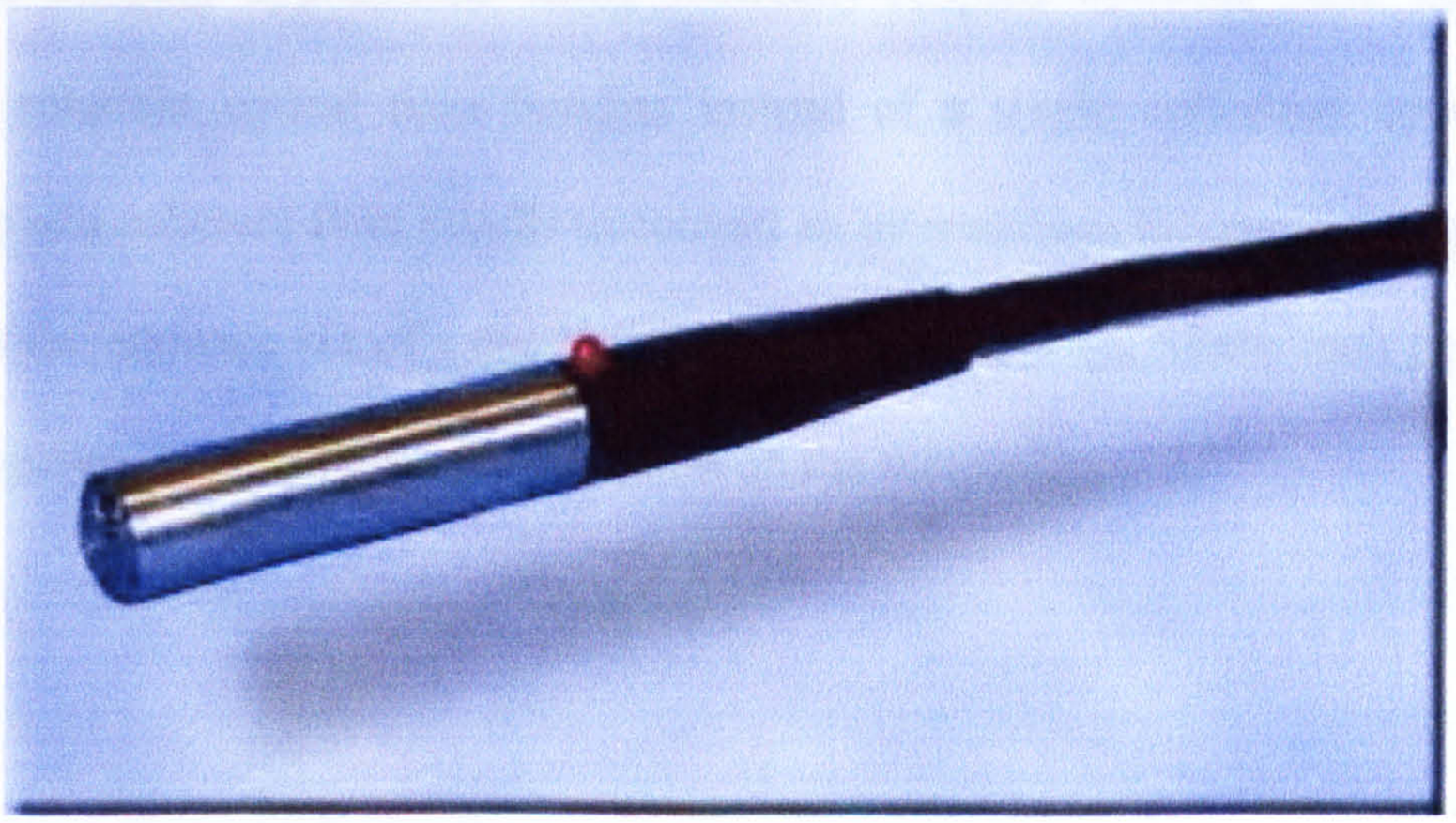

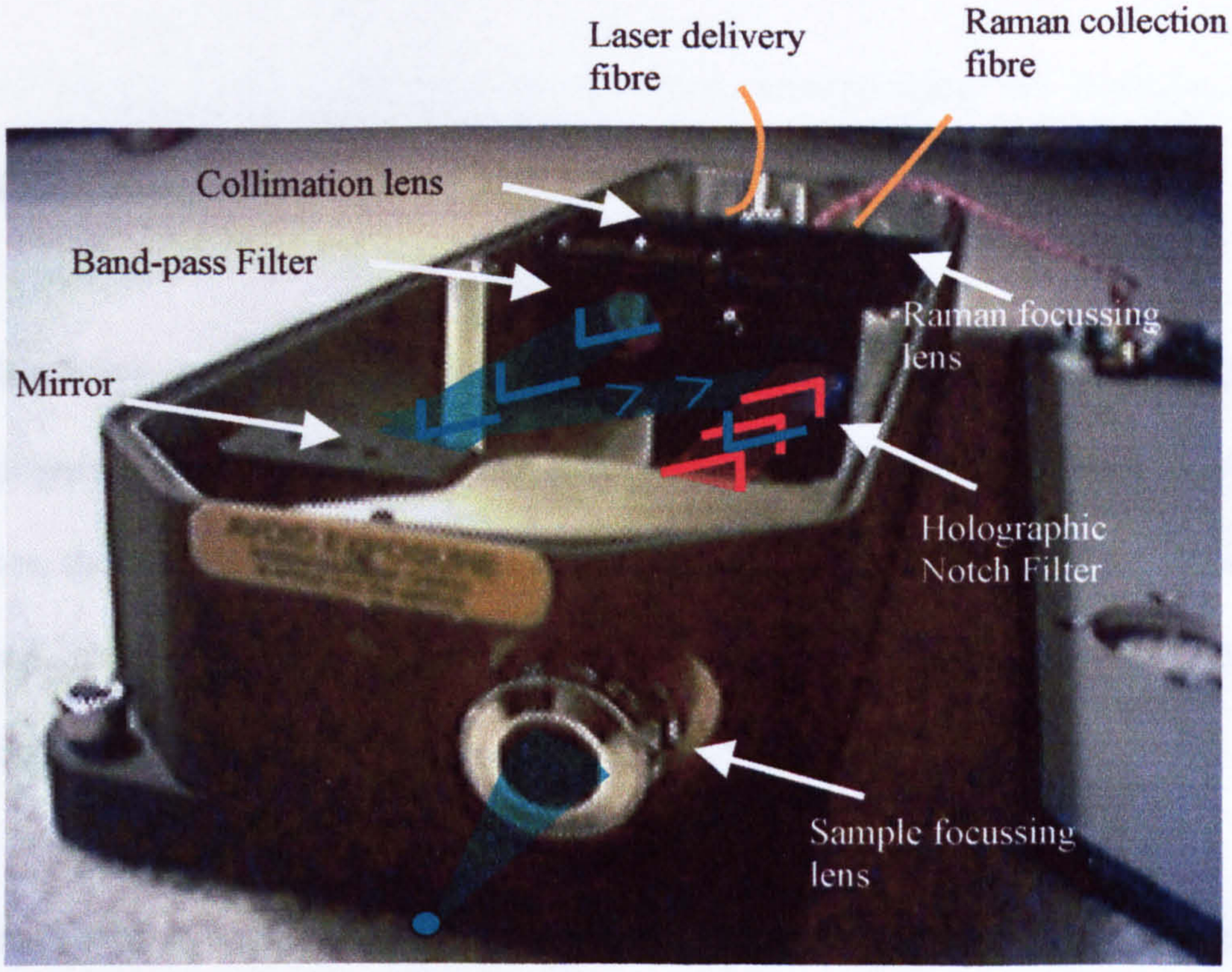

Figure 3.7 Commercially available indirect-coupled probe heads

Images downloaded from (A) Kaiser Optical, Mass, USA

(B) EIC Laboratories, Mass, USA

(C) Renishaw Spectroscopy, UK

Remote Raman imaging applications using indirectly-coupled optrodes have been reported using coherent optical fibre bundles instead of a single collection optical fibre[48]. The use of a coherent fibre bundle to convert an intermediate Raman image into a line, placed at the entrance slit of a spectrograph has been reported, where each point in the slit corresponds to a spatially-resolved point on the sample[49].

3.4 Spectrographs

An ideal dispersive spectrograph comprises: an entrance aperture, a collimating element, a dispersion element, a focussing element and a multi-element detector. In most instances, these components are discrete, although there are many examples where focussing and dispersion are achieved in a single component, and dispersion and detection are performed in a single detector.[50]

The performance of a Raman spectrograph is characterised by: etendue, resolving power, etendue-resolving power product, information bandwidth and stray light[51].

Early Raman spectrographs used large prisms in conjunction with long focal length lenses to achieve high resolution. Spectra were scanned over a single element detector, requiring extremely long integration times, and suffered from poor thermal and mechanical stability. The instrumentation was extremely large, expensive, heavy and delicate. The first Raman spectrum recorded using a ruled diffraction grating was reported in 1928[52]. Diffraction gratings provide the possibility of greater resolving power than early prisms. Ruled gratings suffer however from poor stray light characteristics[53]. "Grass" caused by surface dust contamination, ghosts, satellites and surface-plasmon scattering all contribute stray light and introduce spectral artefacts. Wood's anomalies produce spurious, polarisation dependent diffractive efficiencies that require effective calibration. Mechanical constraints limit the grating ruling densities to 1600 lines per mm. Concave diffraction gratings and abberation-corrected diffraction

gratings were reported with similar groove densities, incorporating the function of focussing and dispersion, affording improved instrument transmissivity.

A forensic Raman analyser requires a resolution of approximately $8cm^{-1}$ to achieve adequate spectral performance[54]. The spectral range must extend to cover as much of the fingerprint region from $200cm^{-1}$ to $3200cm^{-1}$ as possible. Early Raman instruments could only achieve this by employing either long focal length lenses in conjunction with low groove density gratings, or short focal length lenses used in conjunction with high groove density gratings. The first design typically produced a massive instrument profile, whilst the latter suffered from severe imaging aberrations and poor transmission.

The development of compact, portable Raman spectrographs has been aided by the recent development of high numerical aperture, wide field imaging camera lenses with high quality imaging characteristics. The use of high performance anti-reflection coatings in these lenses reduces the straylight generated at each optical interface and increases the instrument transmissivity.

The use of short focal length lenses in combination with a fixed position, high groove density grating has enabled spectral resolution and spectral range suitable for recording the bulk of the Raman fingerprint region to distinguish different materials. Recent designs enabling the extension of the spectral range, whilst maintaining a suitable resolution, have been proposed for two-dimensional imaging detectors and fixed optical

components[55-57]. An example of one of these, the sandwich-scope[56] is shown in figure 3.8.

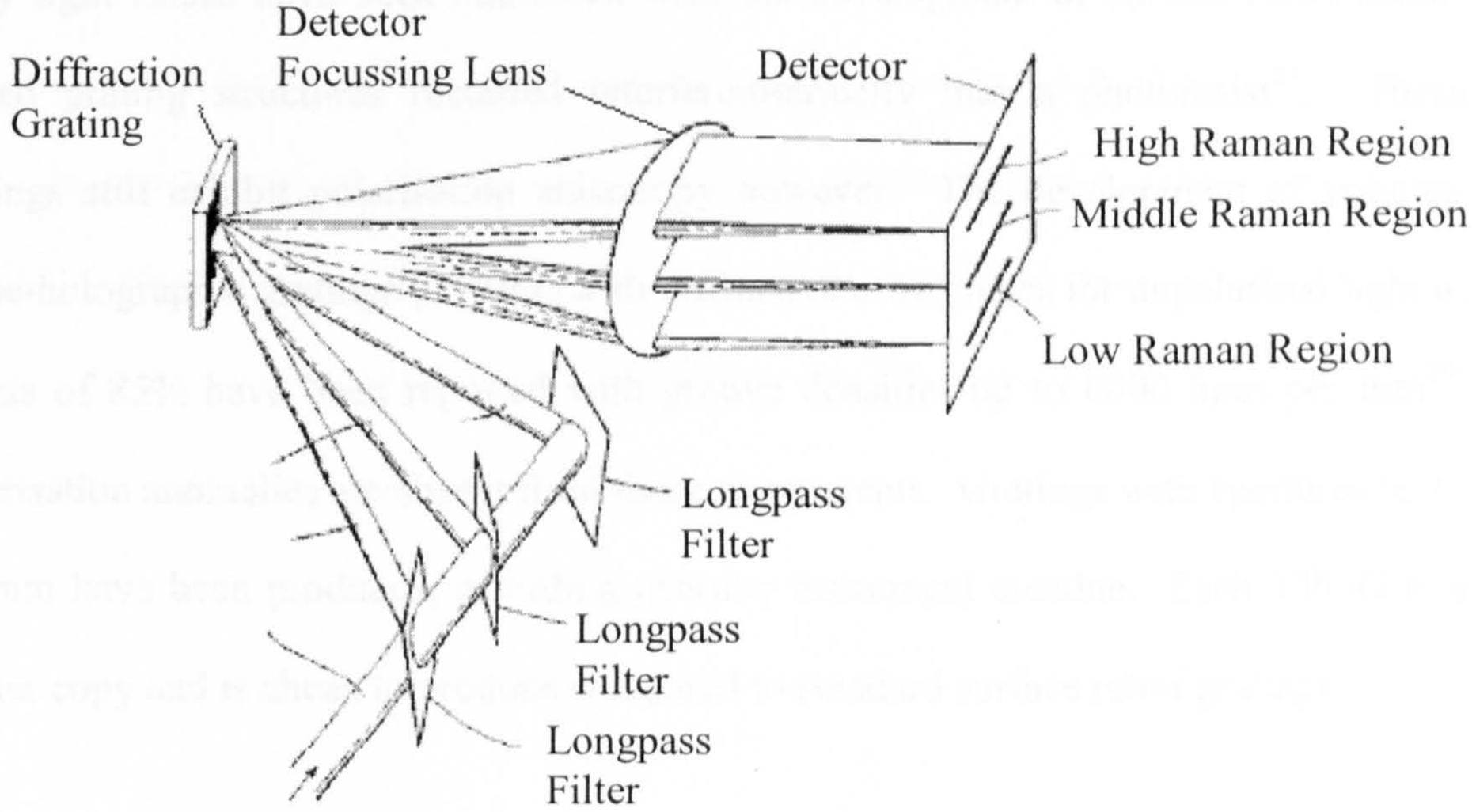

Figure 3.8 Sandwich-scope concept

The use of a 2-dimensional CCD array as a detector for Raman spectroscopy was first reported in 1986[58]. M-spatially resolved channels enabled the signal-to-noise ratio to be increased by $\sqrt{M}$ compared to single channel detection using the sample experimental parameters. In addition to this multiplex advantage, CCD detectors are intrinsically more tolerant to overexposure. The multiplex advantage is significant in enabling short spectral acquisition times. CCD detector performance is characterised by quantum efficiency, read noise, dark noise, charge-transfer efficiencies and pixel-to-pixel response non-uniformity. Most CCD detectors are now thermoelectrically-cooled to a

point where dark noise is insignificant, precluding the requirement for expensive and delicate nitrogen-cooling systems.

Stray light issues have been addressed with the development of surface-relief metal-coated grating structures recorded interferometrically into a photoresist[53]. These gratings still exhibit polarisation anisotropy however. The development of volume-phase-holographic gratings (VPHG) with diffractive efficiencies for unpolarised light in excess of 85% have been reported with groove densities up to 6000 lines per mm[59]. Polarisation anomalies are absent from these components. Gratings with apertures up to 400mm have been produced, affording massive instrument etendue. Each VPHG is a master copy and is cheap to produce compared to standard surface relief gratings.

Technological factors preventing the successful implementation of a novel forensic Raman in-situ analyser are weakening under current developments in thin film filter technologies, holographic optics, lasers and CCD detector technologies. The core elements identified in this chapter offer the potential to enable Raman spectroscopy to be used as a means of rapid, non-destructive testing.

3.5 Commercially Available Instrumentation

3.5.1 Renishaw System 1000 Raman Microscope

The Renishaw System 1000 Raman microscope is illustrated schematically in figure 3.9. A comprehensive design appraisal of the instrument and other variants are available elsewhere[60]. Briefly, the instrument comprises 7 sub-sections; a laser, delivery optics, a conventional optical microscope, Rayleigh rejection filters, a high resolution spectrograph and a CCD detector.

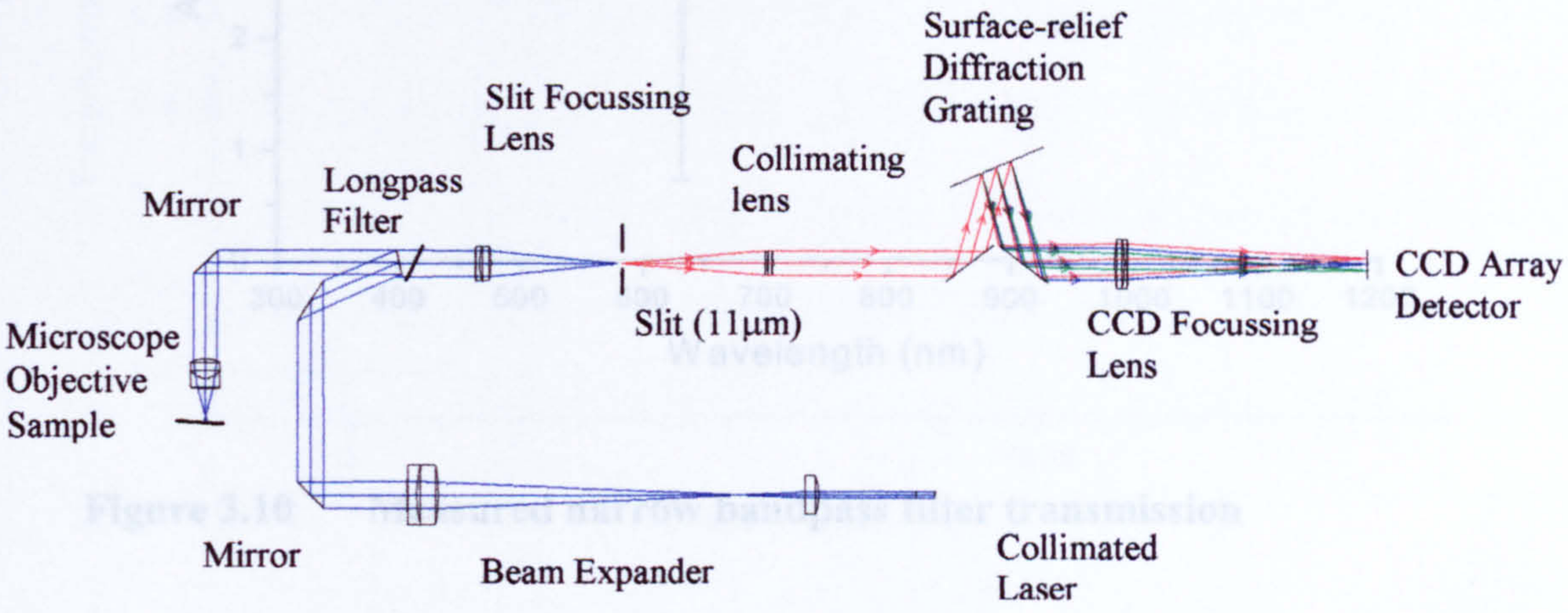

Figure 3.9 Ray-trace of Renishaw System 1000 Raman Microscope (not to scale)

A 25mW, Helium-Neon 632.8nm wavelength laser (Melles-Griot, 25LPH925) was used to produce a gaussian profiled collimated laser beam of 0.7mm diameter (points where the intensity is $1/e^2$ of the central maximum). The laser was passed through a narrow

bandpass filter at low incidence angle to attenuate non-lasing transitions from the laser cavity, whilst preventing reflections from returning to the laser. The measured transmission of the narrow-bandpass filter is shown in figure 3.10.

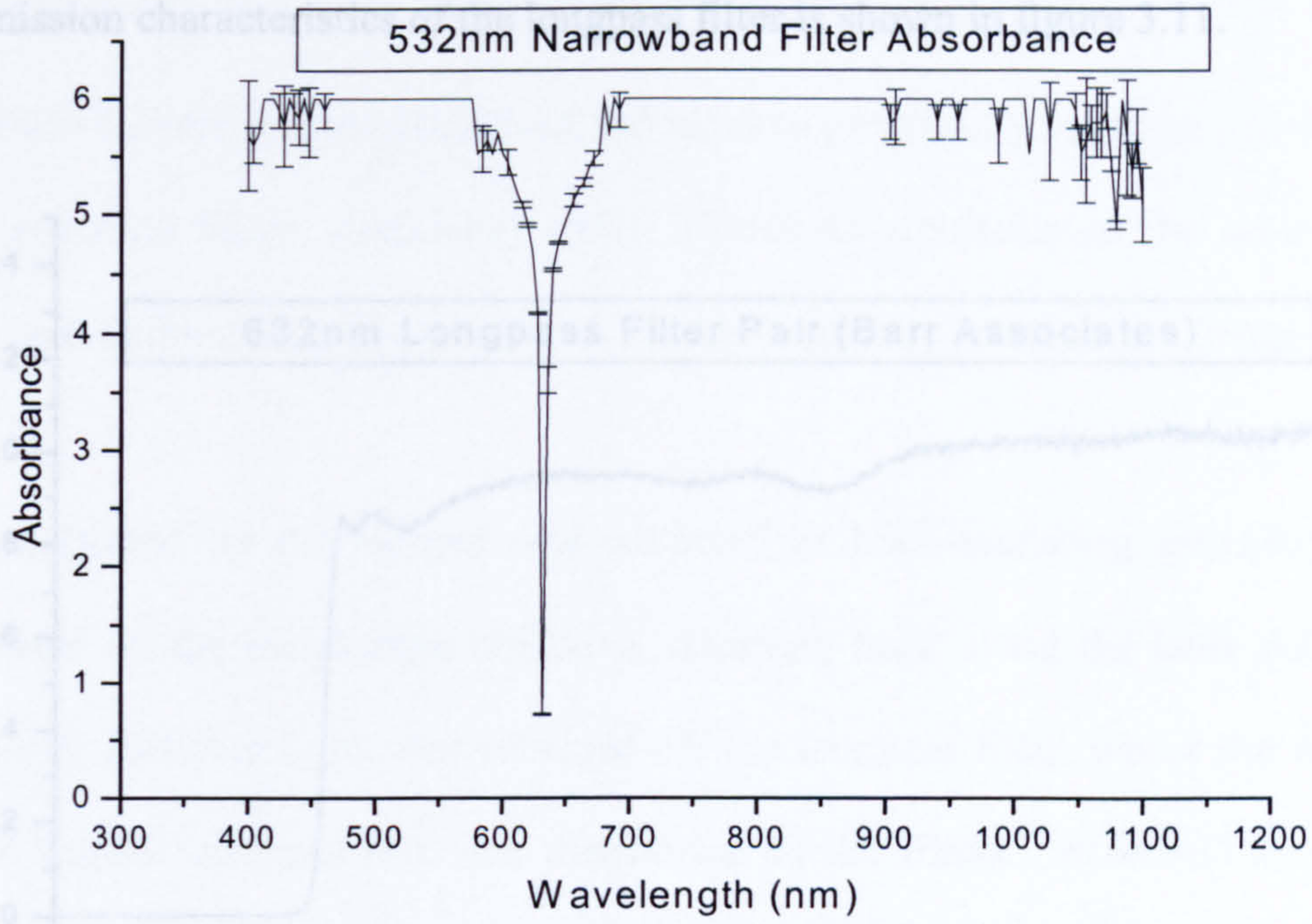

Figure 3.10 Measured narrow bandpass filter transmission

The filtered laser beam was reflected using a pair of mirrors into the rear aperture of a x20 microscope objective, which focussed the laser through a 10μm diameter pinhole. A second x4 microscope objective, mounted on a computer-controlled linear translation stage, was used to collimate the flux transmitted by the pinhole. This improves the laser cross-section uniformity, expands the laser diameter to approximately 6mm diameter and reduces the instrument stray light caused by non-paraxial rays.

The expanded laser was reflected using mirrors onto the surface of a longpass filter LPF1. This comprises multiple dielectric layers, coated onto an absorbing substrate. The filter affords high reflectivity at wavelengths near to the laser wavelength, whilst remaining highly transmissive for Stokes-shifted wavelengths. The measured transmission characteristics of the longpass filter is shown in figure 3.11.

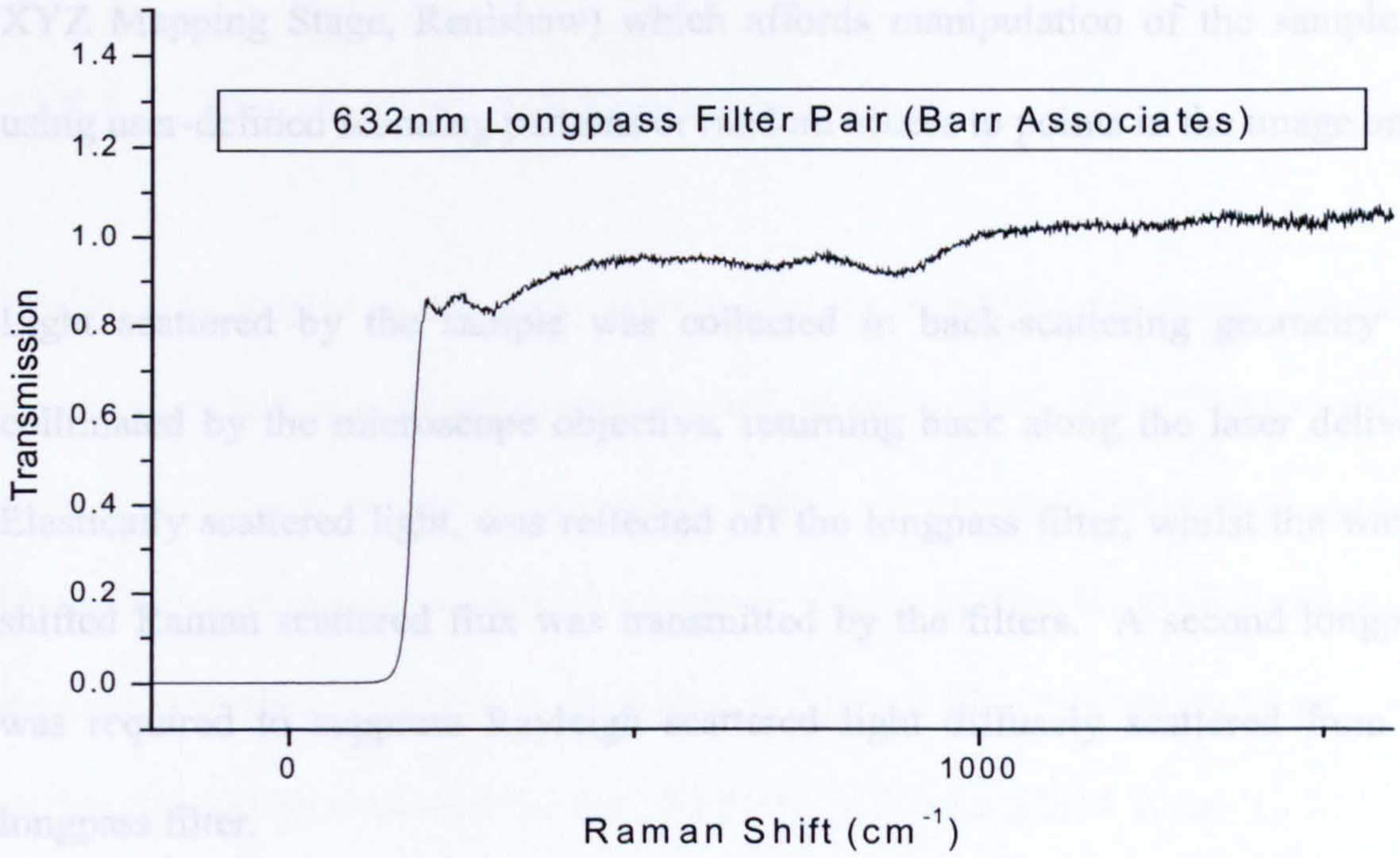

Figure 3.11 Measured transmission function for longpass filter

The laser was reflected into the modified microscope body. A mirror placed between the microscope tube lens and objective reflected the laser beam into the rear aperture of an infinity-corrected microscope objective (Olympus, MSPLAN Series). This enabled the laser to be focussed into a near diffraction-limited spot, affording high sample power density, and spatial resolution of the order of microns.

Samples were presented for analysis on a position-encoded XYZ mapping stage. This affords a manufacturer-specified spatial resolution of 1μm. Samples were observed using white light epi-illumination and observed using either a video camera or binocular attachment.

The video camera output is digitised and input to proprietary mapping software (WiRE XYZ Mapping Stage, Renishaw) which affords manipulation of the sample position using user-defined scanning patterns or random access to points in the image on screen.

Light scattered by the sample was collected in back-scattering geometry and was collimated by the microscope objective, returning back along the laser delivery path. Elastically scattered light, was reflected off the longpass filter, whilst the wavelength-shifted Raman scattered flux was transmitted by the filters. A second longpass filter was required to suppress Rayleigh scattered light diffusely scattered from the first longpass filter.

The Raman scattered flux was focussed using a 50mm focal length achromatic lens to an adjustable slit (Renishaw). The slit affords an element of spatial filtering in one dimension. The image of the slit at the sample defines the spatial resolution. The slit additionally affords axial sectioning, attenuating stray light.

Flux transmitted through the entrance slit aperture, was collimated using a 150mm focal length achromatic lens and reflected off a mirror-coated prism onto a surface-relief, metal diffraction grating (Optometrics,1800VIS). The diffraction grating, mounted on

an encoded-position rotation stage (Renishaw, UK), rotates to control the spectral region received by the detector. The dispersed Raman-scattered light is focussed, usinga 250mm focal length achromatic lens onto a thermoelectrically cooled, charge-coupled device (CCD) camera (Renishaw, UK). The CCD is read using a personal computer, which displays the integrated signal from each spatial element (pixel) and displays this as a spectrum.

3.5.2 OceanOptics R2000 Raman System

Ideally, this project would have concentrated on extending the in-situ applications of Raman spectroscopy to solving real-world forensic problems. Unfortunately, at the time this project began (September, 1998), there was only one manufacturer, OceanOptics, claiming to produce a portable Raman system for general-purpose, in-situ forensic investigation. This is illustrated in figure 3.12. An instrument was purchased so that it could be evaluated for use by PSDB. All information presented in this section was available in the public domain[61-64].

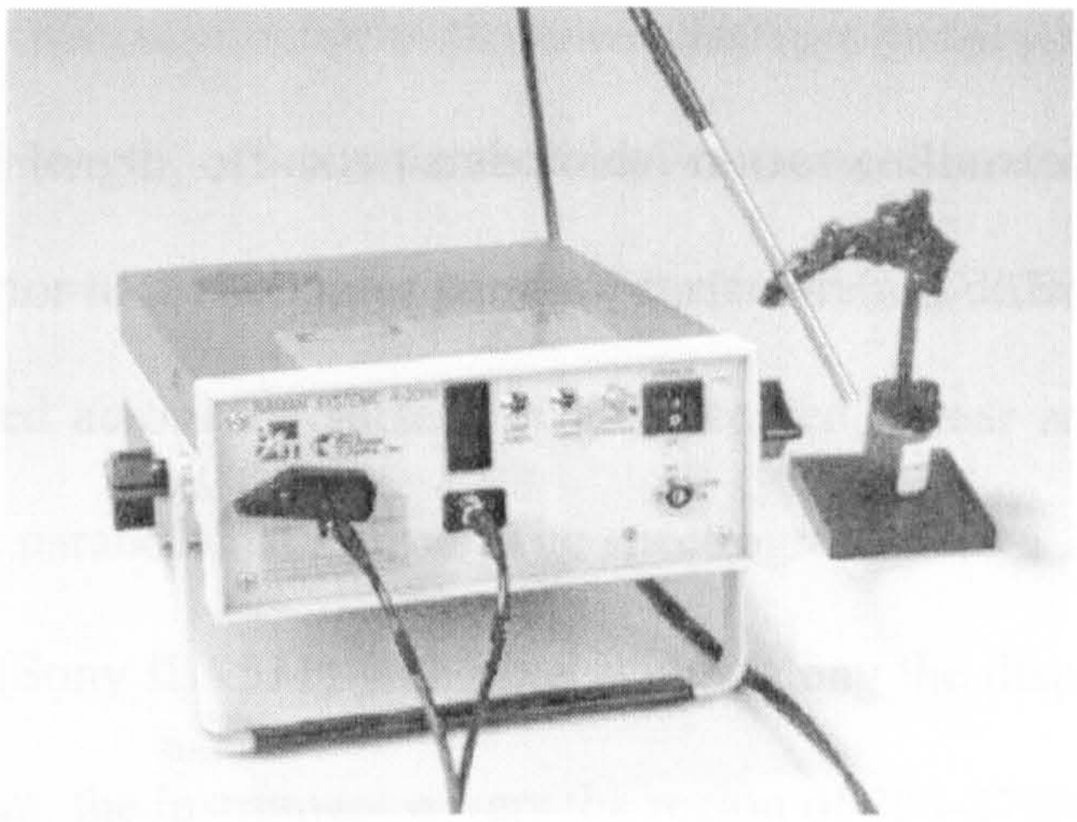

Figure 3.12 OceanOptics R2000 portable Raman spectrograph

The combination of exceedingly high excitation power without any intrinsically eye-safe sampling methodology (Class 3b) relegates this instrument to experienced users only. Laser excitation of 500mW at 785nm, (HPM500F1X12, Power Technology, Ark, US) is delivered to a compact, focussed probe-head, (EIC Laboratories, MA, US) via a 90μm core diameter, 0.22NA optical-fibre, (Polymicro Technologies). The distal end of the fibre is collimated using a 5mm focal length GRIN lens (NSG America, NJ, US), and band-pass filtered (Omega Optical Filters, 530ELPH) to attenuate Raman scattering. The collimated filtered beam is reflected off a filter at 45° (Omega Optical Filter, 550BP10) and focussed using a 5mm focal length achromatic lens to approximately a 90μm diameter spot at the sample. Scattered light is collected in 180° backscattering geometry and focussed into a 200μm core-diameter, 0.22NA optical fibre using a 10mm lens (Newport Corporation, KPX010). The increased fibre diameter

compensates for intrinsic imaging aberrations. The collection fibre transfers the flux to a proprietary crossed Czerny-Turner spectrograph, (S2000, OceanOptics, US).

A 42mm focal length, off-axis paraboloidal mirror collimates scattered light from the optical fibre prior to a 1200 lines per mm, surface-relief, diffraction grating. Dispersed light is focussed across the surface of an uncooled, linear array using a 68mm focal length off-axis paraboloidal mirror. The spectrograph uses a 2048 element linear array photodetector (Sony ILX511) with pixel width, along the dispersive axis, of 14μm. In this arrangement, the instrument covers the region of 200-2700cm^{-1}, with a resolution of 30cm^{-1} (FWHM). The detector has a read-noise of 250e^{-}/p RMS and dark noise that limits acquisition times to a maximum of 60s. The linear array output is acquired using a 12-bit ADC and recorded using a PC. The OceanOptics-supplied literature shows spectra obtained from benzene over a 10s integration period with a signal-to-noise ratio of 200 at 955cm^{-1}. Using the theory derived in Chapters 2 and 3, a signal-to-noise ratio of 4329 should be attainable, assuming shot-noise limited detector performance and an appropriately designed spectrograph. Although not discussed in this thesis, such an instrument was constructed, as illustrated in appendix A.

3.6 Conclusion

The lack of any realistically useful, or purpose-designed, commercial "off the shelf" packages for use in the field as a forensic analyser further compels the development of novel instrumentation. Optimisation of the instrument transmissivity, maximisation of the instrument etendue, correct matching of the spectrograph optics to an appropriate

detector and a stabilised laser source will greatly improve the performance of in-situ Raman analysis. It is worth noting that the interim period has seen considerable growth in the number of commercially available portable Raman spectrograph manufacturers[65-70], and that OceanOptics has released a second-generation instrument, with improved cooling and spectral resolution. This can only be seen as a justification of the work described in this thesis.

3.7 References

1. C.V. Raman, K.S. Krishnan, Nature, 1928, Volume 121, p 501.

2. H.L. Welsh, Canadian Journal of Physics, 1952, Volume 30, p 557.

3. R.M. Hoffman, F. Daniels, Journal of American Chemical Society, 1932, Volume 54, p 4226.

4. L.J. Buttolph, Review of Scientific Instruments, 1930, Volume 1, p 650.

5. S.P.S. Porto, D.L. Wood, Journal of Optical Society of America, 1962, Volume 52, p251.

6. S.P.S. Porto, D.L. Wood, Journal of Optical Society of America, 1963, Volume 53, p1446.

7. J. Loader, Appendix B In: *Basic Laser Raman Spectroscopy,* Heyden & Sons ltd, London, UK, 1970.

8. B. Yang, M. Morris, Applied Spectroscopy, 1991, Volume 45, pp1533-1536.

9. N. Perelman, Journal of Applied Physics, 1996, Volume 79, pp2839-2845.

10. R.T. Pogue, Applied Spectroscopy, 2000, Volume 54, pp12A-28A.

11. M. Futama, Applied Spectroscopy, 1996, Volume 50, pp199-204.

12. S.A. Asher, Spectroscopy, 1986, Volume 1, p26.

13. D. Long, *Raman Spectroscopy*, McGraw-Hill International Book Company, London, 1977.

14. P.J. Hendra, C. Jones, *Fourier Transform Raman Spectroscopy: Instrumentation and Chemical Applications,* Ellis Horwood Ltd, Chichester, UK, 1991.

15. M.J. Pelletier, R. Altkorn, Applied Spectroscopy, 2000, Volume 54, pp1837-1841.

16. X. Dou, Y. Yamaguchi, H. Yamamoto, Applied Spectroscopy, 2000, Volume 50, p 995-998.

17. J. Ferraro, K. Nakamoto, *Fluorescence Problem*, Chapter 2.7.5, In: *Introductory Raman Spectroscopy*, Academic Press, London, UK, 1994.

18. S.E.J. Bell, A. Dennis, E.S.O. Bourguignon, Analyst, 1998, Volume 123, pp1729-1734.

19. N. Everall, R.W. Jackson, Journal of Raman Spectroscopy, 1986, Volume 17, p415.

20. see Chapter 3.1.4 in reference 17.

21. R.C. Keir, E. Polwart, C. Davidson et al, Applied Spectroscopy, 2000, Volume 54, pp552-527.

22. C. Cheng, T.E Kirkbride, D. N. Batchelder, Journal of Forensic Science, 1995, Volume 40, pp31-37.

23. J. Akhavan, Spectrochimica Acta, 1991, Volume 47A, pp1247-1250.

24. C.C. Montarou, T.K. Gaylord, Applied Optics, 2000, Volume 39, pp5762-5767.

25. B. T. Bowie, D.B. Chase, P.R. Griffiths, Applied Spectroscopy, 2000, Volume 54, p 164A-173A.

26. D.M. Porterfield, A. Campion, Journal of American Chemical Society, 1988, Volume 110, p408.

27. InGaS Linear Array, JY Horiba, Lille, France.

28. H.S. Sands, I.P. Hayward, T.E. Kirkbride, Journal of Forensic Science, 1998, Volume 43, pp509-513.

29. J. Behringer, *Observed Resonance Raman Spectra.* In Szymanski H.A (Editor), *Raman Spectroscopy:Theory and Practise*, John Wiley & Sons, Chichester, UK.

30. 266nm Nanolaser, JDS Uniphase, 1768 Automation Parkway, San Jose, California 95131, USA.

31. Y. Wang, R. McCreery, Analytical Chemistry, 1989, Volume 62, p 2647.

32. J.M. Williamson, Applied Spectroscopy, 1989, Volume 43, p372-375.

33. K. Baldwin, D.N. Batchelder, Applied Spectroscopy, 2001, Volume 55, p517-524.

34. B. Schrader, *Infrared and Raman Spectroscopy,* VCH Verlagsgellschaft mBH, Cambridge, 1995.

35. C.L. Stevenson, T. Vo-Dinh, *Signal expressions in Raman spectroscopy.* In Laserna J.J (Editor) *Modern Techniques in Raman spectroscopy,* John Wiley & Sons, Chichester, UK, 1996.

36. M.D. Ray, A. Sedlacek, M. Wu, Review of Scientific Insturments, 2000, Volume 71, pp3485-3489.

37. B. Sagmuller, B. Schwarze, G. Brehm et al, Analyst, 2001, Volume 126, pp2066-2071.

38. J.M. Sylvia, J.A. Janni, J.D. Klein, et al, Analytical Chemistry, 2000, Volume 72, pp5834-5840.

39. R.A. Sulk, R.C. Corcoan, K.T. Carron, Applied Spectroscopy, 1999, Volume 53, pp954-959.

40. S.D. Schwab, R.L. McCreery, Analytical Chemistry, 1984, Volume 56, pp2199-2204.

41. M. Myrick, S.M. Angel, Applied Optics, 1999, Volume 30, pp795-805.

42. M.M Carrabba, D.R.Rauh, Patent Number US05112127, 1992.

43. B. Yang, M. Morris, H. Owen, Applied Spectroscopy, 1991, Volume 45, pp 512-513.

44. I.P. Hayward, T.E. Kirkbride, D.N. Batchelder, Journal of Forensic Science, 1995, Volume 40, pp883-884.

45. P. Niemela, J. Suhonen, Applied Spectroscopy, 2001, Volume 55, pp1337-1340.

46. M. Carrabba, Applied Spectroscopy, 1990, Volume 54, pp1558-1561.

47. C.L. Schoen, T.F. Cooney, S.K. Sharma, Applied Optics, 1992, Volume 31, pp7707-7715.

48. B.L. Mclain, J.Y. May, D. Ben-Amotz, Journal of Raman Spectroscopy, 1999, Volume 30, pp757-765.

49. B.L. Mclain, J.Y. May, D. Ben-Amotz, Applied Spectroscopy, 1999, Volume 53, pp1118-1122.

50. Microparts UV Spectrometer, STEAG microParts GmbH, Hauert 7 D 44227, Dortmund, Germany.

51. M.C. Hutley, Diffraction Gratings, Academic Press, London, 1982.

52. S.P. Davis, Diffraction Grating Spectrographs, New York Holt, Rinehart & Winston, 1970.

53. J.F. James , R.S. Sternberg, The Design of Optical Spectrometers, Chapman & Hall ltd, London, 1969.

54. N.T. Kawai, J.A. Janni, Spectroscopy, 2000, Volume 15, p32.

55. K.W. Busch, M..A. Busch, *Multielement Detection Systems for Spectrochemical Analysis,* John Wiley & Sons, Chichester, 1990.

56. K.J. Baldwin, D.N. Batchelder, B.J.E. Smith, Patent Number US5638173, 1997.

57. J.M. Tedesco, H. Owen, Chang, J. Byung, Patent Number US5011284, 1991.

58. C.A. Murray, S.B. Dierker, Journal of the Optical Society of America, 1986, Volume 12, pp2151-2159.

59. Ralcon Development Labs, South 400, West Box 142 Paradise, 84328, USA.

60. H.Sands, Ph.D Thesis, Leeds University, 1998.

61. M.L. Wach, G.Gervasio, Patent Number US05911017, 1999.

62. OceanOptics R-2001, OceanOptics, 380 Main Street, Dunedin, FL34698, USA.

63. OceanOptics S2000 Miniature Fibre Optic Spectrometers, OceanOptics, 380 Main Street, Dunedin, FL34698, USA.

64. Sony ILK511, Sony Corporation of America, New York, New York, USA.

65. Inphotote, InPhotonics, Inc. 111 Downey Street, Norwood, Massachusetts 02062, USA.

66. Foram-685, Foster & Freeman Ltd, 25 Swan Lane, Evesham, Worcestershire, WR11 4PE, UK.

67. Spectral Dimensions, Spectracode, Inc. Edward R. Grant, 1291 Cumberland Avenue, West Lafayette, Indiana 47906, USA.

68. RA 200, Renishaw Spectroscopy Products Division, Old Town, Wotton-under-Edge, Gloucestershire, GL12 7DW, UK.

69. Raman Analyser, Raman Systems, Inc. 108 Water Street, Suite 2L, Watertown, MA 02472, U.S.A.

70. PDA-200, GAMMA-METRICS, 5788 Pacific Center Blvd., San Diego California 92121, USA.

Chapter 4

Development of compact spectrometers for TNT vapour detection using SERRS

4.1 Introduction

The in-situ detection of explosives and their degradation products presents an extremely relevant analytical problem. To date, this has been achieved using either bulk detection methods, whereby electromagnetic radiation is used to invasively probe a suspect package, or vapour detection methods[1]. The latter are comparatively non-invasive, reliant upon the inherent volatility of the explosives to release sufficient molecules into the air, which are subsequently drawn into a detection system. Military-grade explosives, such as TNT, RDX and PETN have an extremely low vapour pressure, of the order of ppb (1 part in 10^9) to ppt (1 part in 10^{12}). Currently, vapour detection instrumentation in place at airport security checkpoints, relies upon methods of gas-chromatography, mass spectroscopy, ion-mobility spectroscopy or hybrids of these techniques. Although these offer sensitivity to explosives down to the ppt level, their physical construction has historically rendered them impractical for all but static applications and their poor selectivity reduces their effectiveness in discriminating against common interferent materials.

The use of Surface Enhanced Raman Spectroscopy (SERS) to achieve selective determination of trace-concentrations of 2,4,6 tri-nitro-toluene (TNT) and 2,4 di-nitro-toluene (DNT) has been reported previously[3-4] and used to develop a SERS-based DNT vapour detection system. Under blind testing, a detection of 5 ppb was reported, implying that vapour trace detection was unfeasible using SERS enhancement alone.

The use of Surface Enhanced Resonance Raman Spectroscopy (SERRS) has been reported in achieving the detection of a single molecule of a cyanine dye adsorbed in a silver colloidal solution[5]. This represents a new level of sensitivity, approximately 10^{-20}g in the sampling volume, with a molecularly specific spectrum that if applied to the detection of explosives affords a real improvement over current technologies. The use of SERRS to enhance the Raman scattering cross section of explosives has been a pressing subject of research, funded by the Department of Transport and the Regions (DETR) in the UK and has resulted in a collaboration between Strathclyde University, Leeds University and the PSDB. Of the explosives of primary concern, TNT has the highest saturation vapour pressure[2], and was established as the suitable first candidate. Since TNT does not possess a chromophore in the visible region and does not effectively adsorb onto silver colloidal surfaces[3], chemical modification of the explosive was necessary to fulfil the experimental requirements of SERRS. The development of a series of chemical reactions necessary to derivitise TNT molecules collected from vapour samples, and achieve adsorption onto a silver colloidal solution was performed at the Strathclyde Pure and Applied Chemistry Department and has been reported

previously[6]. At the time this project began, the development of the Janowsky reaction[7] had progressed sufficiently that a computer-controlled flow-cell arrangement had been constructed[8]. The system was quickly abandoned, as the sensitivity did not approach the necessary detection limits. Approximately 20 different derivitisation procedures have been attempted[6], the latest culminating in the production of an azo-derivitised TNT dye molecule. A robust test-bed system was constructed in conjunction with Strathclyde University[9], combining a series of flowcells with a Renishaw System 100 Raman spectrograph.

Since the chemistry and instrumentation required to implement an automated flowcell was under constant development, the aim of this project was to implement an optimised optical system and to investigate the feasibility of TNT vapour detection using data supplied by Strathclyde University. This was achieved by modelling the signal-to-noise ratio of TNT-specific peaks at various concentrations and calculating a limit of detection. An investigation of waveguide-enhanced sampling, excitation power, optical component performance and various spectrograph arrangements was performed to establish improvements in signal-to-noise ratio. A spectrograph was designed for the purpose of concept demonstration, in fulfilment of the commercial requirements of this DETR-funded project. It was a commercial requirement of the project that detection be achieved using a spectrograph, since the same instrumentation was envisaged for use in the eventual detection of RDX and PETN vapours using SERRS. From this point, the system described in this chapter shall be referred to as the S^2R^5 spectrograph, in

reference to the initial DETR-project designation. The experimental characteristics of the S^2R^5 spectrograph are presented and compared with theoretically derived results.

4.2 Feasibility Study

The Azo-chemistry flow cell system was developed in collaboration with the PSDB and Strathclyde University and is reported elsewhere[9]. The system produces two spectra, corresponding to the conditions of "TNT Detected" and "TNT Not Detected". These are shown in figure 4.1.

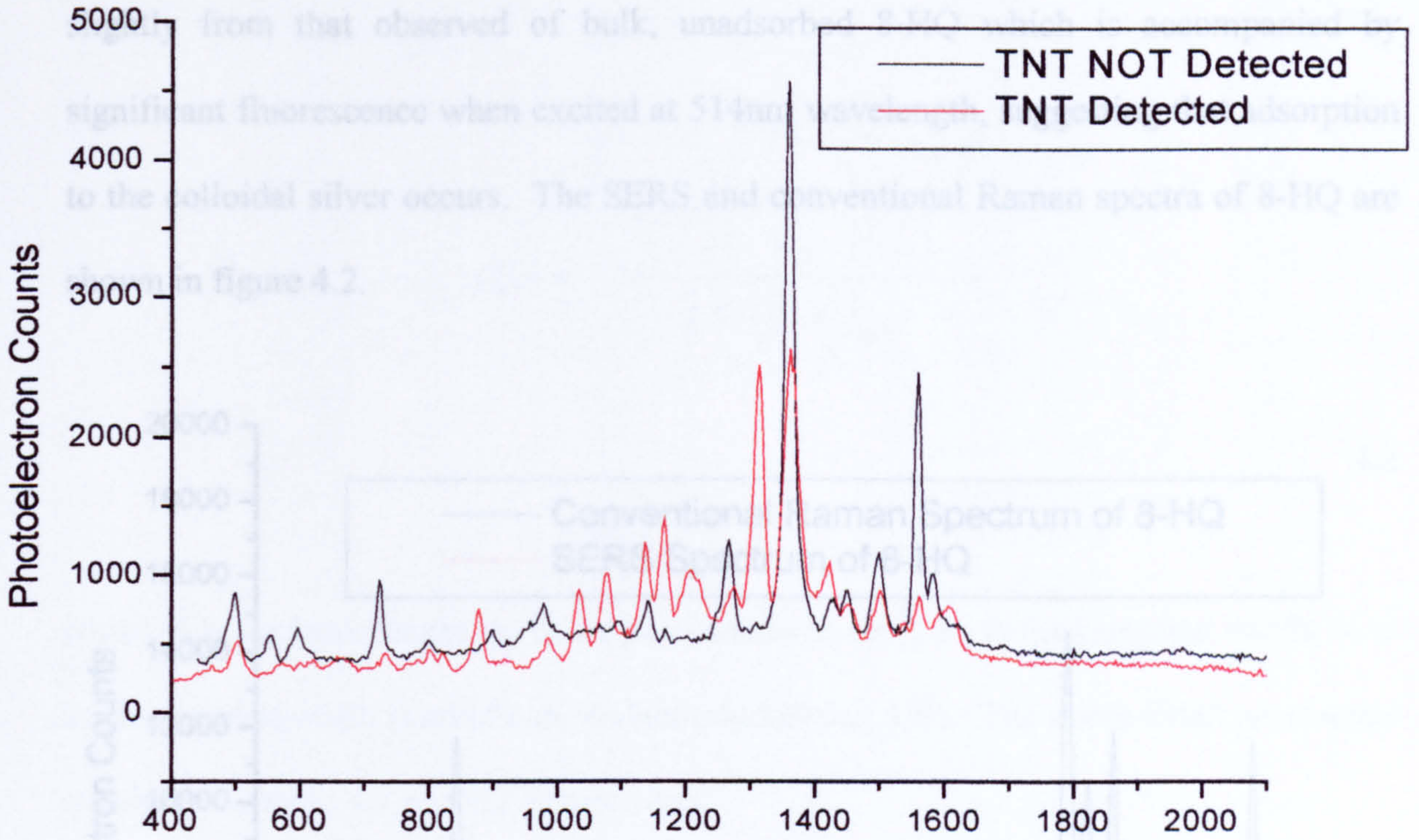

Figure 4.1 SERRS spectra from flowcell system

Experimental Conditions:

Excitation:	3.2mW at 514nm wavelength
Collection Objective:	x20 (Olympus MSPLAN)
8HQ Concentration:	$1x10^{-4}M$
TNT Concentration:	$1x10^{-5}M$
Integration Time:	10s

8-hydroxy-quinoline (8-HQ), the main flow cell reagent produces peaks that appear in both spectra. The position of Raman bands in the 8-HQ SERS spectrum are shifted slightly from that observed of bulk, unadsorbed 8-HQ which is accompanied by significant fluorescence when excited at 514nm wavelength, suggesting that adsorption to the colloidal silver occurs. The SERS and conventional Raman spectra of 8-HQ are shown in figure 4.2.

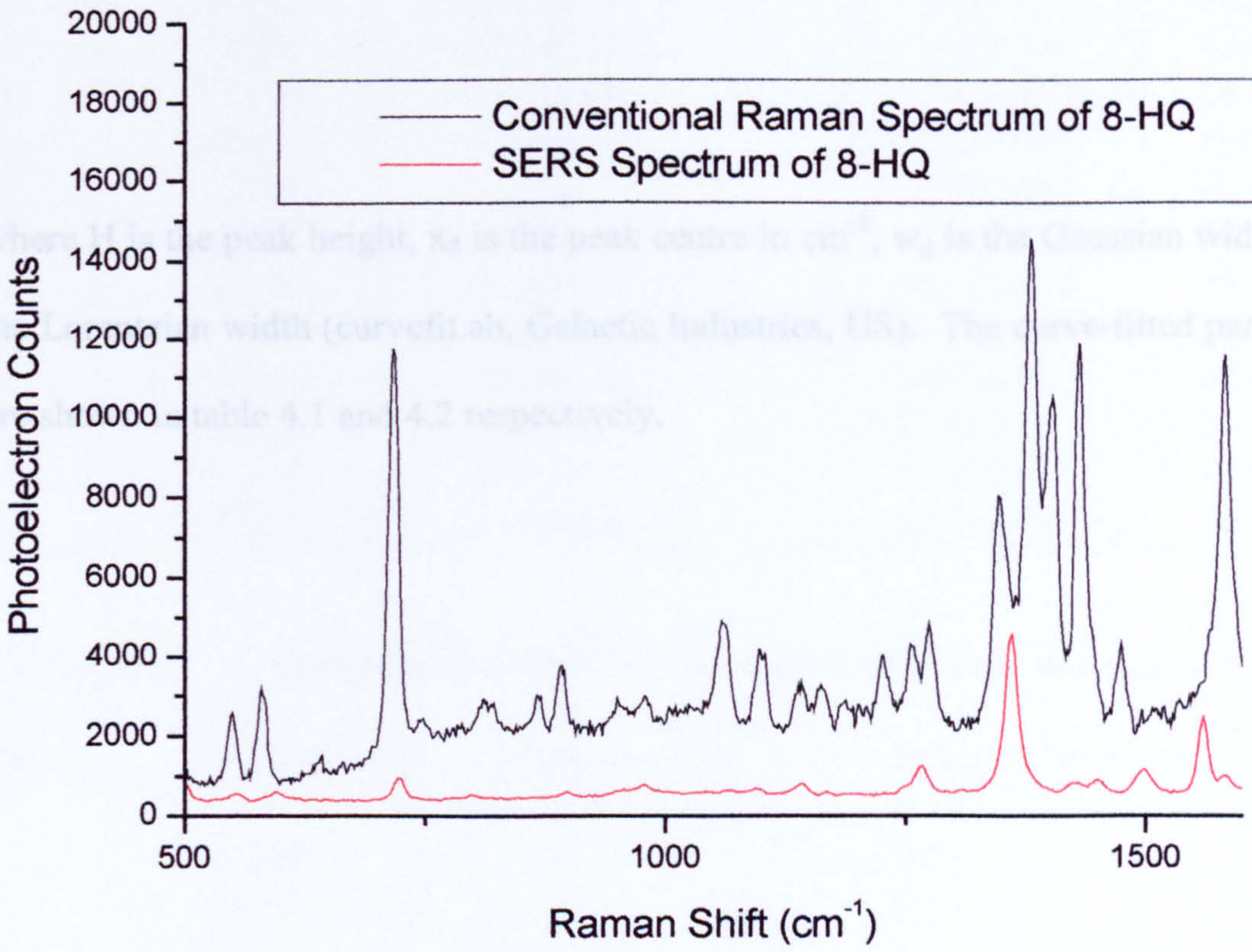

Figure 4.2 SERS and conventional Raman spectra of 8-HQ.

Conventional Raman spectrum is background subtracted.

The position of Raman bands of the 8-HQ SERS spectrum and TNT SERRS spectrum in figure 4.2 were curve-fitted using a Voigt function defined in equation 4.1.

$$f(x) = \frac{\int_{-\infty}^{\infty} \frac{H \exp(-y^2)}{w_g^{\,2} + \left[\left(\frac{x - x_0}{w_g}\right) - y\right]^2} dy}{\int_{-\infty}^{\infty} \frac{\exp(-y^2)}{w_l^{\,2} + y^2} dy} \qquad \textbf{4.1}$$

where H is the peak height, x_0 is the peak centre in cm^{-1}, w_g is the Gaussian width, w_l is the Lorentzian width (curvefit.ab, Galactic Industries, US). The curve-fitted parameters are shown in table 4.1 and 4.2 respectively.

Table 4.1 Curve-fitted 8-HQ Raman bands

Peak	Centre (cm^{-1})	Height (counts)	Width (cm^{-1})	Area
1	496	509±107	19.5±8.52	13136
2	553.3	189±103	15.2±9.99	3081
3	595.9	235±97.7	22.3±16.7	7959
4	722.8	598±125	12.0±4.13	11173
5	798	105±6.09	16.9±1.84	2598
6	897.2	114±5.94	14.3±0.899	1973
7	975.2	244±4.71	39.6±1.4	14397
8	1096	92.2±7.14	11.5±1.11	1138
9	1140	256±5.65	15.6±0.432	4286
10	1247.8	140±11.4	9.96±0.890	1491
11	1266.4	688±9.88	17.2±0.290	13484
12	1360.5	4120±11.4	16.0±0.062	93659
13	1427.2	255±8.4	17.6±0.716	4767
14	1450.1	322±8.59	16.12±0.52	5529
15	1498.0	612±10.3	20.5±0.395	15433
16	1530.1	49.4±14.5	3.01±0.01	243
17	1559.8	1894±11.7	12.8±0.10	29956
18	1582.9	456±10.4	15.3±0.611	10701
19	1615.1	114±6.06	36.0±2.64	4400

Table 4.2 Curve-fitted Raman bands in TNT Spectrum not assigned to 8HQ

Peak	Centre (cm^{-1})	Height (counts)	Relative Intensity
1	867	18.3±2.00	0.19
2	1028.5	11.8±1.95	0.24
3	1069.1	18.2±1.02	0.54
4	1307	14.6±0.92	1.0

The concentration dependence of the SERRS scattered flux is shown in figure 4.3. 0.5ml volumes of stock solutions, comprising 2,4,6-tri-nitro-toluene dissolved in acetic acid in the concentration range $1x10^{-8}$ to $1x10^{-5}$moles/litre, were used to simulate the collection of TNT vapour.

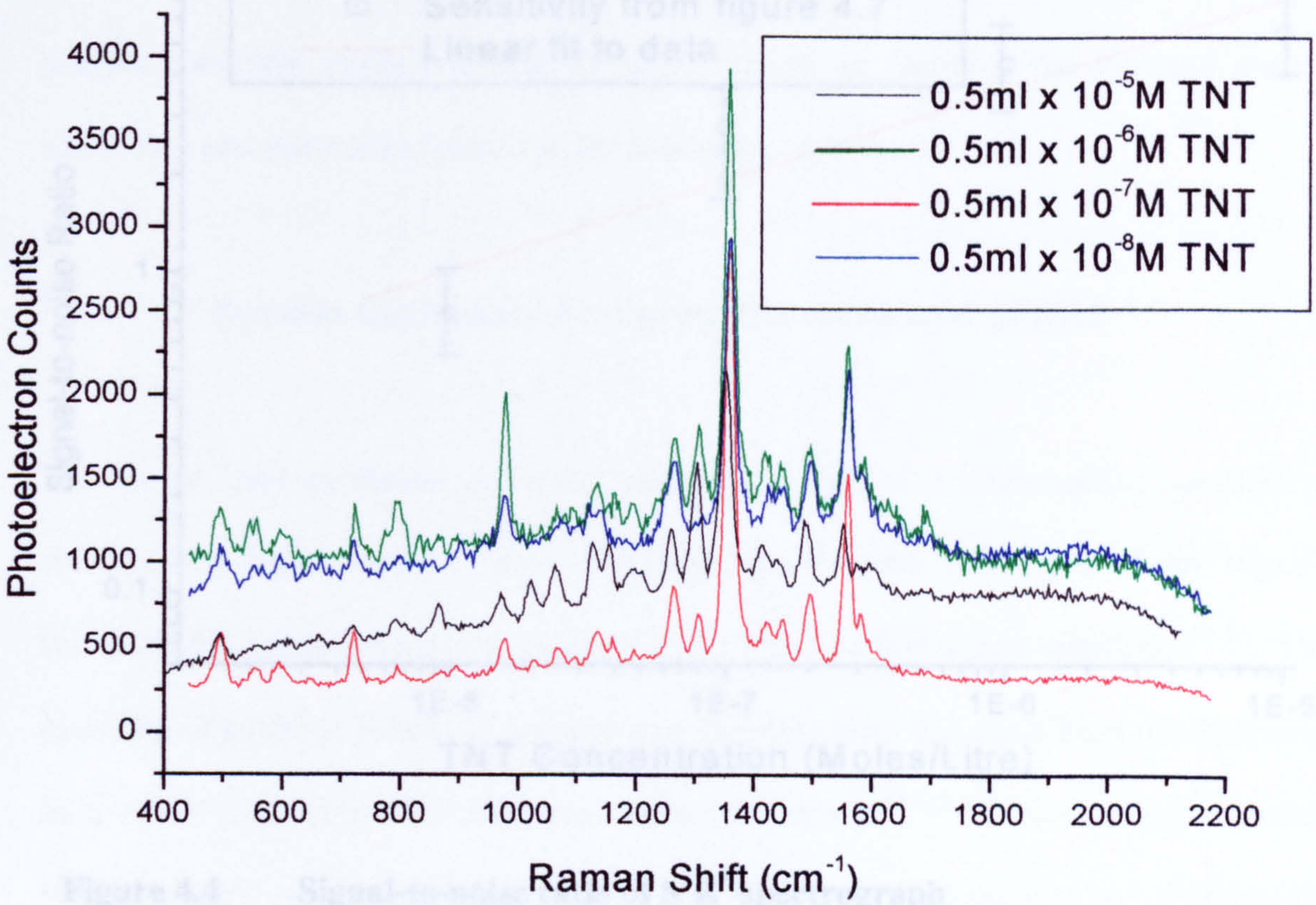

Figure 4.3 SERRS spectra of TNT at various concentrations

Experimental:

Excitation: 3.2mW at 514nm wavelength

Collection Objective: x20 (Olympus MSPLAN)

Integration Time: 10s

The system sensitivity is illustrated in figure 4.4, determined by calculating the signal-to-noise ratio of the TNT peak at 1307cm^{-1} at each concentration and plotting this with respect to the sample concentration. The limit of detection was established at the point where the signal-to-noise ratio of the peak at 1307cm^{-1} above the background was 3.0.

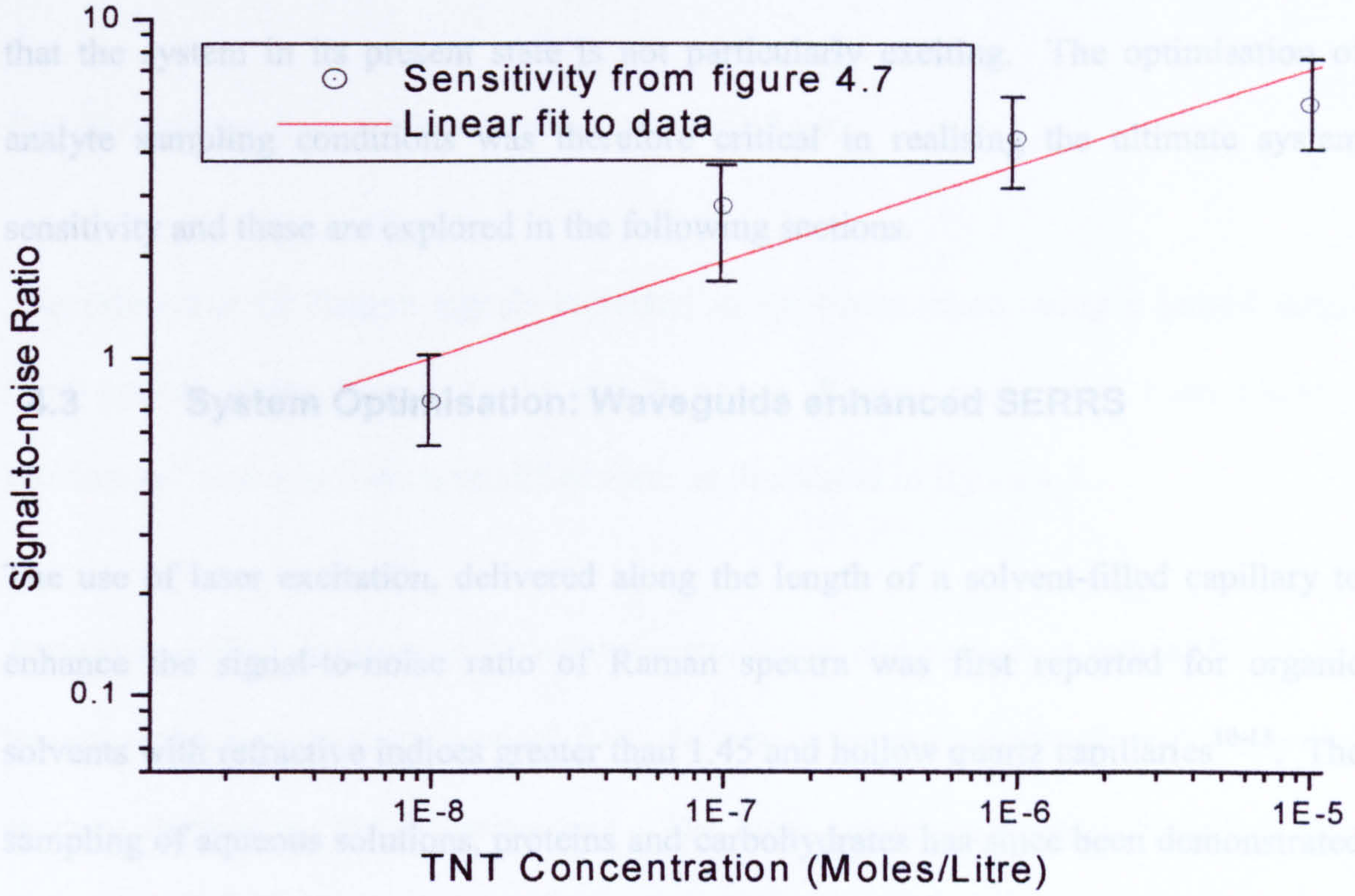

Figure 4.4 Signal-to-noise ratio of S^2R^5 spectrograph

Table 4.3 Linear Fit Data from Figure 4.4

Parameter	Value	Error
A	2.96	0.44
B	0.38	0.07

R=0.97

Yscale(Y)=A+B*xscale(X); Where scale() is the axis scale function.

From figure 4.4, the limit of detection occurs at a TNT concentration of (3.06 ± 0.12) x10^{-7}moles/litre. A 0.5ml volume of TNT stock solution at this concentration corresponds to an equivalent mass of (3.40 ± 0.14)x10^{-8}g of TNT. The state of the art TNT vapour detection limits of current GC-MS systems is typically 10^{-12}g, suggesting that the system in its present state is not particularly exciting. The optimisation of analyte sampling conditions was therefore critical in realising the ultimate system sensitivity and these are explored in the following sections.

4.3 System Optimisation: Waveguide enhanced SERRS

The use of laser excitation, delivered along the length of a solvent-filled capillary to enhance the signal-to-noise ratio of Raman spectra was first reported for organic solvents with refractive indices greater than 1.45 and hollow quartz capillaries[10-13]. The sampling of aqueous solutions, proteins and carbohydrates has since been demonstrated as a result of improved Teflon processing procedures[14-18]. Waveguiding enhances Raman spectra by increasing the sampling depth, d, and hence the number of molecules probed by the laser. Sample self-absorption was anticipated to be a particularly relevant issue in the study of analytes using SERRS since the silver colloidal solution strongly absorbs in the visible spectrum.

The aim of this section was to investigate the enhancement of Raman spectra afforded using an epi-illumination waveguided arrangement compared to those recorded using

the original arrangement used by Strathclyde University[7]. These results were then compared with theoretically derived modelling.

4.3.1 Background

Epi-illumination Raman signals collection calculation

The estimation of Raman signals collected in epi-illumination using a lensed single fibre optical probe, analogous to the Renishaw Raman probe, has been reported previously[19] and was used in modified form as illustrated in figure 4.5.

Assuming perfect registration between the excitation and collection optical fibres, the image of the laser delivery optical fibre defines a "virtual aperture", with numerical aperture defined by the focussing lens. The laser excitation density, described by a Gaussian normalised distribution function, g(r,h) generates Raman scattering at each elemental area in a plane at height h over a circle of radius r_h. The integrated sample radiance, L_R, normalised for unity molecular number density and unity Raman scattering cross section, was calculated in 4 separate volumes by computing the solid angle of collection at each point in elemental planes within the sample and integrating over the sample depth above and below the virtual aperture according to;

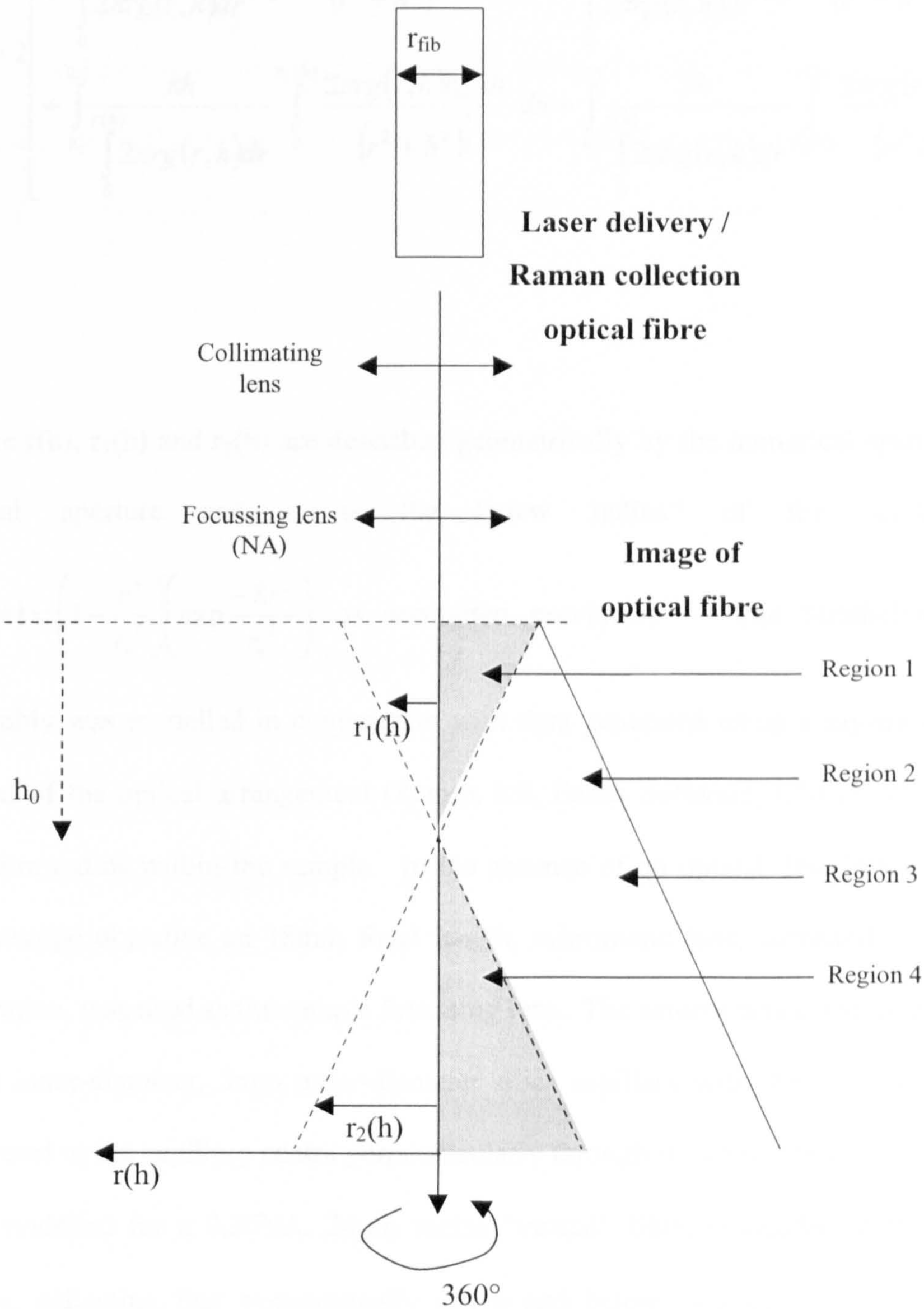

Figure 4.5 Optical fibre collection model

$$L_R = 2\left[\int_0^{h_0}\frac{\pi h}{\int_0^{r(h)}2\pi r g(r,h)dr}\int_0^{r_1(h)}\frac{2\pi r g(r,h){r_{1v}}^2 dr}{\left(r^2+h^2\right)^{\frac{3}{2}}}dh+\int_0^{h_0}\frac{\pi h}{\int_0^{r(h)}2\pi r g(r,h)dr}\int_{r1h}^{r(h)}\frac{2\pi r g(r,h){r_{2v}}^2 dr}{\left(r^2+h^2\right)^{\frac{3}{2}}}dh\right.$$
$$\left.+\int_{h_0}^{0.5}\frac{\pi h}{\int_0^{r(h)}2\pi r g(r,h)dr}\int_0^{r_2(h)}\frac{2\pi r g(r,h){r_{3v}}^2 dr}{\left(r^2+h^2\right)^{\frac{3}{2}}}dh+\int_{h_0}^{0.5}\frac{\pi h}{\int_0^{r(h)}2\pi r g(r,h)dr}\int_{r_2(h)}^{r(h)}\frac{2\pi r g(r,h){r_{4v}}^2 dr}{\left(r^2+h^2\right)^{\frac{3}{2}}}dh\right]$$

4.2

where r(h), $r_1(h)$ and $r_2(h)$ are described geometrically by the numerical aperture of the virtual aperture and r_v is the "view radius" of the aperture and $g(r,h)=\left(1-\frac{r^4}{r_h^4}\right)\left(\exp\frac{-8r^2}{r_h^2}\right)$ as accounted previously[19]. The Strathclyde optical assembly was modelled in conjunction with data generated using a ray-traced optical model of the optical arrangement (Zemax 9.0, Focus Software, US) to determine the aperture radius within the sample. In the absence of an optical description for a x10 microscope objective an 18mm focal length, achromatic lens, corrected for spherical aberration, was used as the sample focussing lens. The sample was constrained within a 1mm inner-diameter, 3mm outer-diameter silica capillary with the focused excitation delivered to the capillary centre perpendicularly through the capillary wall. The system was modelled for a 0.36NA, 24μm radius "virtual" fibre, embedded at the capillary centre, collecting flux symmetrically above and below to a depth of 0.5mm. The numerical integration was achieved using Simpson's rule over 100 equal segments using Maple 7.0.

Waveguided Raman signal collection calculation

The calculation of Raman signals collected using a Teflon AF waveguide under epi-illumination has been reported previously for absorbing samples and was modelled for the liquid core optical fibre and the bulk silver colloid as the core analyte according to;

$$L_R = \frac{\pi\left(n^2_{sample} - 1.29^2\right)\frac{1}{2\alpha}e^{(-2\alpha l)}}{n^2_{sample}} \qquad \textbf{4.3}$$

where n_{sample} is the refractive index of the analyte, α is the sample absorptivity and l is the length of the waveguide. A complete derivation is available elsewhere[18]. The silver colloidal solution was considered as an optically homogeneous solution with bulk absorption properties described by figure 4.6 and a refractive index of 1.33 (water). The UV absorption of the TNT derivitised dye is shown in figure 4.7 and was expected to make negligible contribution to the characteristics of the typical analyte since the Azo-TNT concentration is typically very low and does little to alter the colloidal solution aggregation state[8]. The extinction spectrum of the silver colloidal solution is influenced by light absorption due to resonant excitation of surface plasmons on the silver particles[8]. The typical particle diameter of unaggregated silver particles comprising the silver colloidal solution is <40nm and so extinction from scattering was presumed negligible[8].

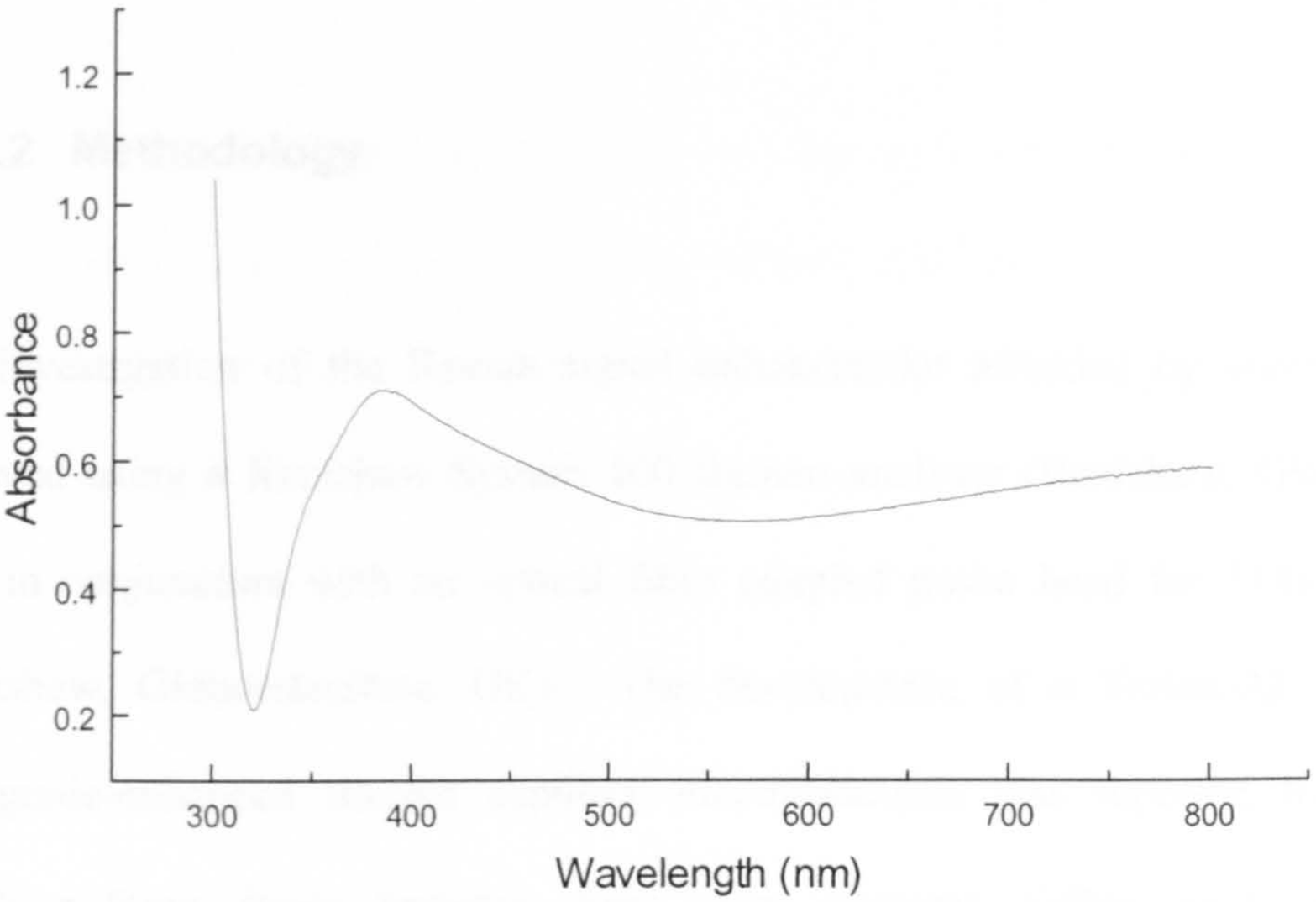

Figure 4.6 UV-Visible absorbance spectrum of silver colloid (Sampled using Perkin Elmer UV-VIS Lambda 60)

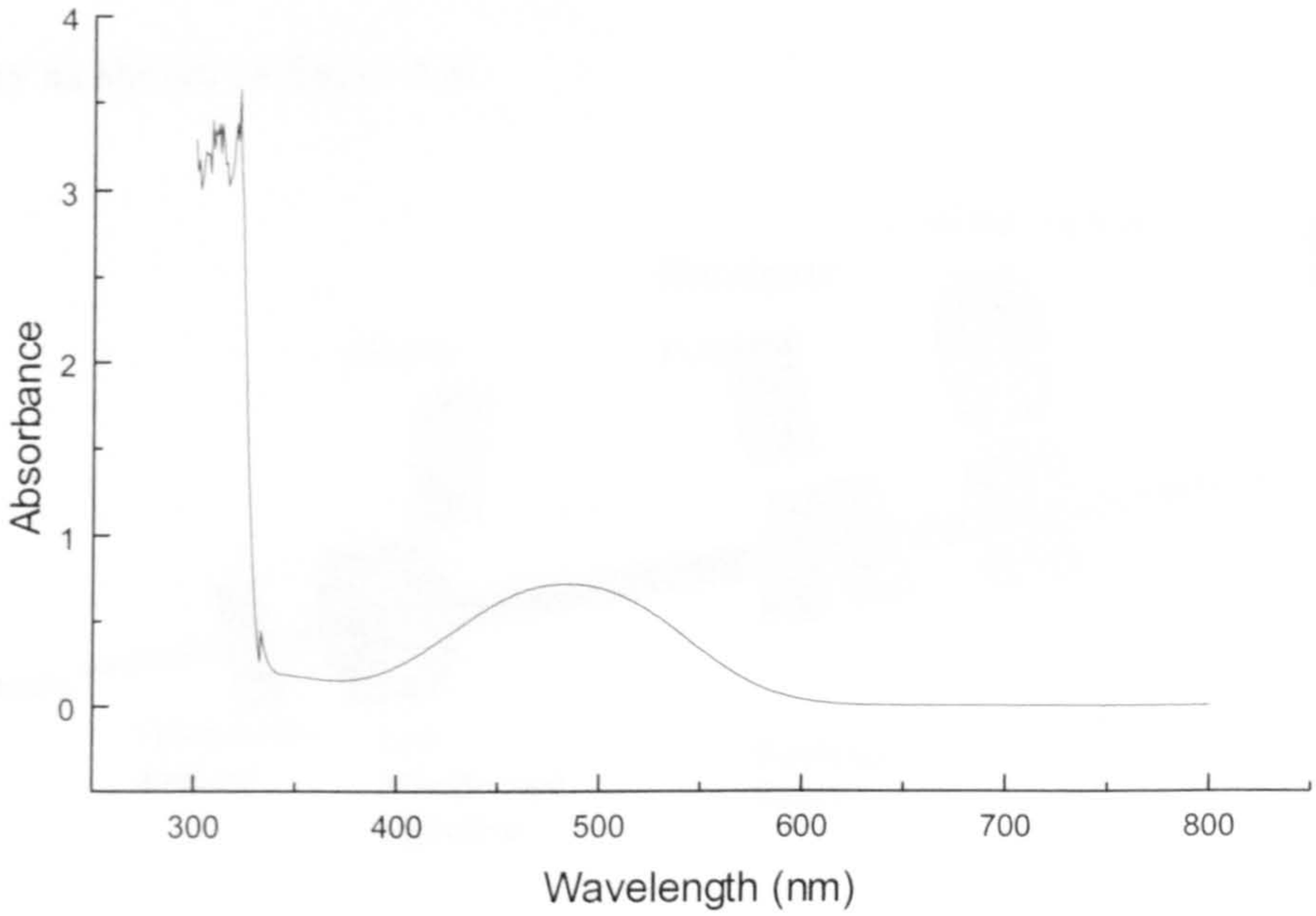

Figure 4.7 UV-Visible absorbance of TNT-Azo in Acetone ($7.9x10^{-5}M$) (Sampled using Perkin Elmer UV-VIS Lambda 60)

4.3.2 Methodology

The investigation of the Raman signal enhancement afforded by waveguiding was achieved using a Renishaw System 100 Raman analyser (Renishaw, Gloucestershire, UK) in conjunction with an optical fibre coupled probe head for 514nm excitation (Renishaw, Gloucestershire, UK). The development of a Teflon-AF flowcell for waveguide-enhanced Raman capillary electrophoresis was reported by Ruddick[18]. Briefly a 50μm inner diameter, 3mm outer diameter, Teflon AF™ capillary was constrained at one end in a modified 1/16" high-pressure liquid chromatography tee. A 100μm thick fused-silica window was mounted in a stainless-steel unit such that the excitation could be focussed through the window and into the proximal end of the capillary as shown in figure 4.8.

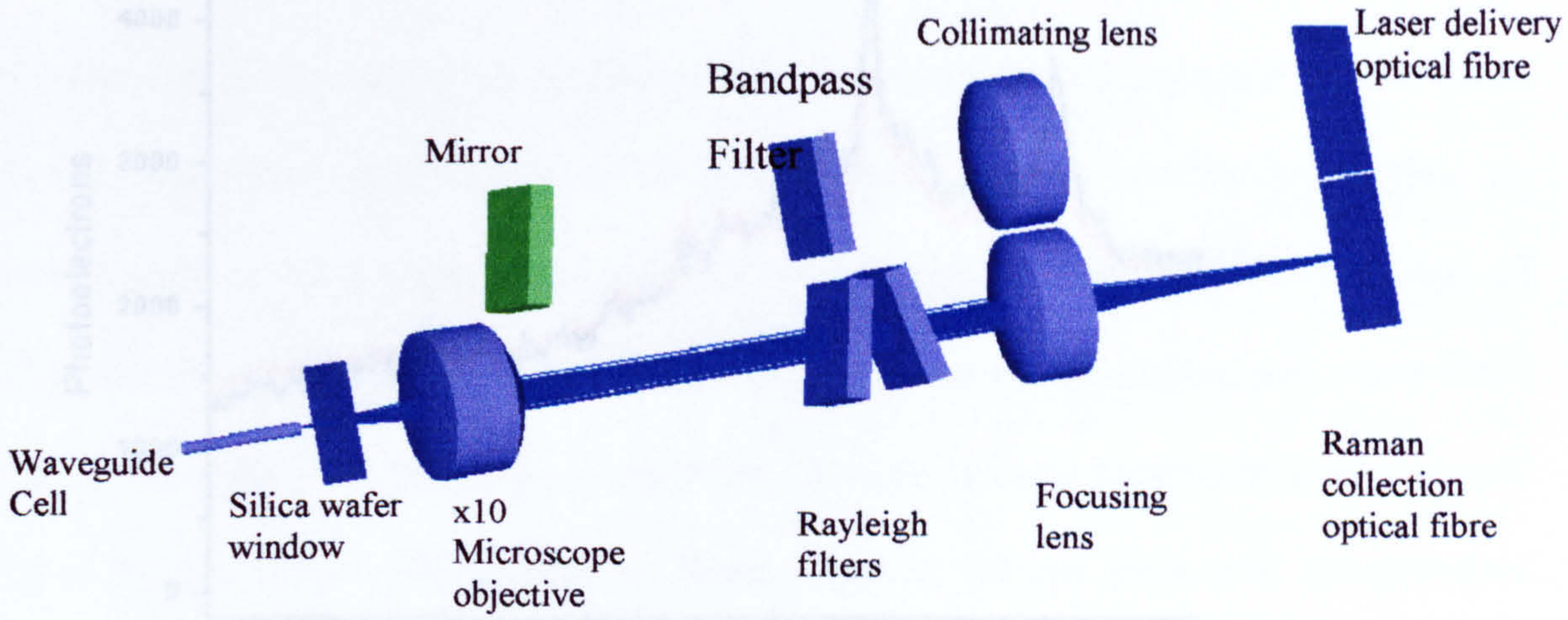

Figure 4.8 Waveguide sampling arrangement

The cell was sealed using a Teflon wafer and mounted on a three-axis translation stage enabling optimisation of the excitation delivery and scattering collection using the optical fibre probe head in conjunction with a x10 microscope objective. Equivalent volumes of 8-HQ and silver colloidal solution were injected into the waveguide cell using an HPLC pump (Hewlett Packard). Once three spectra were acquired of the SERS analyte, the HPLC stream was then used to fill a 1mm internal diameter, fused-silica capillary. The optical fibre coupled laser was focussed into the analyte volume through the capillary wall and Raman scattered light collected in 180° backscattering geometry. The averaged spectra from each sampling method are shown in figure 4.9.

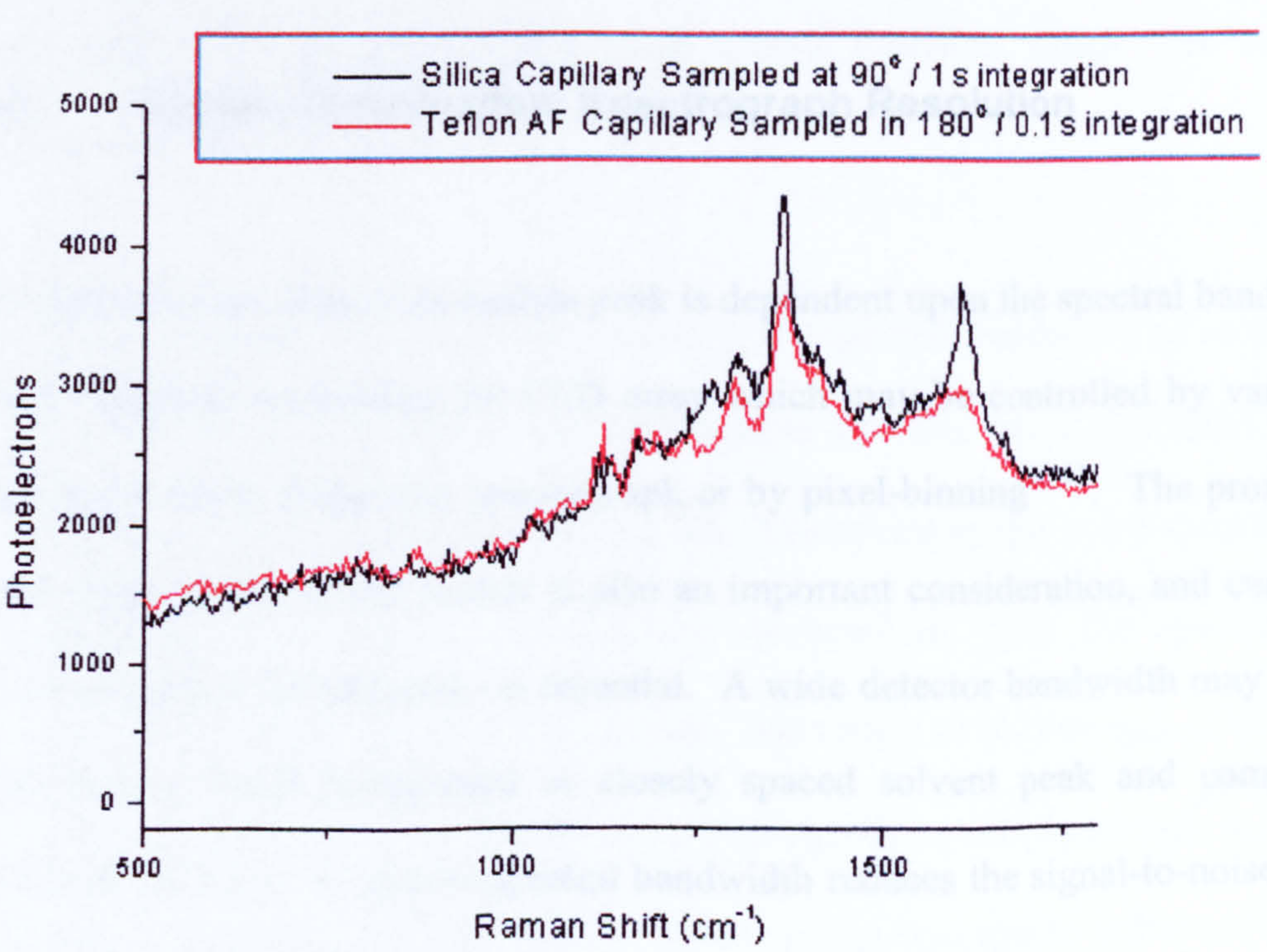

Figure 4.9 Raman spectra acquired using waveguided and non-waveguided methods

From figure 4.9, the waveguided sampling achieves an enhancement factor of 12 over the standard epi-illumination geometry. The enhancement factor is approximately constant across the Raman spectral region and also enhances the broad fluorescence background. This compares reasonably well with the theoretically derived value of 15.6. An explanation for this discrepancy is that there may not be perfect registration between the excitation and collection optical paths. Additionally, poor alignment of the optical probe with the core of the waveguide, or the deposition of silver colloid on the inner surface of the waveguide may cause significant losses. The use of a waveguiding sampling arrangement affords an order of magnitude increase in signal and should form a key component of a SERRS optical arrangement.

4.4 System Optimisation: Spectrograph Resolution

The signal-to-noise ratio of an analyte peak is dependent upon the spectral bandwidth of discrete elements comprising the CCD array which may be controlled by varying the spectrograph linear dispersion spectrograph or by pixel-binning[20-21]. The proximity of solvent peaks to an analyte feature is also an important consideration, and curve-fitted data of the typical solvent peaks is essential. A wide detector bandwidth may integrate signal from a broad background or closely spaced solvent peak and compromises signal-to-noise ratio. A narrow spectral bandwidth reduces the signal-to-noise ratio by reducing the amount of signal detected. The optimisation of spectrograph resolution is therefore important.

The analyte spectral intensity, $\phi_a(\lambda)$, as a function of detector position using a dispersive arrangement is the convolution of the laser intensity profile, $\phi_{ex}(\lambda)$, the spectrograph point spread function, $\phi_{opt}(\lambda)$, and the natural spectrum of the sample, $\phi_{natural}(\lambda)$ such that;

$$\phi_a(\lambda) = \phi_{ex}(\lambda) \otimes \phi_{opt}(\lambda) \otimes \phi_{natural}(\lambda) \qquad \textbf{4.4}$$

For the purpose of this investigation, the excitation spectral bandwidth is so small it was unresolvable from the spectrograph point spread function, which was considered constant across the detector array.

The effects of reduced dispersion on increasing the spectral bandwidth of each detector pixel and on the signal-to-ratio of the TNT peak at 1307cm^{-1} were simulated using the spectrum, $\phi_a(\lambda)$ shown in figure 4.3 at 10^{-6}M. The spectrograph point-spread function (effectively the laser intensity profile) was deconvolved from the spectrum using Fourier self-deconvolution (GRAMS, Galactic Industries) to resolve $\phi_{natural}(\lambda)$. Various spectrograph dispersions were simulated by binning the natural spectrum, $\phi_{natural}(\lambda)$ by factors of 2,,4 and 8. In anticipation of either of the waveguide enhanced sampling geometry's considered in section 4.3, the spectrograph point-spread function was not

expected to change significantly. The spectra were reconvolved with the original spectrograph point-spread function, $\phi_{opt}(\lambda)$ to produce the spectra shown in figure 4.10.

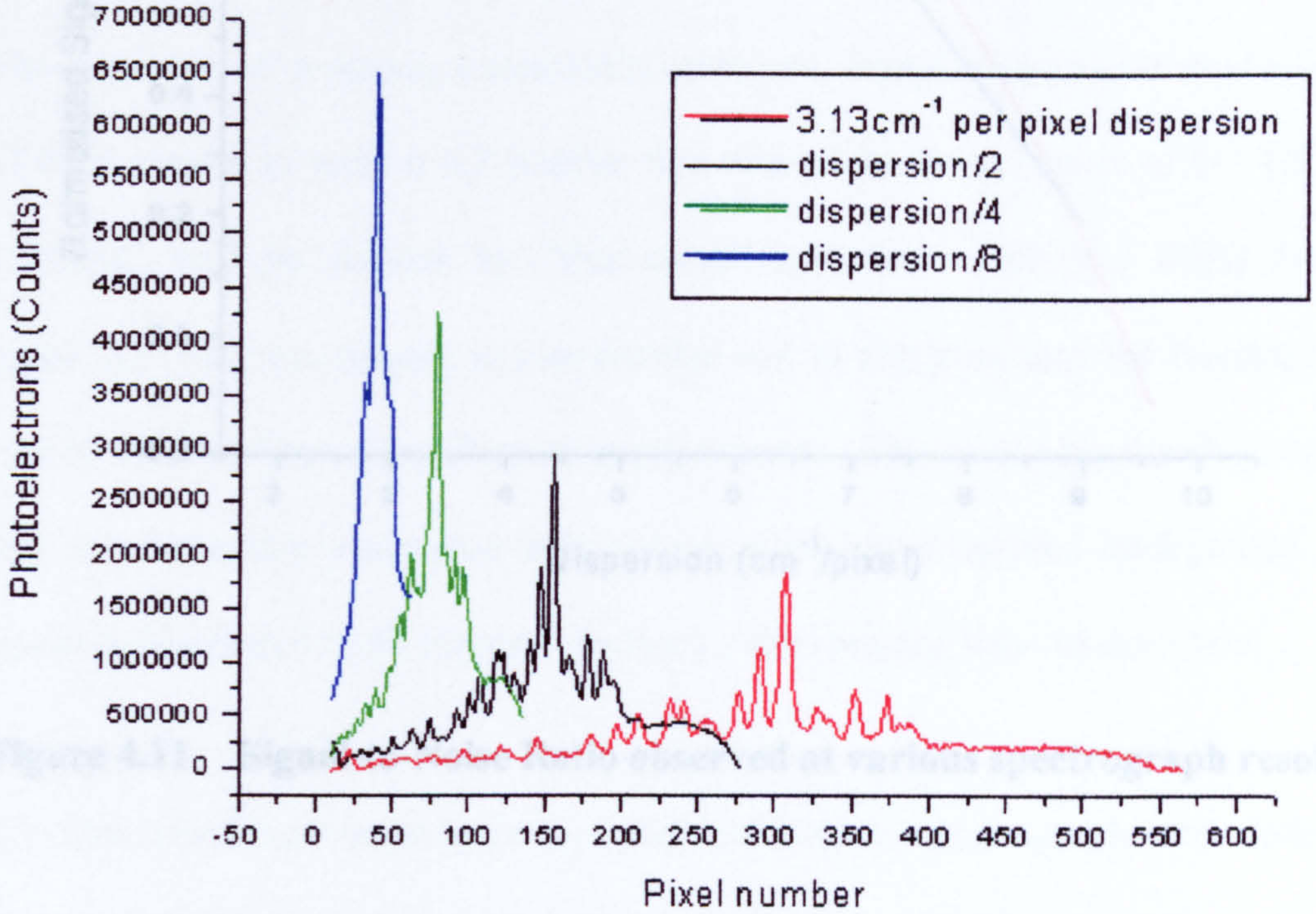

Figure 4.10 Simulated TNT spectra at decreasing spectrograph resolution

The signal-to-noise ratio of the TNT peak at 1307cm^{-1} in each spectrum was curve-fitted and is shown in figure 4.11.

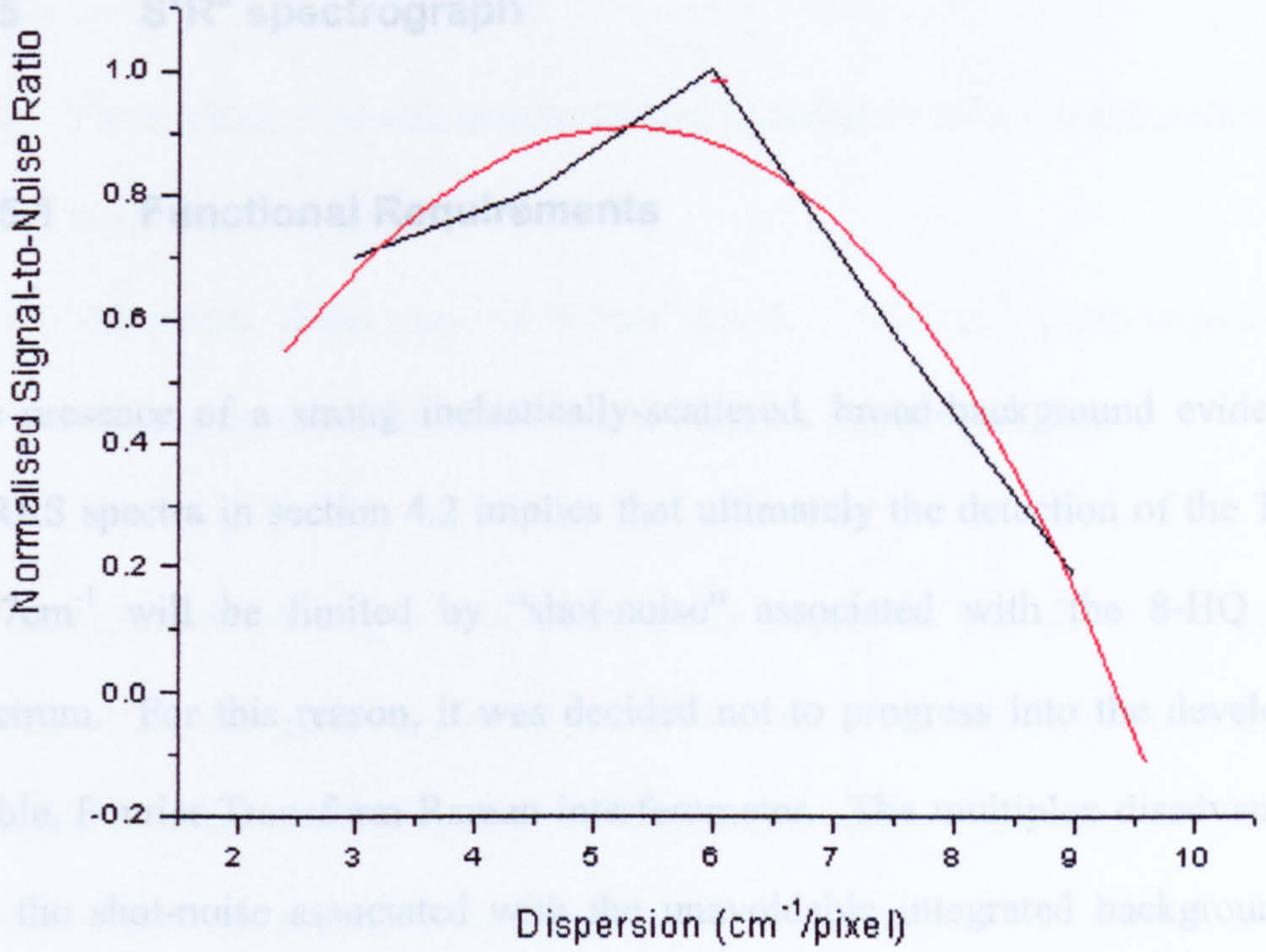

Figure 4.11 Signal-to-Noise Ratio observed at various spectrograph resolutions

From figure 4.11 the optimum signal-to-noise ratio occurs when employing a pixel-pixel resolution of 5.6cm^{-1}. This affords an improvement in signal-to-noise ratio of approximately 20% over the Strathclyde system, whilst retaining the ability to resolve the TNT peak from the background spectrum. This is not a significant increase in performance, and it was decided that a resolution of 1.75cm^{-1} per pixel would be necessary to fulfil the commercial requirements of Renishaw to develop a general purpose portable concept demonstrator instrument.

4.5 S^2R^5 spectrograph

4.5.1 Functional Requirements

The presence of a strong inelastically-scattered, broad-background evidenced in the SERRS spectra in section 4.2 implies that ultimately the detection of the TNT peak at 1307cm^{-1} will be limited by "shot-noise" associated with the 8-HQ background spectrum. For this reason, it was decided not to progress into the development of a visible, Fourier-Transform Raman interferometer. The multiplex disadvantage applies and the shot-noise associated with the unavoidable integrated background spectrum signal is distributed to all Fourier channels, degrading the limit of detection.

The functional requirements for an optimised Raman spectrograph were deduced from the preliminary study using the Renishaw System 100 analyser. In anticipation of waveguided, axial illumination and 90° collection, these are in summary:

- The spectrograph must be capable of recording the spectrally-resolved image of a 12 x 0.05mm area, comprising the TNT analyte constrained within a 50μm core diameter Teflon AF™ optical waveguide.
- Spectral range of at least 1000cm^{-1} from 700cm^{-1} to 1700cm^{-1} using 532nm excitation in anticipation of the development of RDX and PETN selective chemistries.

- The excitation wavelength is defined to coincide with the absorption structure of the derivitised dye.
- Maximum dispersion of 5.6cm^{-1}/pixel. 1.75cm^{-1} pixel-to-pixel resolution required by Renishaw for General Purpose Raman Analyser.

For commercial reasons, it was additionally important that the entire instrument be housed within a single laptop-sized briefcase (Peli Products, US). The minimisation of instrument weight and profile were central to this theme. The option to perform remote measurements using optical fibre connections up to 100m was also necessary so that multiple sampling stations could be installed within a large airport terminal.

4.5.2 Probe Head

The choice of an excitation source for the SERRS spectroscopy was limited by commercial as well as practical constraints. The requirements were;

- Wavelength:532nm to coincide with the absorption maximum of the analyte dye.
- High power:80mW or greater to enable greater scattering.
- Air-cooled operation.

In addition, it was a commercial requirement that the laser satisfy the following criteria so that it could be integrated into their current commercial range of instruments;

- Polarisation: 500:1 or better
- Stability (Power):1% RMS
- Single Longitudinal Mode Operation at TEM_{00}

As part of a commercially motivated instrumentation development project, it was essential to work with a laser manufacturer to provide a commercially viable excitation source. The laser identified primarily on cost grounds, was the Elforlight G4, (Elforlight, UK). The laser output was investigated at high resolution using a Renishaw System 1000 spectrograph. Initial work identified the presence of a broad, residual emission at 810nm, corresponding to the diode laser used to pump the Neodymium-Vanadate lasing crystal. Additional emissions were observed, displaced from the laser line in the Stokes scattered region at multiples of $127cm^{-1}$. This was attributed to the transmission of broadband fluorescence through an etalon used to define the laser cavity. These emissions were attenuated using an short-pass filter with an optical density of 8 whilst transmitting the laser wavelengths preferentially.

The requirement for remote sampling was central to the flexibility of the SERRS detection system commercially. It was essential that the sampling head be capable of remote connection over long distances. For commercial reasons, it was decided to use a

Renishaw Compact optical fibre probe as the sampling probe. The optical arrangement had previously been refined from earlier designs and is described in chapter 3. The measured attenuation characteristics of the laser bandpass filter are presented in chapter 3.

4.5.3 Spectrograph Design

The large numerical aperture of the optical fibres (0.22-0.27NA) used to couple the probe head to the spectrograph precluded the use of commercially-available concave diffraction gratings since none were available with sufficient numerical aperture.

The simplest spectrograph design was to use a lens to collimate the output of the optical fibre and direct it onto a surface-relief diffraction grating. The dispersed light was then focussed onto the CCD array detector.

The relationship between the lens focal lengths, diffraction grating groove density, and the grating orientation, was solved iteratively using an Excel spreadsheet to produce an appropriate instrument. The necessary incidence angle, θ_I, onto the grating was determined according to equation 4.5.

$$\theta_I = \frac{\theta_{inc}}{2} + \cos^{-1}\left(\frac{m\lambda_{cl}}{2d\cos\left(\frac{\theta_{inc}}{2}\right)}\right) \qquad 4.5$$

Where λ_{cl} is the wavelength in nm units diffracted to the CCD centre; d is the grating spacing in nm; θ_{inc} is the included angle between the incident and diffracted ray at λ_{cl}.

The requirement for good imaging quality across the complete area of the CCD camera (12.7 x 8mm), whilst maintaining the smallest instrument profile, precludes the use of short focal length achromatic lenses to collimate and focus the dispersed Raman scattered flux. Preliminary modelling using Zemax 9.1 identified that comatic aberrations and distortion were severe at wide fields of view for 50mm focal length achromatic lenses. The imaging quality of high-speed CCTV camera lenses was reviewed since these are typically used for wide field of view imaging security applications at high resolution. A 50mm focal length CCTV lens (Cosmicar,C25014, Japan) was selected as it offered a high MTF across the area of the CCD camera at high spatial frequencies and negligible distortion. The manufacturer-supplied data applies to photographic imaging at infinity and does not specifically apply to this application.

The instrument design parameters are summarised in table 4.5.

Table 4.5 Spectrograph summary

Collimating Lens		**CCD Focussing Lens**	
Focal Length	50mm	**Focal Length**	50mm
F# Number	1.4	**CCD Chip**	
Diffraction Grating		**Pixel Size**	0.022mm
Lines	2400 l/mm	**No of pixels**	578
Order	-1		
Incidence Angle	-25.07°		
Central Wavelength	568.27nm		
Include Angle	45°		
Spectral Range	1105.20cm^{-1}		

The constructed spectrograph, combined with optical fibre connector, is shown in figure 4.12.

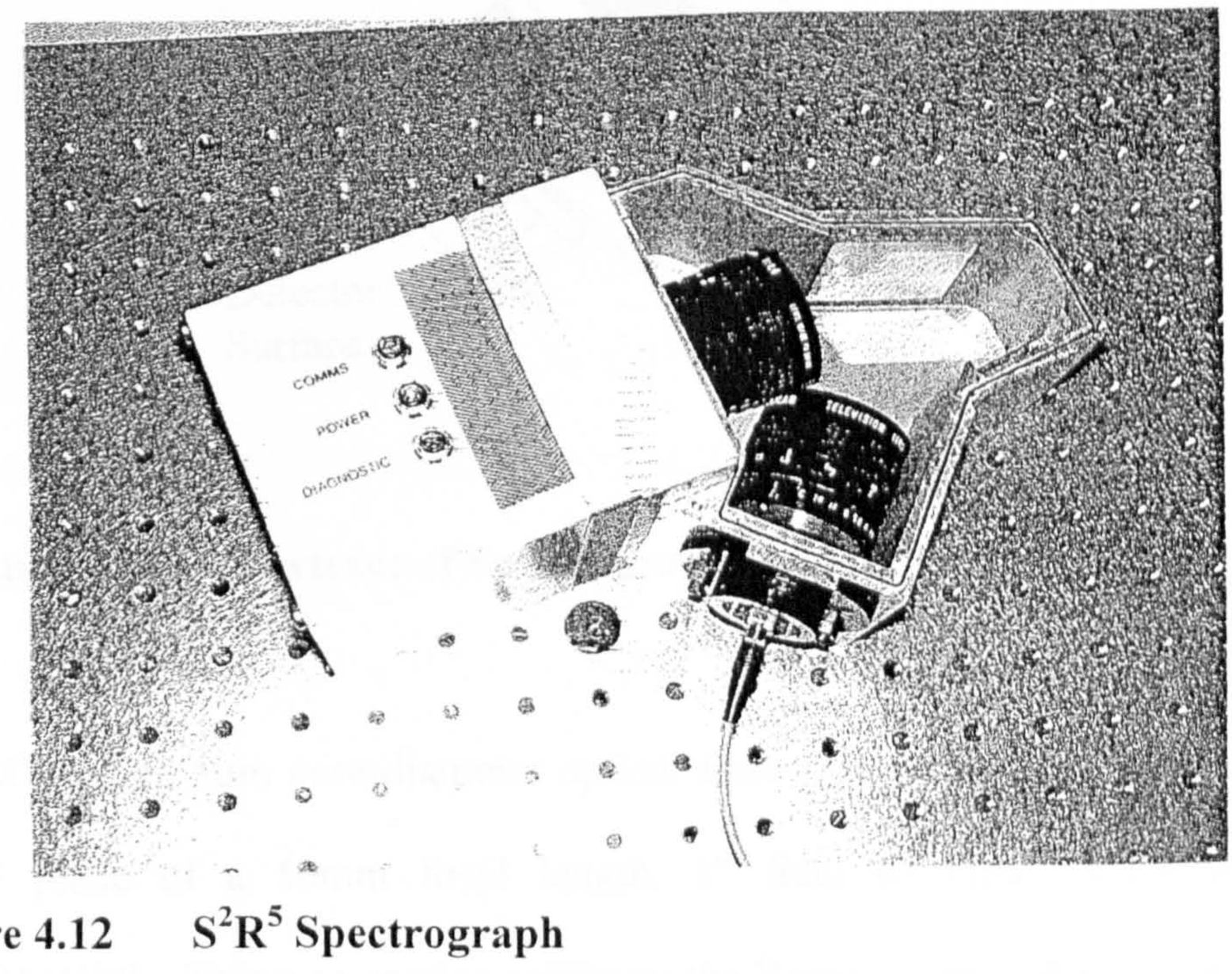

Figure 4.12 S^2R^5 Spectrograph

The optical layout of the S^2R^5 spectrograph was modelled using Zemax 9.1, (Focus Software, US) using data supplied from the lens manufacturer. Due to the proprietary

nature of the lens design, the complete lens prescription has been withheld. The optical layout is shown in figure 4.13.

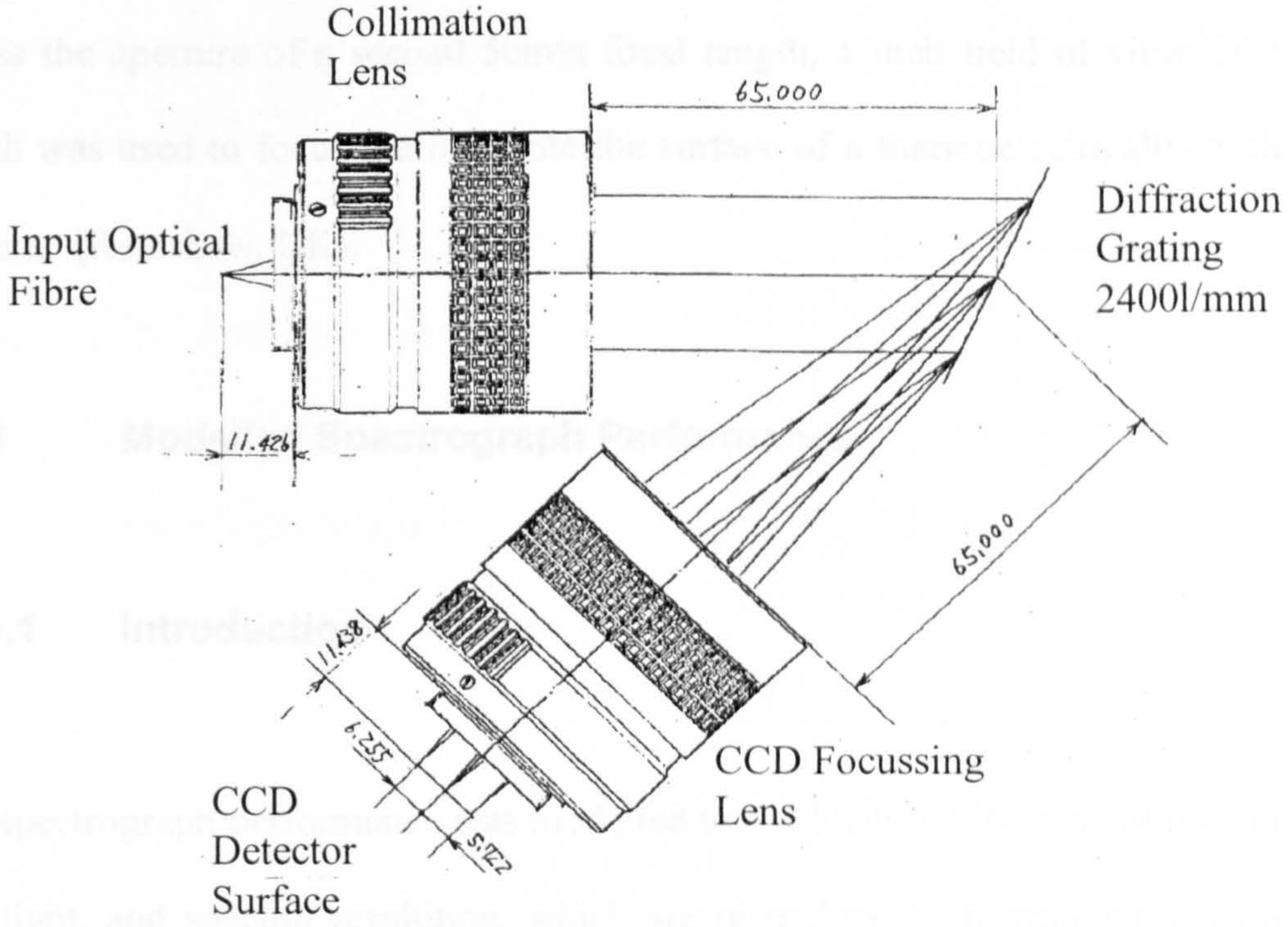

Figure 4.13 Raytrace of Spectrograph

A 0.27NA, 62.5μm core diameter optical fibre (Fibrecom, UK) was positioned at the focal plane of a 50mm focal length, 1" field of view CCTV lens (Cosmicar, C25014VIS). This was used to collimate the Raman scattered flux and direct it onto a 2400 lines per mm holographically blazed surface-relief diffraction grating (Optometrics, 2400VIS). A holographic-grating was chosen over a ruled grating since

straylight and ghost defects generated by these gratings are negligible compared to their ruled equivalents. The optical fibre output was modelled by defining a 62.5μm diameter aperture at the focal plane of the collimating lens, and displacing a 0.27NA Gaussian profile source behind the aperture. The diffraction grating disperses light across the aperture of a second 50mm focal length, 1 inch field of view CCTV lens, which was used to focus the flux onto the surface of a thermoelectrically-cooled CCD camera. (Renishaw, UK).

4.6 Modelled Spectrograph Performance

4.6.1 Introduction

The spectrograph performance was modelled to establish the instrument transmissivity, straylight, and spectral resolution, which are related to the instrument sensitivity and specificity respectively. Combined with the signal-to-noise ratio data obtained from the SERRS analyte at varying TNT concentrations, the aim of this section was to deduce the ultimate detection limit of the instrument.

4.6.2 White light Response Function

Zemax 9.1 was used to investigate the theoretical response of the spectrograph to white light, so that regions of poor instrument sensitivity could be identified. This was achieved by calculating the instrument transmissivity for points at the centre of the object plane, and the two extreme object field points, corresponding to the lateral extent of the optical fibre. The computed white light profile shown in figure 4.14 is the product of the diffraction grating efficiency, the CCD quantum efficiency, the optics transmission and the instrument vignetting function averaged over the three points. The computed white light spectrum is normalised to 0.127, representing the maximum absolute transmission of the spectrograph.

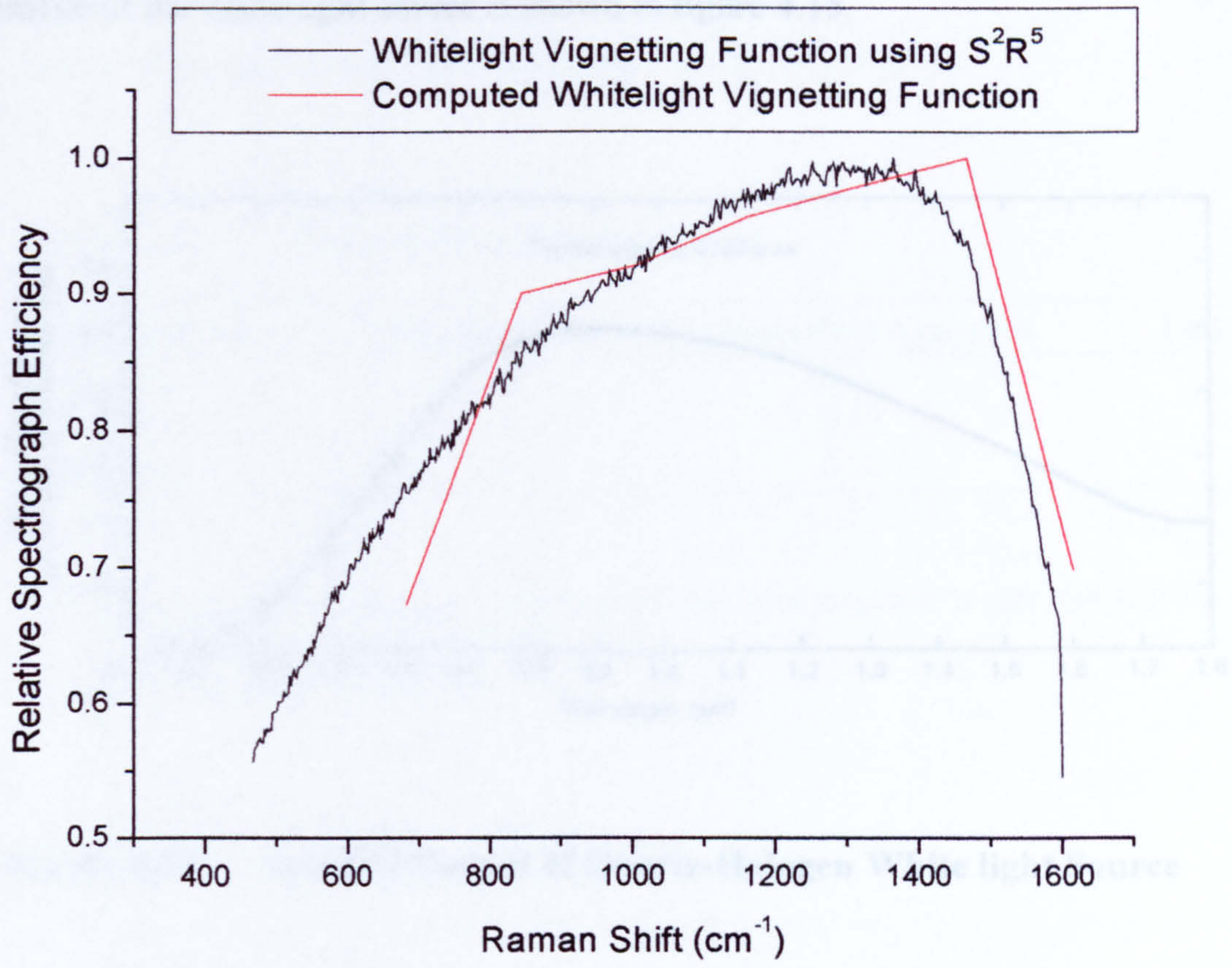

Figure 4.14 Absolute Efficiency of Spectrograph

Computed white light spectrum normalised to 0.127 efficiency
Sampled Parameters
CCD0206 Quantum Efficiency; 2400 lines per mm VIS optimised grating; vignetting and lens transmission functions.

The white light profile shown in figure 4.14 was measured using a halogen white light source. A 3mm focal length achromatic lens (Oz-optics, US) was used to focus white light from a 100W Quartz Halogen bulb, (633 100WQTH, Oriel Corporation, US) into a 50μm core diameter, 0.22NA optical fibre, (Fibrecore, UK). The achromatic lens was

positioned approximately 10cm from the filament surface. The manufacturer-supplied profile of the white light source is shown in figure 4.15.

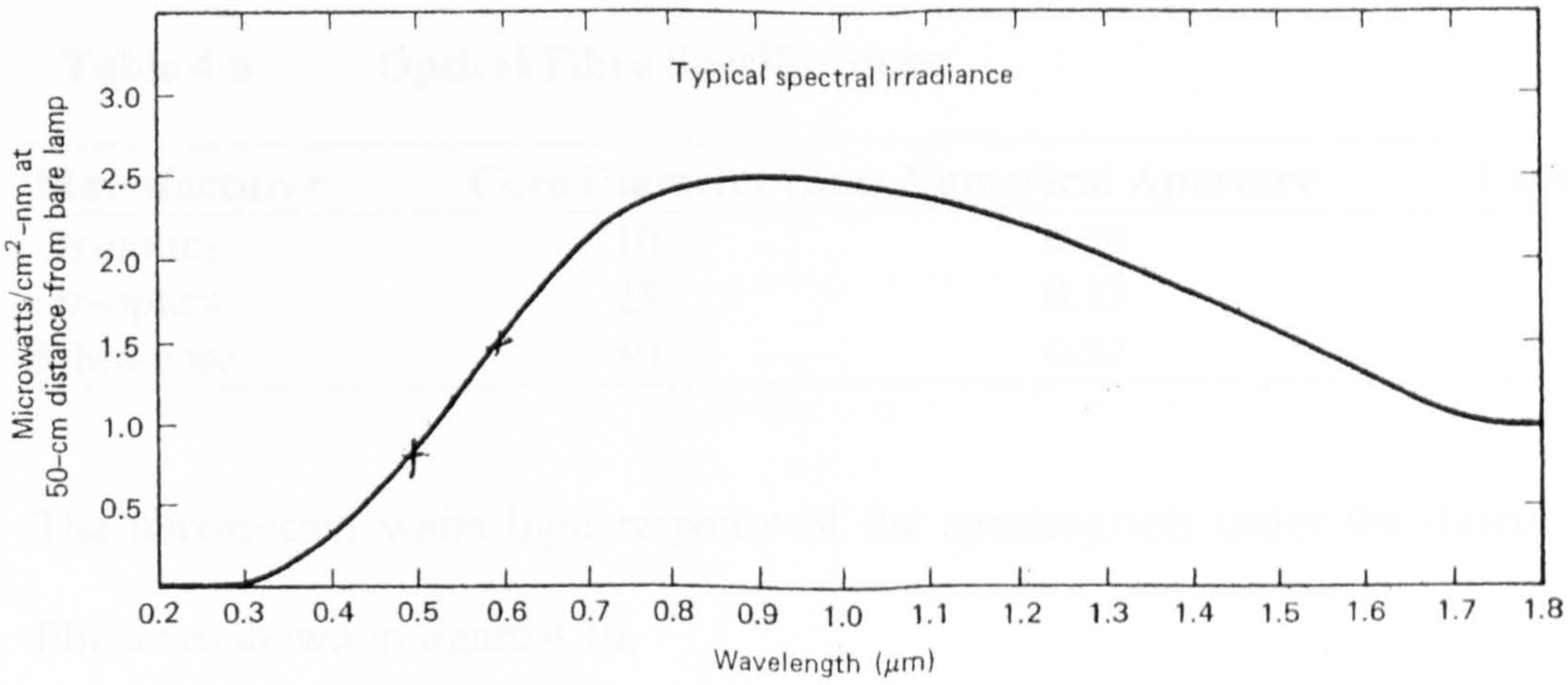

Figure 4.15 Spectral Output of Quartz-Halogen White light Source

The distal end of the optical fibre was connected, using an fc-pc connector, to the 50μm core diameter optical fibre that was connected to the spectrograph entrance aperture. The spectrum obtained was corrected for the spectral irradiance of the halogen source.

The modelled spectrograph performance in figure 4.14, compares favourably with the experimentally derived data for Raman shifts greater than $700cm^{-1}$. The non-linear white light profile of the spectrograph has a sufficiently broad sensitivity region between $800cm^{-1}$ and $1500cm^{-1}$ with an absolute efficiency in the range 9-12%. Fortunately, this encompasses the important spectral features in the analyte spectrum.

The vignetting function of the spectrograph was investigated using various optical fibres of various numerical apertures. The optical fibres shown in table 4.6 were connected in turn to the 50μm optical fibre and coupled to the spectrograph.

Table 4.6 Optical Fibre Specifications

Manufacturer	Core Diameter (μm)	Numerical Aperture	Length (m)
Oz-optics	10	0.10	5
Oz-optics	25	0.13	5
Fibre-core	50	0.22	5

The uncorrected white light response of the spectrograph under the different optical fibres are shown in figure 4.16.

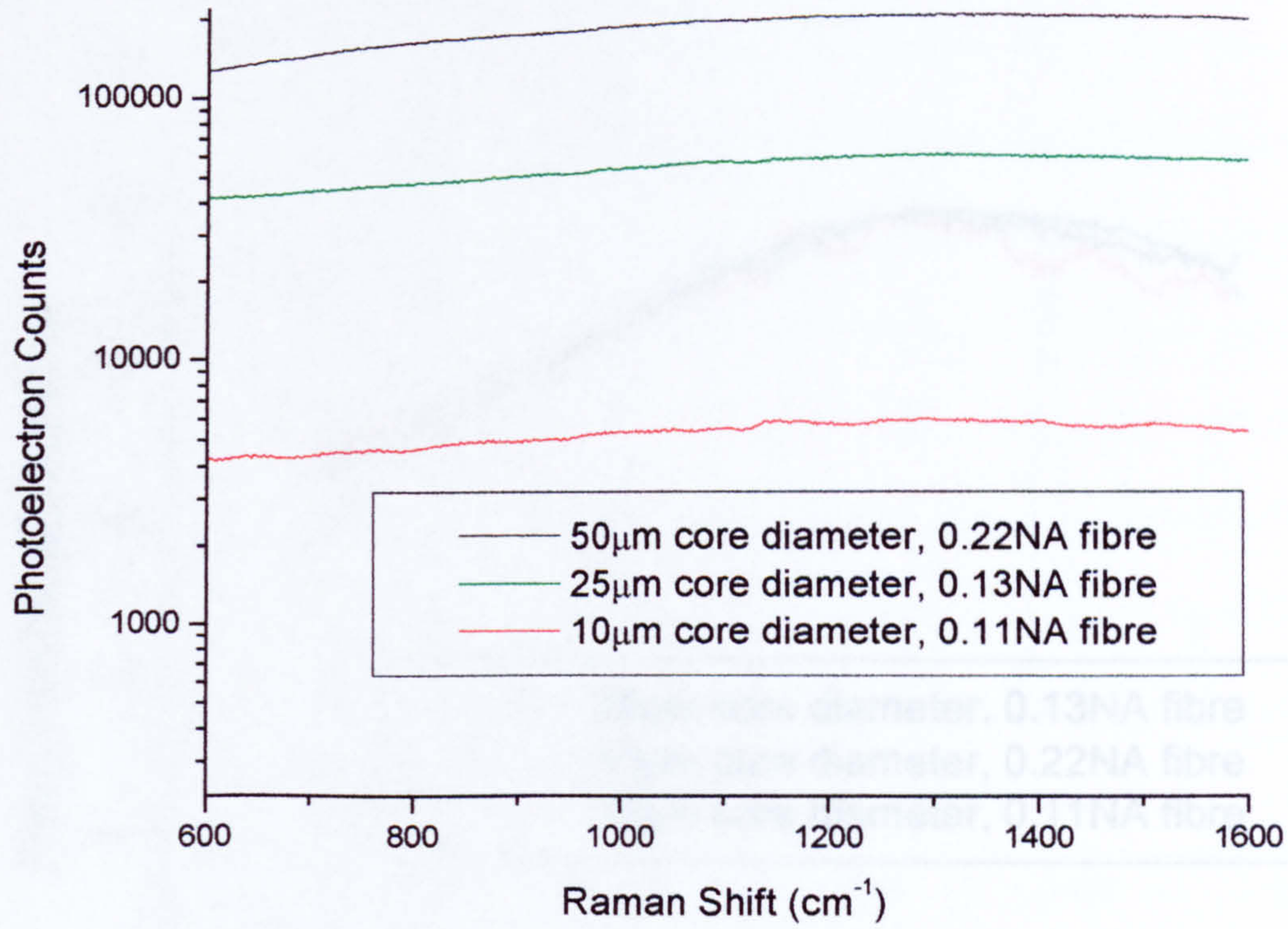

Figure 4.16 Uncorrected white light spectra recorded using the S^2R^5 spectrograph with three different optical fibres

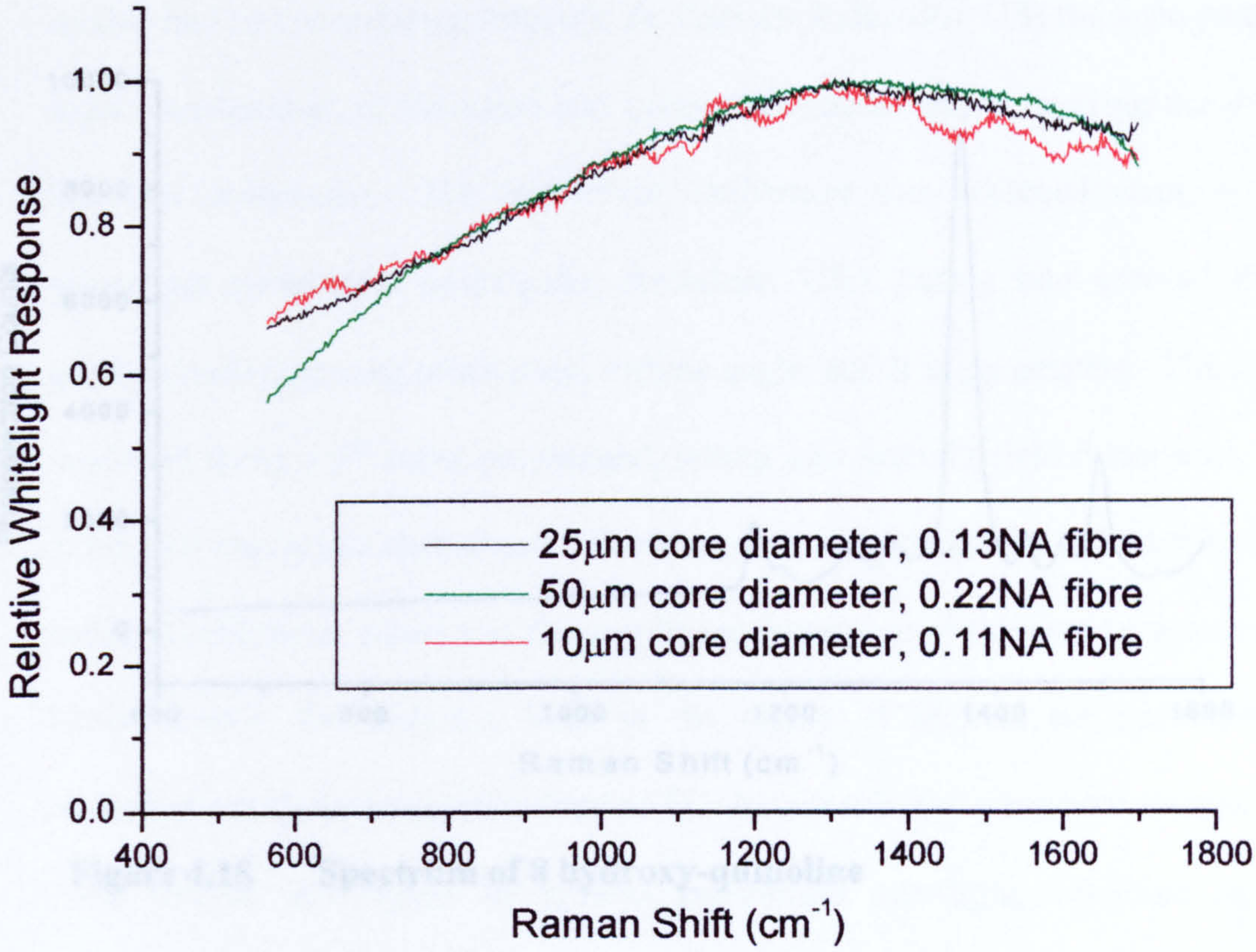

Figure 4.17 Uncorrected vignetting function of spectrograph using different optical fibres

From figure 4.17, the spectrograph vignetting function is slightly improved as the optical fibre numerical-aperture is reduced. This is caused by the waist of the dispersed Raman scattered flux overfilling the aperture of the CCD focussing lens. Raytracing predicts that this is more noticeable for small Raman shifts due to the grating position.

An example of a response-corrected spectrum of the 8 hydroxy-quinoline is shown in figure 4.18.

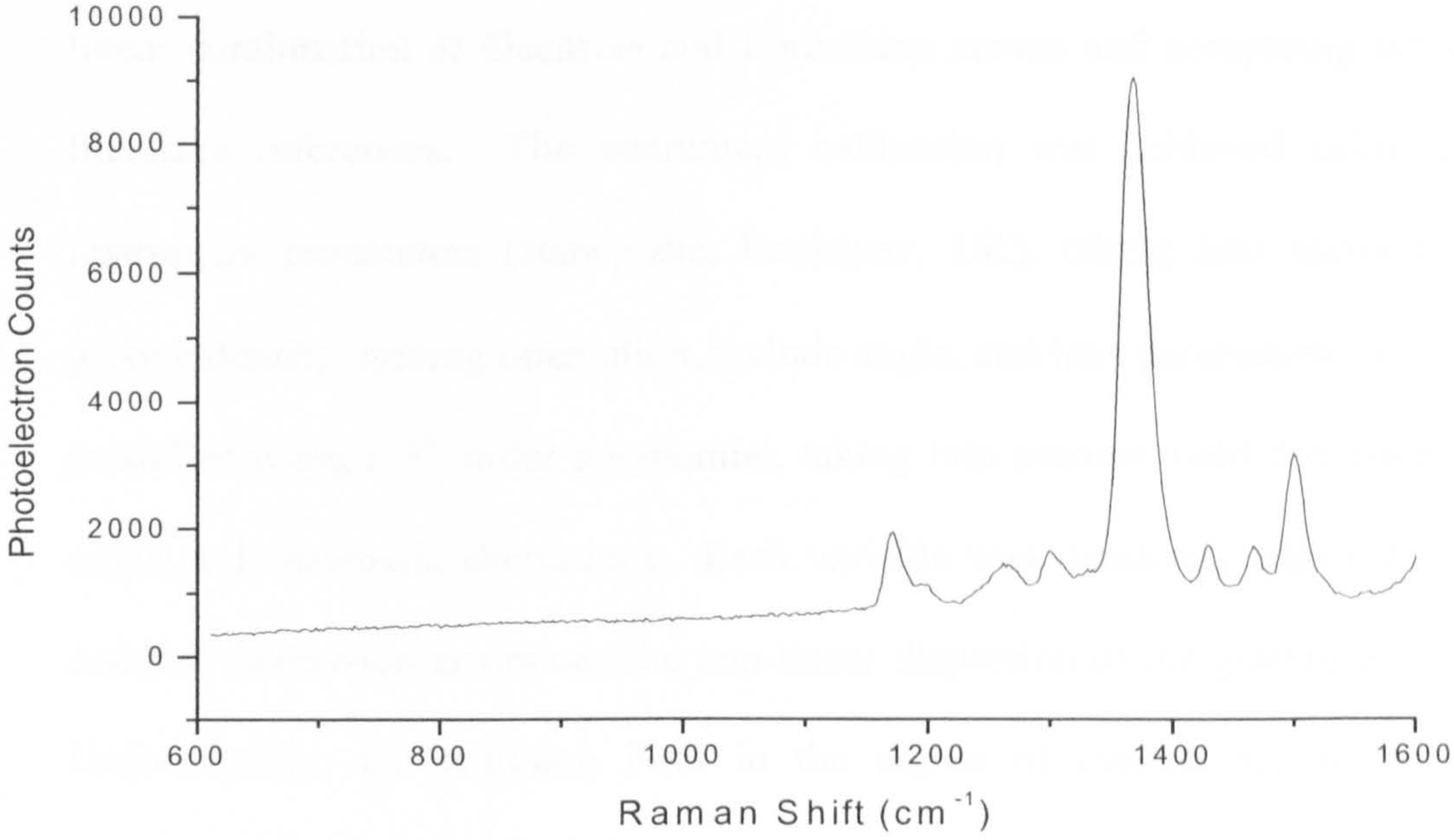

Figure 4.18 Spectrum of 8 hydroxy-quinoline

The spectral region of interest recorded by the spectrograph was deduced using equation 4.5. The pixel limited spectral bandwidth was calculated using equation 4.6.

$$\Delta\beta = \frac{\Delta\nu}{N_{pixel}} \qquad \textbf{4.6}$$

The pixel-limited spectral bandwidth was measured as 1.91cm^{-1}. Wavelength calibration was achieved by taking a spectrum of the discrete atomic emission lines from a low-pressure, Neon-discharge lamp (Renishaw, UK). The line positions were established by curve-fitting (curvefit.ab, Galactic Industries, US) the neon peaks using a linear combination of Gaussian and Lorentzian curves and comparing the values with literature references. The instrument calibration was achieved using a model of instrument parameters (staticg.abc, Renishaw, UK), taking into account the grating groove density, grating orientation, include angle, and lens parameters. The lenses were modelled using a 5th order polynomial, taking into account field distortions, spherical, coma and chromatic aberrations. Each variable was iteratively adjusted such that the residual calibration errors and the non-linear dispersion of the grating were minimised. Unfortunately, the emission lines in the region of interest are particularly weak, necessitating a long integration time of 5s. As a result, the integrated intensity of Neon lines outside the region of interest contributes straylight, manifest as a raised background. A spectrum of the Neon lines from 535cm^{-1} to 1640cm^{-1} is shown in figure 4.19.

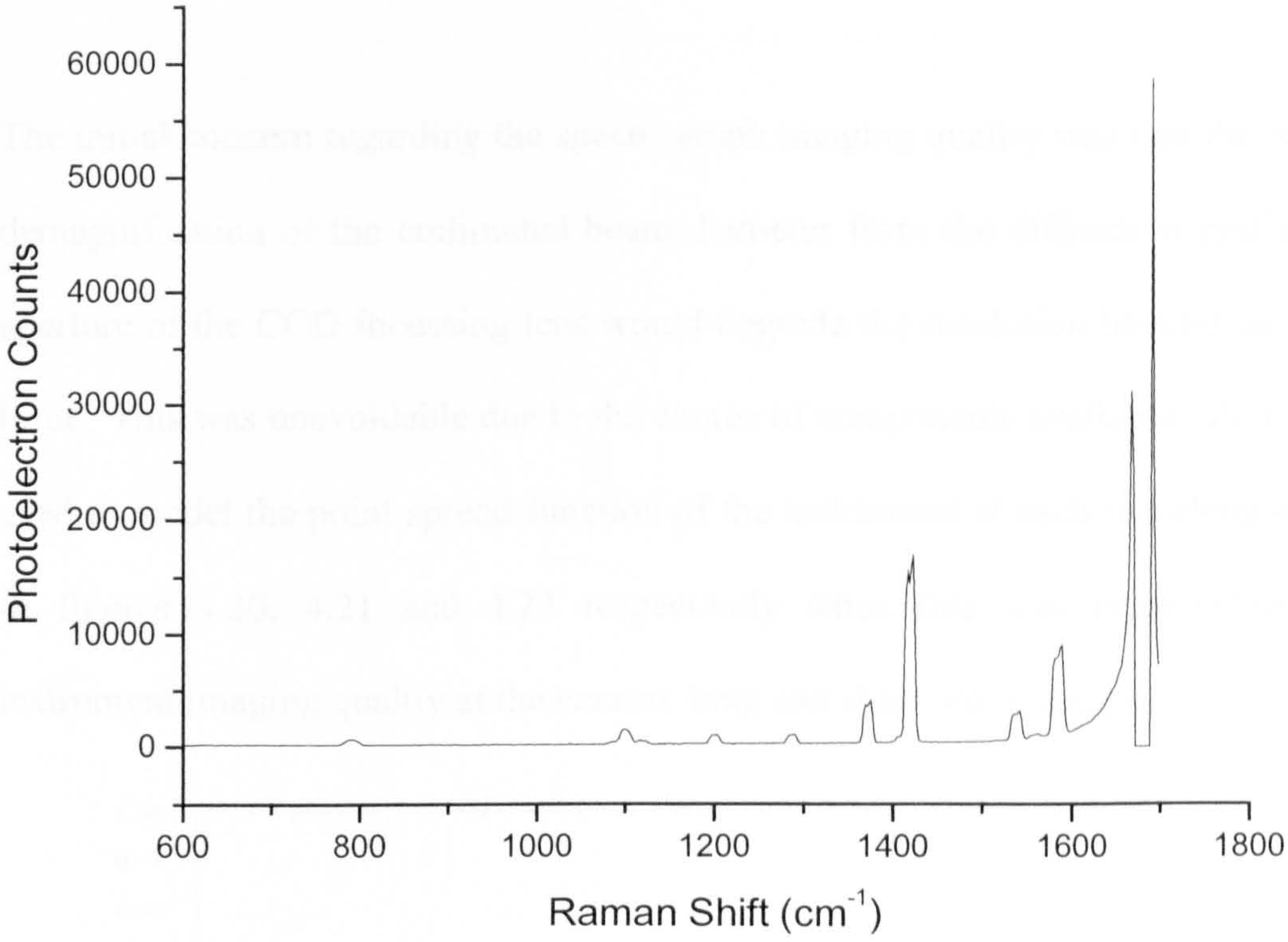

Figure 4.19 Neon Calibration Spectrum

The calibrated spectral region measured using the S^2R^5 spectrograph extends from 649.2cm^{-1} to 1764cm^{-1}. The calculated spectral region extends from 535cm^{-1} to 1640cm^{-1}; this difference is most likely due to mechanical misalignment of the grating. The experimentally-measured pixel limited resolution is 1.93cm^{-1}, in good agreement with the calculated value of 1.91cm^{-1}.

4.6.2 Imaging Quality

The initial concern regarding the spectrograph imaging quality was that the anamorphic demagnification of the collimated beam diameter from the diffraction grating into the aperture of the CCD focussing lens would degrade the resolution beyond an acceptable limit. This was unavoidable due to the choice of components available. Zemax 9.1 was used to model the point spread function of the instrument at each wavelength as shown in figures 4.20, 4.21 and 4.22 respectively since this was representative of the instrument imaging quality at the central, long and short wavelengths.

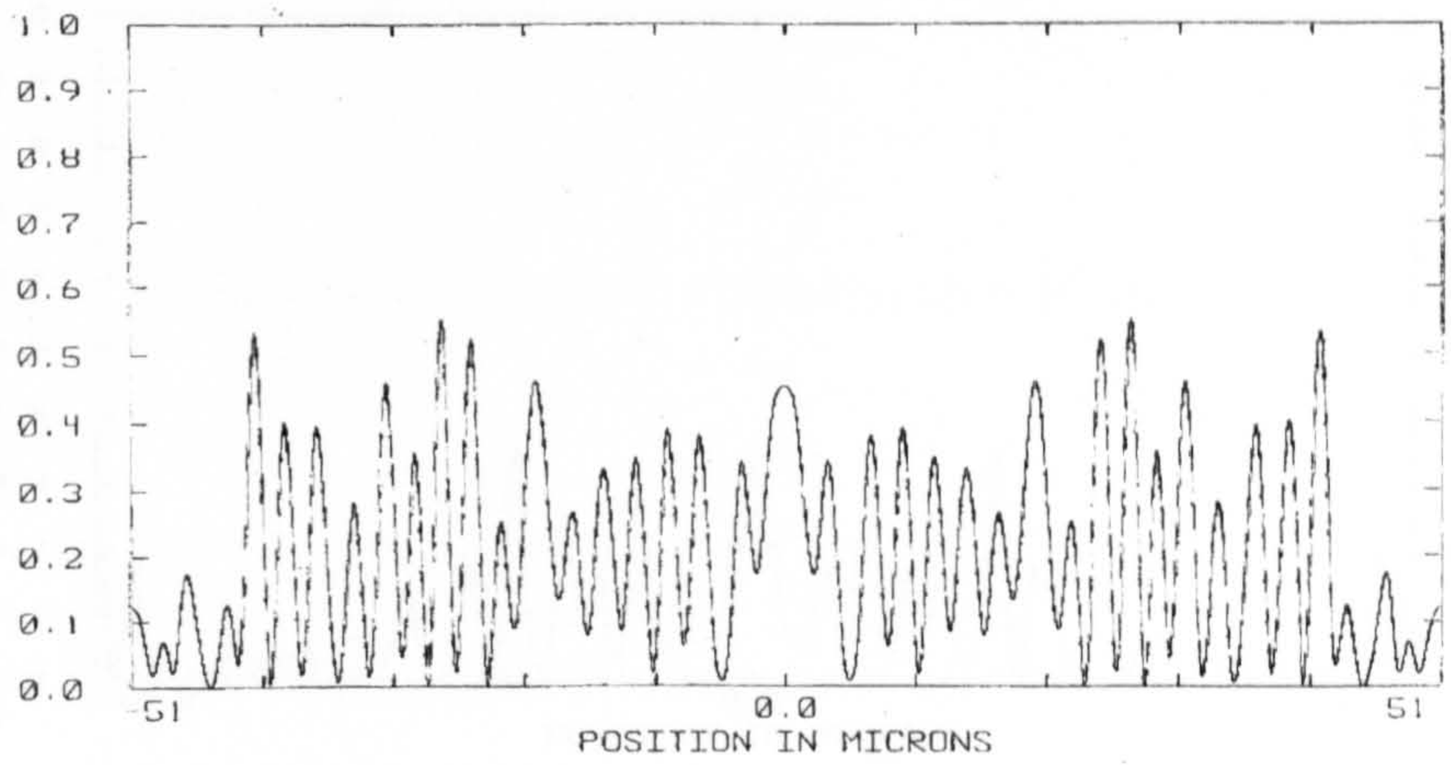

Figure 4.20 Point spread function at 548nm

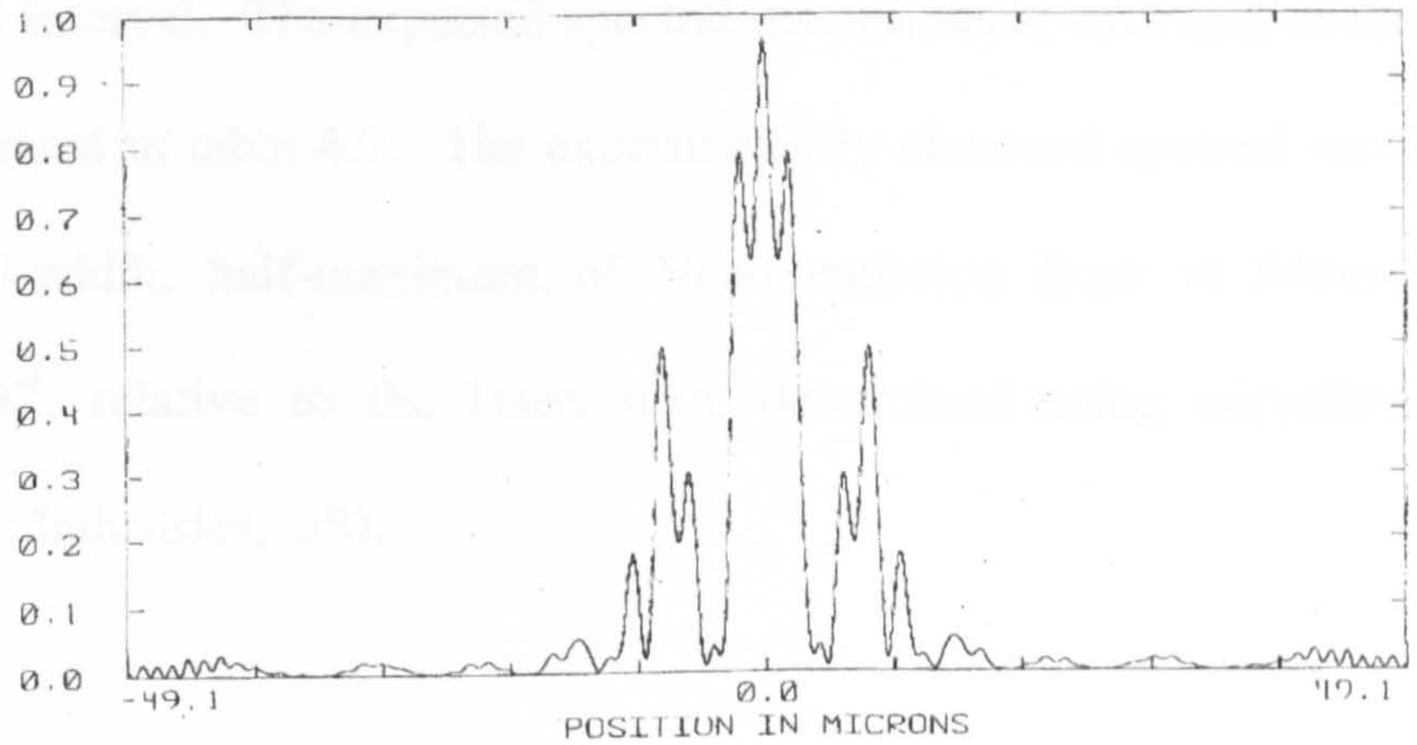

Figure 4.21 Point spread function at 567nm

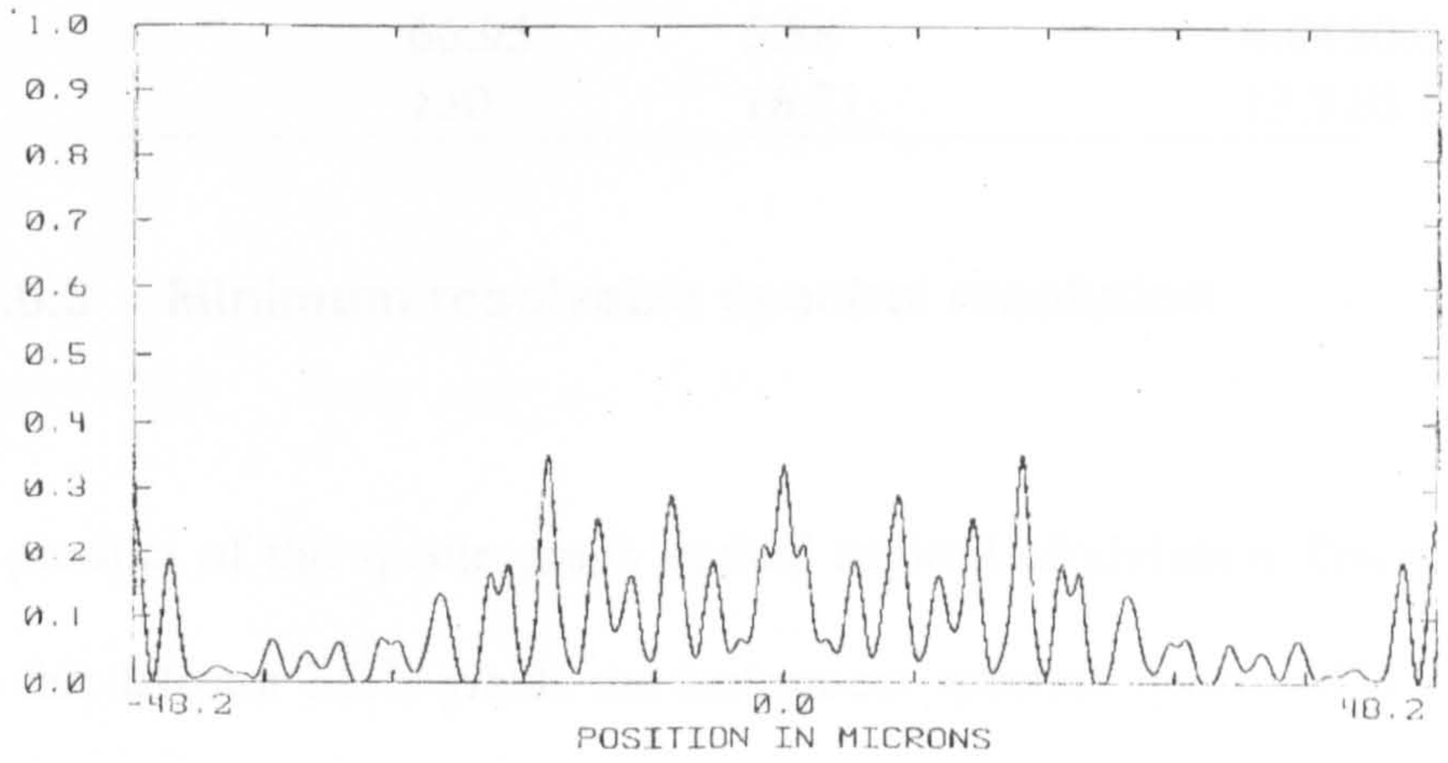

Figure 4.22 Point spread function at 597nm

From the width of the envelope of the point spread functions, it appears that the focal plane of the spectrograph is curved with respect to the plane of the detector surface, resulting in a loss of resolution towards the detector edges (when the lenses are focussed optimally at the detector centre). The spatial extent of the full width, half maximum at

each wavelength were measured from these graphs and converted into an equivalent spectral interval. The expected spectral resolutions at each end of the detector chip are summarised in table 4.7. The experimentally observed spectral resolutions, quoted as the full-width, half-maximum of Neon emission lines at 546cm^{-1}, 1200cm^{-1} and 1645cm^{-1}, relative to the laser, were determined using curvefitting. (curvefit.ab, Galactic Industries, US).

Table 4.7 Full width, half-maxima at characteristic points in the detector

Wavelength (nm)	FWHM (μm)	FWHM (cm^{-1})	Observed FWHM (cm^{-1})
548	105.5	13.16	13.5±0.12
567	66.95	5.88	6.04±0.09
584	130	16.21	13.8±0.16

4.6.3 Minimum resolvable spectral resolution

The product of the spectrograph optical sagittal Modulation Transfer Function (MTF) with the detector MTF yields the instrument spectral system MTF. This identifies the ability of the spectrograph to reproduce spatial frequencies.

The spatial frequency, u_{lim}, at which the system MTF is zero corresponds to the minimum resolvable resolution. The instrument is not capable of reproducing spatial frequencies greater than this point without aliasing.

In addition, the point at which the system MTF is 0.11, corresponds to the Rayleigh resolution limit. The MTF of the spectrograph optics is shown in figures 4.23, 4.24 and 4.25 respectively.

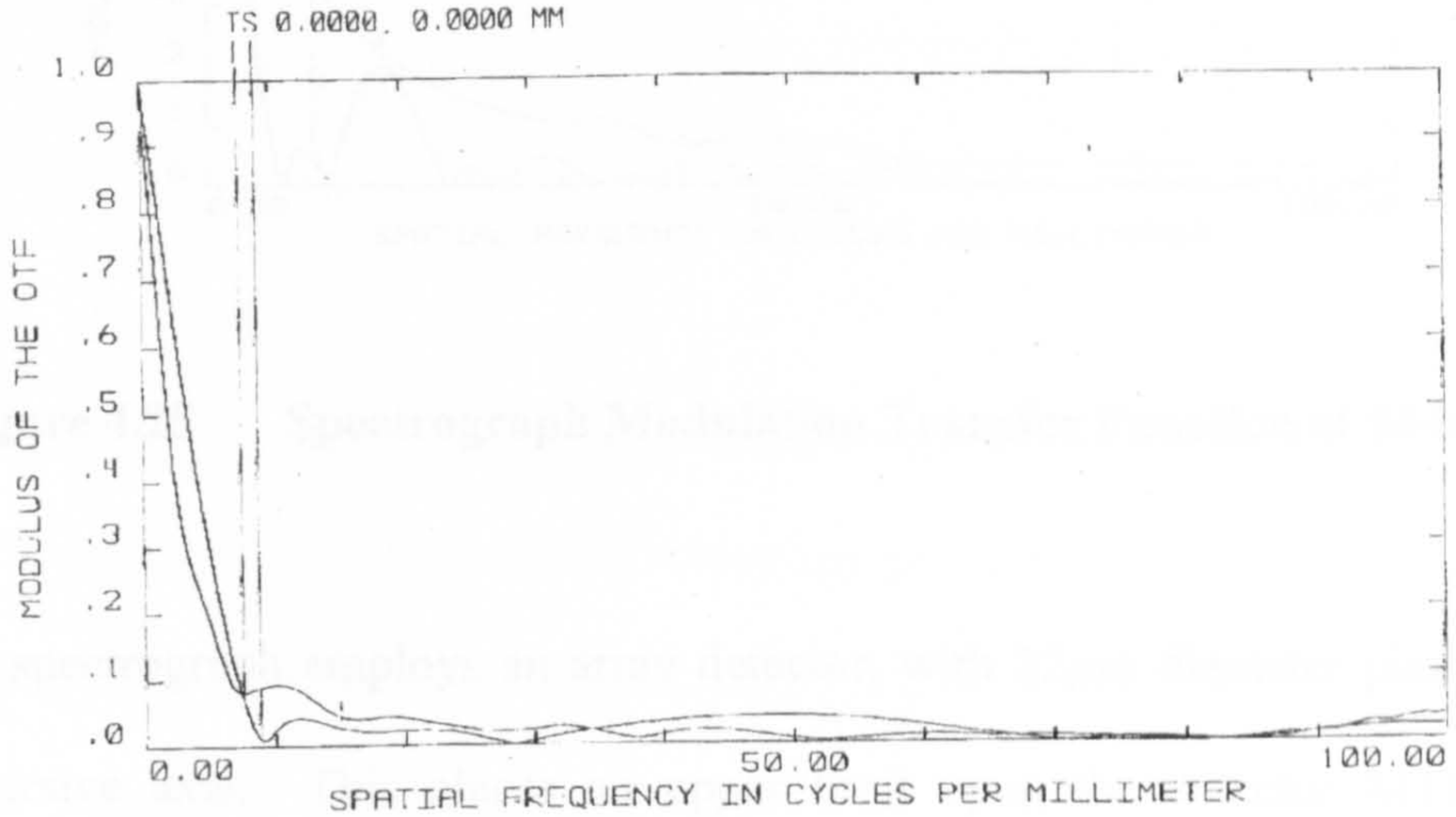

Figure 4.23 Spectrograph Modulation Transfer Function at 548nm

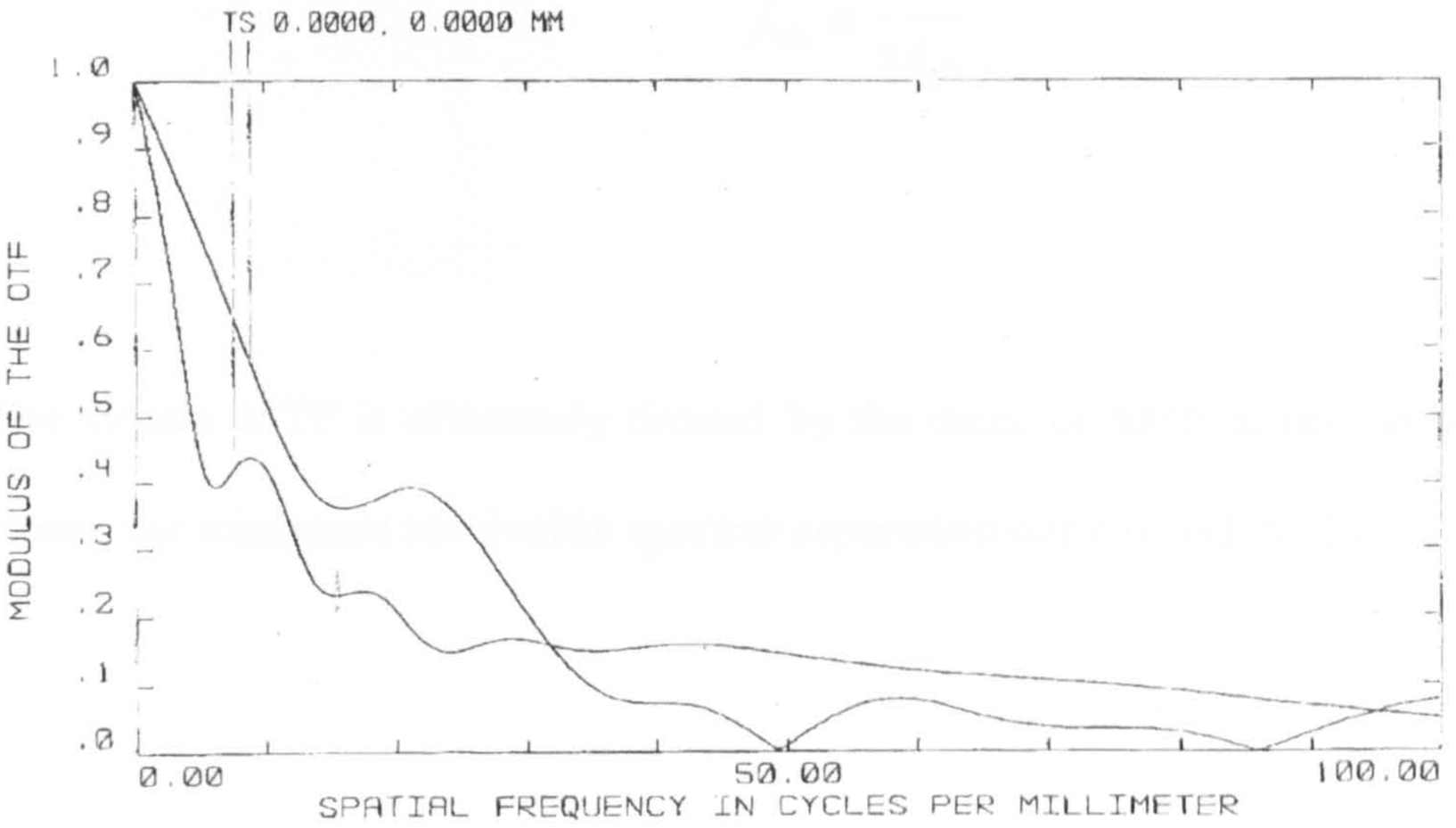

Figure 4.24 Spectrograph Modulation Transfer Function at 567nm

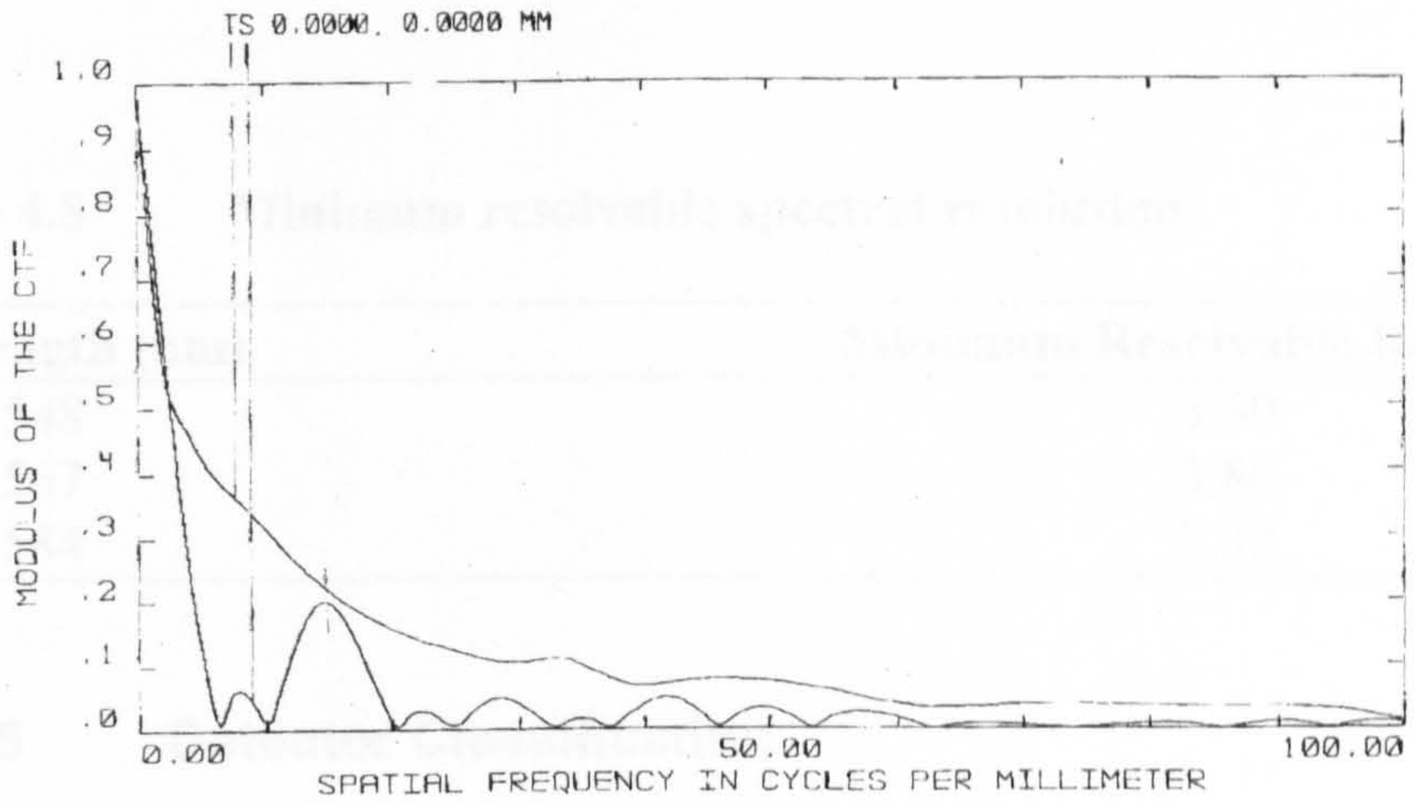

Figure 4.25 Spectrograph Modulation Transfer Function at 584nm

The spectrograph employs an array detector, with 22μm diameter pixels, d_{pixel}, in the dispersive axis. This places an upper limit upon the detector MTF according to equation 4.7.

$$f_{\lim} = \frac{1}{2d_{pixel}} \qquad \textbf{4.7}$$

The system MTF is ultimately limited by the detector MTF at the central wavelength. Hence the minimum resolvable spectral separation corresponds to $2d_{pixel}$.

Table 4.8 Minimum resolvable spectral resolution

Wavelength (nm)	Minimum Resolvable Resolution (cm^{-1})
548	5.50
567	3.86
584	2.32

4.6.5 Detector Classification

The determination of the CCD detector performance used in this concept demonstration was important. The four critical operating parameters relevant to the detector were; readnoise, N_{read}, signal-dependent noise sources, thermally generated noise, N_{dark}, and noise associated with straylight, N_{stray}. The effect of signal-dependent and chip-dependent noise is shown in figure 4.26.

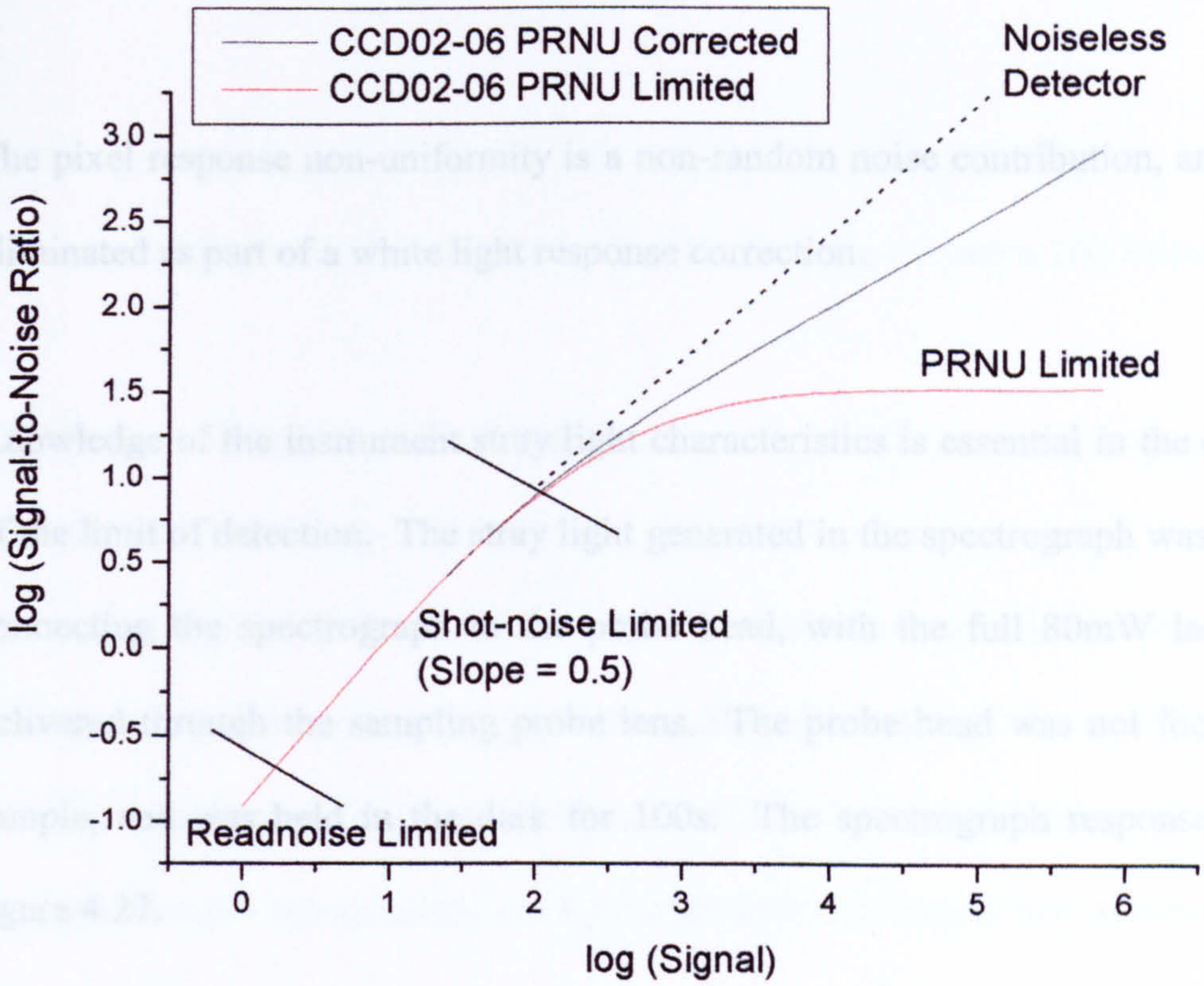

Figure 4.26 Log Signal-to-Noise Ratio vs Signal Plot

CCD Camera : G91766 AIMO
Parameters:
CTE: 0.999993
PRNU: 3% of mean (standard deviation)
Read Noise: 5.6e^-/p RMS
Dark Noise: 0.05e^-/p/s RMS

From figure 4.26, there are three regimes of operation corresponding to;

- Read noise dominated measurements at very low light levels
- Shot noise dominated measurements at moderate light levels
- Pixel response non-uniformity (PRNU) dominated noise at signal levels close to saturation.

The pixel response non-uniformity is a non-random noise contribution, and is typically eliminated as part of a white light response correction.

Knowledge of the instrument stray light characteristics is essential in the determination of the limit of detection. The stray light generated in the spectrograph was measured by connecting the spectrograph to the probe head, with the full 80mW laser excitation delivered through the sampling probe lens. The probe head was not focussed on any sample, and was held in the dark for 100s. The spectrograph response is shown in figure 4.27.

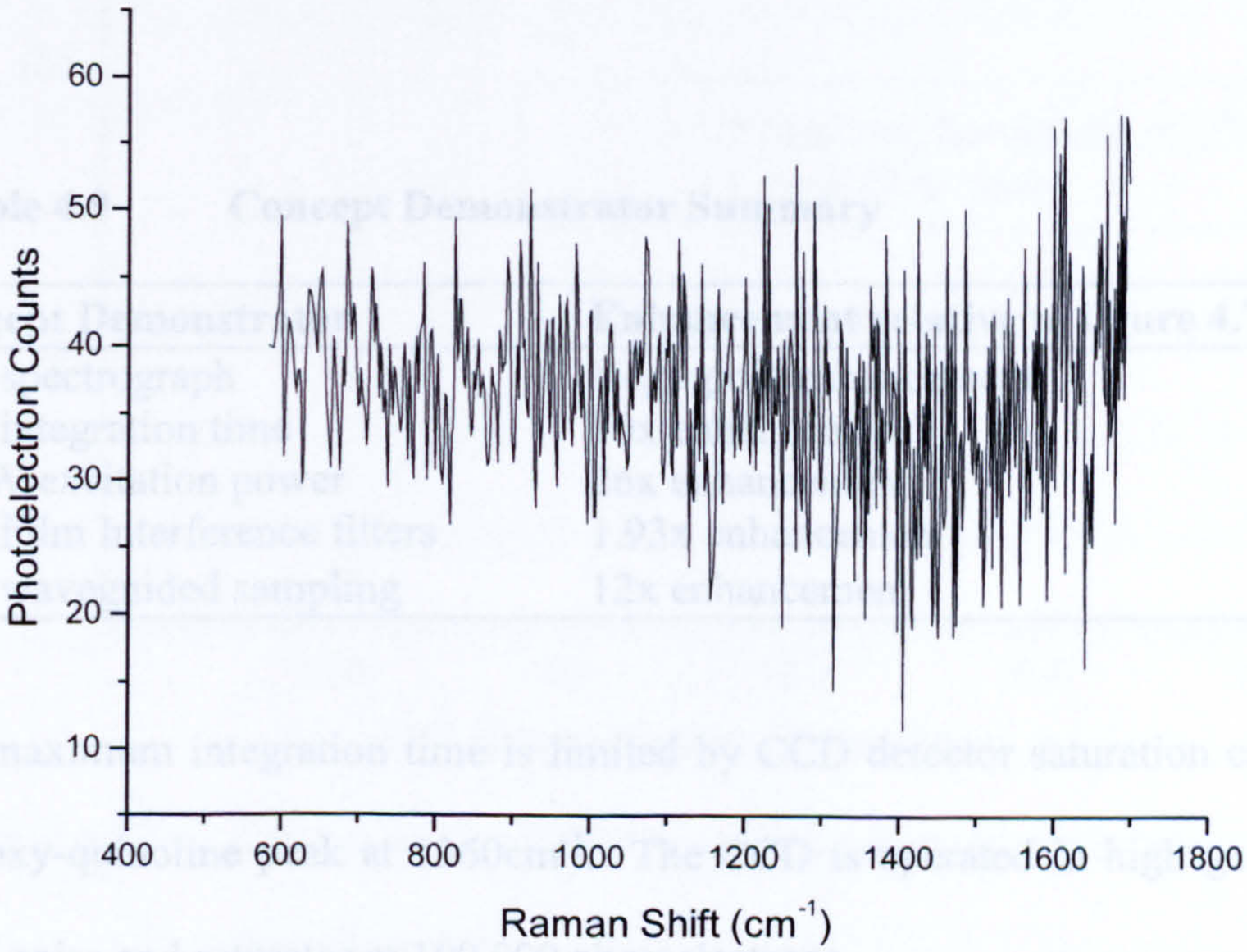

Figure 4.27 Stray light

Integration Time: 100s
Laser Power: 15mW at sample

This is consistent with that observed using the Renishaw System 100 Raman analyser.

4.6.6 Projected Performance

The projected performance of the concept demonstrator was estimated by modelling the increase in signal-to-noise ratio expected at each of the spectra shown in figure 4.7. The critical components of the concept demonstrator and the signal enhancement relative to the experimental set-up employed by Strathclyde University are summarised in table 4.9.

Table 4.9 Concept Demonstrator Summary

Concept Demonstrator	Enhancement relative to figure 4.7
S^2R^5 spectrograph	Negligible enhancement
300s integration time	30x enhancement
80mW excitation power	26x enhancement
Thin Film Interference filters	1.93x enhancement
180° waveguided sampling	12x enhancement

The maximum integration time is limited by CCD detector saturation caused by the 8 hydroxy-quinoline peak at 1360cm^{-1}. The CCD is operated in high gain to minimise ADC noise and saturates at 100,000 photoelectrons.

The signal increase afforded using the parameters in table 4.9 implies that 2045 spectra must be recorded, one every 0.15s and added in software. This incurs additional read

noise; the noise associated with shot noise and dark current is increased through software binning.

The projected signal-to-noise ratio of each spectrum expected using the concept demonstrator is shown in figure 4.28.

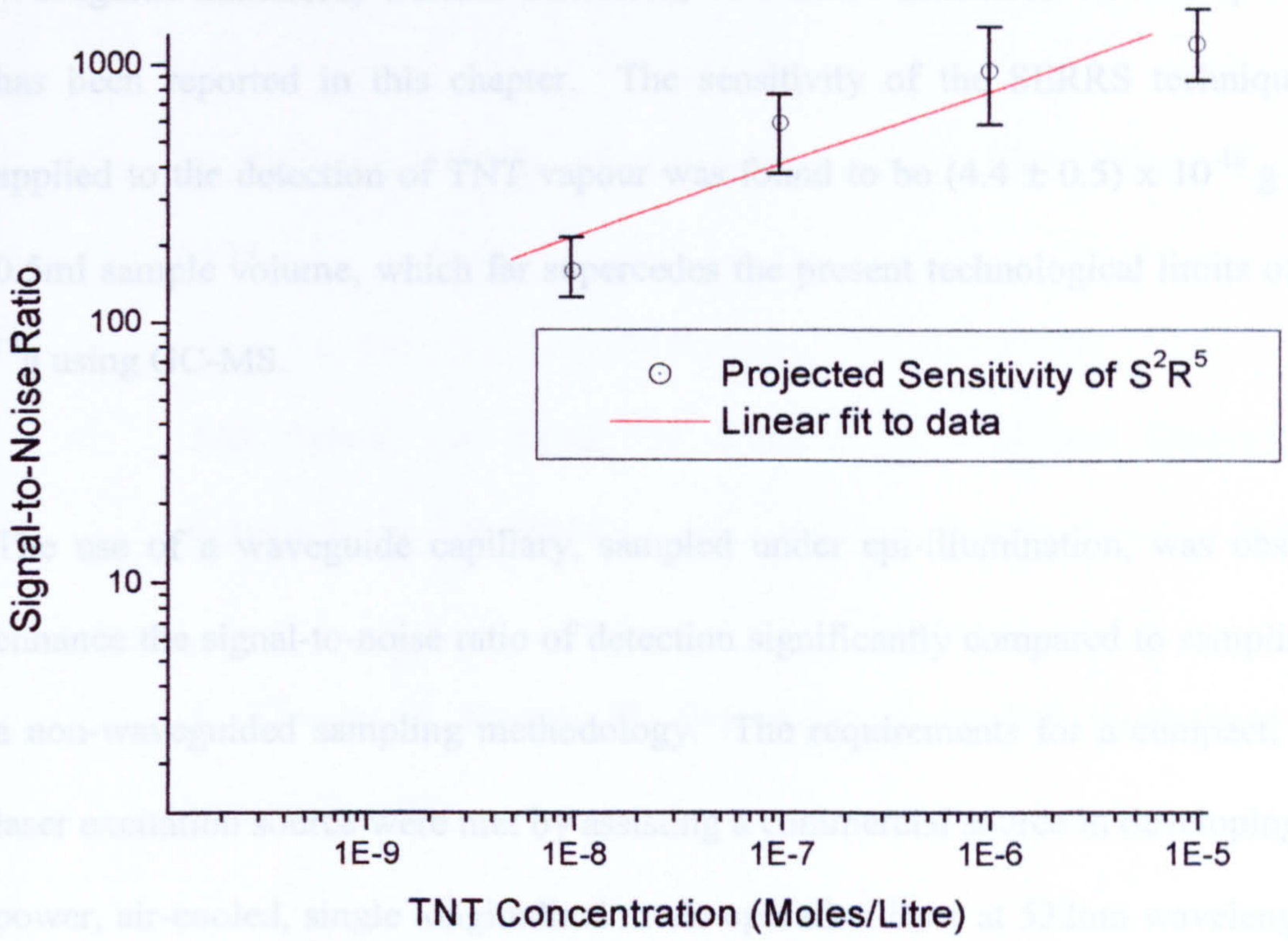

Figure 4.28 Concentration dependent signal-to-noise ratio's for concept demonstrator.

The limit of detection occurs at a TNT concentration of $(3.8 \pm 0.4) \times 10^{-15}$ moles/litre using a standard sample volume of 0.5ml injected into the SERRS flowcell. This

corresponds to an equivalent TNT mass of (4.4 ± 0.5) x 10^{-16} g within the injected sample volume.

4.7 Conclusions

The development of an instrument to yield sensitive detection of TNT vapour using Waveguide-Enhanced, Surface-Enhanced, Resonance-Enhanced Raman spectroscopy has been reported in this chapter. The sensitivity of the SERRS technique, when applied to the detection of TNT vapour was found to be (4.4 ± 0.5) x 10^{-16} g within a 0.5ml sample volume, which far supercedes the present technological limits of 1 x 10^{-12}g using GC-MS.

The use of a waveguide capillary, sampled under epi-illumination, was observed to enhance the signal-to-noise ratio of detection significantly compared to sampling using a non-waveguided sampling methodology. The requirements for a compact, portable laser excitation source were met by assisting a commercial source in developing a high-power, air-cooled, single longitudinal mode operation laser at 532nm wavelength. The instrument flexibility was enhanced by designing a band-pass filter to attenuate Raman scattering from a remote optical fibre to deliver excitation to the sample. The design of an imaging spectrograph, employing a surface-relief diffraction grating, has been achieved and observed to have a performance comparable with that predicted from geometrical optics.

4.8 References

1. J. Yinon, *Forensic and Environmental Detection of Explosives.* John Wiley and Sons, Ltd, London, UK, 1999.

2. B. Dionne & C. Rounbehler, Journal of Energetic Materials, 1986, Volume 4, pp 447-472.

3. K. Kneipp & Y. Wang, Spectrochemica Acta A, 1995, Volume 51, pp 2171-2175.

4. J.M. Sylvia, J.A. Janni, J.D. Klein et al, Analytical Chemistry, 2000, Volume 72, pp 5834-5840.

5. K. Kneipp, H. Kneipp, G. Deinum et al, Applied Spectroscopy, 1998, Volume 2, p 175.

6. D. Graham, W.E. Smith, C.J. McHugh, R. Kier, Chemical Communications, 2002, pp 580-581.

7. T. Donnelly, Strathclyde University Undergraduate Dissertation, 1998.

8. S. Cooper, Strathclyde University Postdoctoral Dissertation, 1998.

9. C. McLaughlin, Ph.D thesis, Strathclyde University, 2000, *Development and evaluation of surface-enhanced resonance Raman scattering (SERRS) spectroscopy for quantitative analysis.*

10. G.E. Walrafen & J. Stone, Applied Spectroscopy, 1972, Volume 26, p 585.

11. G.E. Walrafen, Physics B1, 1974, Volume 12, p 540.

12. G.E. Walrafen, Applied Spectroscopy, 1975, Volume 29, p 179

13. G.E. Walrafen, Applied Spectroscopy, 1977, Volume 31, p 295-299

14. R. Altkorn, I. Koev, M. Pelletier, Applied Spectroscopy, 1999, Volume 53, pp 1169-1176.

15. R. Altkorn, M. Malinsky, R. Van Duyne et al, Applied Spectroscopy, 2001, Volume 55, pp 373-381.

16. M. Pelletier & R. Altkorn, Analytical Chemistry, 2001, Volume 73, pp 1393-1397.

17. M. Pelletier & R. Altkorn, Applied Spectroscopy, 2000, Volume 54, pp 1837-1841.

18. A. Ruddick, D.N. Batchelder, K.D. Bartle et al, Applied Spectroscopy, 2000, Volume 54, pp 1857-1862.

19. S.M. Angel, T. Cooney, H.T. Skinner, Applied Spectroscopy, 1996, Volume 50, pp 836-860.

20. G. Turrell, 'Raman Sampling' in *Practical Raman Spectroscopy*,D.J. Gardiner & P.R. Graves, (Editors), Springer, New York, USA, 1989.

21. C.L Stevenson T. Vo-Dinh, *Signal Expressions in Raman Spectroscopy* in *Modern Techniques in Raman Spectroscopy,* J.J Laserna, (Editor), John Wiley & Sons, Chichester, UK, 1996.

Chapter 5

Stand-off Detection of SERRS Substrates

5.1 Introduction

The analysis of materials at long standoff distances is an area of interest for forensic investigations[1], requiring both rapid detection and identification of small objects using a portable instrument. This may be achieved using passive methods, whereby the intrinsic nature of the target object is studied, or actively, whereby a labelling material is applied to the target object and studied. The immediate necessity is for an instrument capable of general-purpose object tracking, and also, for the remote (standoff) detection of noxious or dangerous materials in the open air.

The purpose of this project, therefore, was to develop a portable, compact concept demonstrator instrument capable of detecting and identifying tagged objects at long standoff to enable the tracking of material, or equipment. Additionally, selectivity of detection between different labelling materials was important to enable multiple objects to be tracked. It was specified that the instrument should be capable of identifying a labelled object at a minimum standoff of 5m using a maximum excitation power of 5mW within a maximum measurement time of 20s. For portability, it was essential that the detector head be limited to an approximate maximum aperture diameter of 70mm. A wide range of technologies based on optical spectroscopy have been presented[2-6],

which could be applied to either passive detection or, by using an appropriate strongly scattering material, used in an active tagging role. A brief résumé of these techniques was performed to identify the advantages and constraints of these methods.

Fluorescence and UV-VIS absorption spectroscopy enable sensitive measurements, but the often-broad spectral features do not afford the chemical selectivity required for accurate sample discrimination. For this reason, these techniques cannot be considered. The development of an instrument for the use of UV-Raman spectroscopy has been reported for the categorisation of chemical spills at standoff distances approaching 550m.[2] The use of deep UV excitation makes use of the λ^{-4} dependence of the scattering cross section of Raman scattering affording two orders of magnitude increase in signal over near infra-red Raman, and in addition has been shown to give resonance enhancement for some explosive materials[7]. The intrinsic vibrational nature of the sample material is studied, rather than labelling compounds, and can be compared with standard spectral libraries produced using laboratory-based Raman spectrometers. UV excitation below 300nm would also enable Raman spectra to be analysed under daylight conditions with minimal ambient background, due to the Hartley absorption region of atmospheric ozone. Non-resonance Raman spectroscopy of materials at long standoff distances during daylight is not feasible using visible excitation. Sample fluorescence induced by the laser excitation and a large ambient background from sunlight, artificial lighting and thermal radiation, obscures an intrinsically weak Raman spectrum. The instrument described in the above reference, however, requires high energy, invisible,

pulsed excitation from a cooled laser over a period of 60-150s for a standoff distance of 550m; this presents an unacceptable laser hazard for use in public areas. Collection of Raman scattered light was achieved using a 40cm diameter, Cassegrain telescope from a 70cm^2 sample area and analysed using a UV-optimised spectrometer. The requirement to house this equipment in a dedicated vehicle makes this technology expensive and also limits the instruments fieldable applications.

The extremely large scattering cross-section of Surface Enhanced Resonance Raman-active (SERRS) substrates makes them ideal as labelling materials. The signal enhancement over conventional Raman spectroscopy typically approaches 10^6-10^{12}, whilst retaining the chemically specific spectral features essential for accurate sample discrimination.

The aim of this study was to investigate the feasibility of long standoff detection of a proprietary SERRS substrate (Strathclyde University, Pure and Applied Chemistry Department.) using low-power excitation, short integration periods and the compact spectrometer unit described in chapter 4, and referred to as the S^2R^5 spectrometer. The original requirement was for two different instruments: a short-range, low-cost detector with a maximum range of 5m and a long-range detector. The expected characteristics of proposed designs were determined by conducting a preliminary study of the signal levels obtained using the SERRS substrates using a laboratory-based Raman

spectrometer and modelling the signal levels by accounting for a reduced collection numerical aperture, sampling conditions and the variation in system response functions.

5.2 Preliminary Study

5.2.1 Signal Level Considerations

The development of the 4(5'azobenzotriazole-3,5-dimethoxyphenylamine), (ABT DMOPA) SERRS substrate was performed at Strathclyde University[8], and is not the subject of this study. A sample of the ABT DMOPA substrate was supplied as a thin layer coating on a standard glass microscope slide. Preliminary spectra of the ABT DMOPA SERRS substrate were obtained using a Renishaw Raman System 100 spectrometer system. Excitation of 3.0mW, at 514nm (Spectra-Physics, GN514) was focussed onto a glass-slide mounted sample using a X5 infinity corrected microscope objective (Olympus, MSPLAN x5). Raman scattering was collected in 180° backscattering geometry. A spectrum of the substrate is shown in figure 5.1. The S^2R^5 spectrograph was designed for use with 532nm excitation since portable 514nm excitation sources are not commercially available. Since the absorption band of the sample[8] is broad, shifting to this excitation wavelength is expected to make negligible difference.

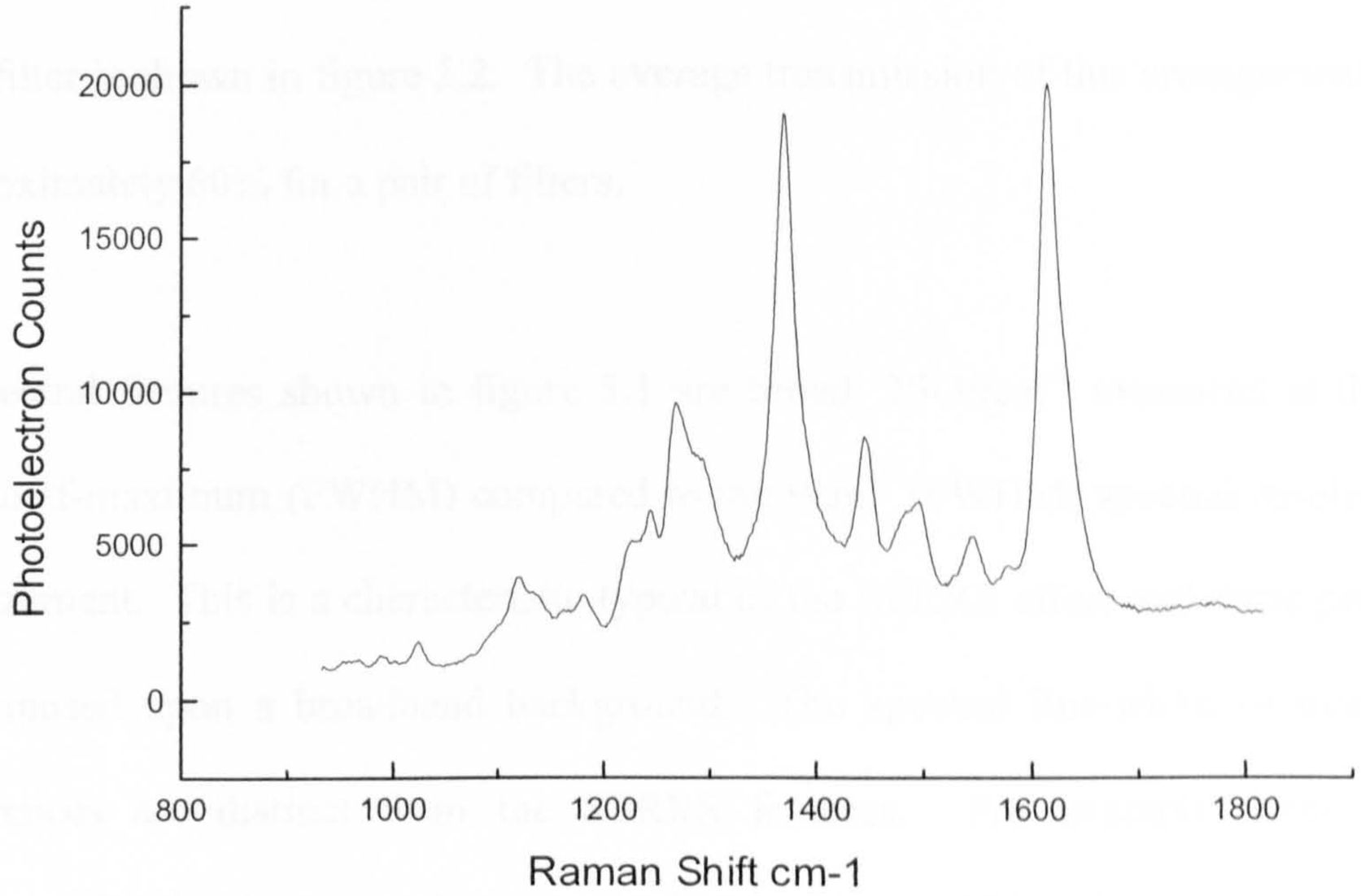

Figure 5.1 Reference Spectrum of GM19 SERRS Substrate

Source: Strathclyde University, Pure and Applied Chemistry Dept, McCabe, 2000

Experimental:

Excitation:	3.0mW at 514nm at Sample
Integration Time:	1sec
Collection Lens:	MSPLAN x5 (0.1NA)

The Renishaw System 100 has been described previously[9]. In this arrangement, the microscope objective lens limits the numerical aperture of collection, NA_{R100}, to 0.1. Rejection of elastically scattered light collected by the objective lens is achieved using a pair of holographic notch filters (Kaiser, 514nm). The transmission characteristic of a

single filter is shown in figure 5.2. The average transmission of this arrangement, τ_{R100}, is approximately 60% for a pair of filters.

The spectral features shown in figure 5.1 are broad, 25-30cm^{-1} measured at the full-width, half-maximum (FWHM) compared to the 9cm^{-1} (FWHM) spectral resolution of the instrument. This is a characteristic typical of the SERRS effect and these peaks are superimposed upon a broadband background. The spectral line-width of man-made interferences are distinct from the SERRS features. For example, low-pressure fluorescent lighting is due to discrete atomic transitions within a low pressure gas and are intrinsically narrow. Thermal sources only contribute to the broad background of the Raman spectrum.

The signals achievable using the S^2R^5 spectrometer and a 70mm diameter collection aperture can be estimated by considering the difference in system response function

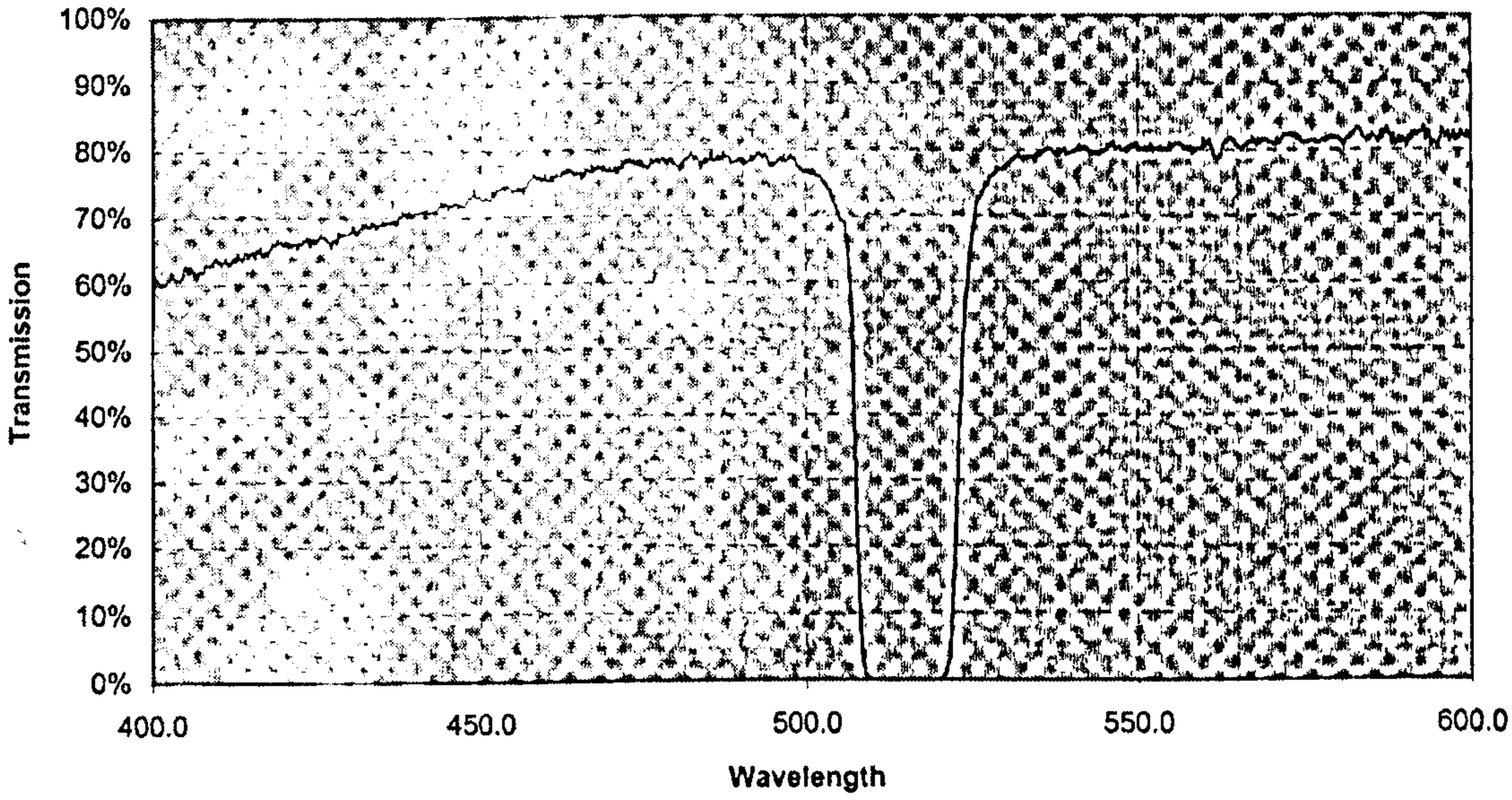

Figure 5.2 Transmission Function For a Single 514nm Holographic Notch Filter

Source (Kaiser Optical Systems, Inc)

between the Renishaw System 100 spectrometer and the field instrument. The major difference arrives from a reduction in the collection numerical aperture, NA, of the detector head, the transmission characteristics of the filters, τ, used to reject elastically scattered light, the integration time allowed, $t_{int,}$ and the laser power used at the sample, ϕ. In addition, the ratio of the spectral bandwidth of each binned pixel, $\Delta\beta$, the optical fibre area, A, used to collect the scattered light and the modulation transfer functions of the spectrographs, MTF, must be considered. A conversion factor, γ, can be considered as the product of the ratio's of each of these considerations and is shown in equation 5.1. The subscripts R100 and 5m refer to the preliminary and the 5m standoff experimental conditions respectively.

$$\gamma = \left(\frac{A_{R100}}{A_{5m}}\right)^2 \left(\frac{NA_{R100}}{NA_{5m}}\right)^2 \cdot \left(\frac{\phi_{R100}}{\phi_{5m}}\right) \cdot \left(\frac{\tau_{R100}}{\tau_{5m}}\right) \cdot \left(\frac{t_{\text{int}\,R100}}{t_{\text{int}\,5m}}\right) \left(\frac{\Delta\beta_{R100}}{\Delta\beta_{5m}}\right) \left(\frac{MTF_{SYSR100}}{MTF_{SYS5m}}\right) \quad \textbf{5.1}$$

The 5m standoff requirement makes it feasible to use a commercially available standard or telephoto camera lens to focus onto the sample, collect the inelastic scattered light and refocus it into the acceptance cone of an optical fibre positioned at the finite conjugate image position. The optical fibre is then used to remotely connect the detector optics to the spectrograph up to distances of 100m, according to the attenuation characteristics of the fibre. The detector head optics arrangement can be treated using the thin-lens approximation and is illustrated in figure 5.3.

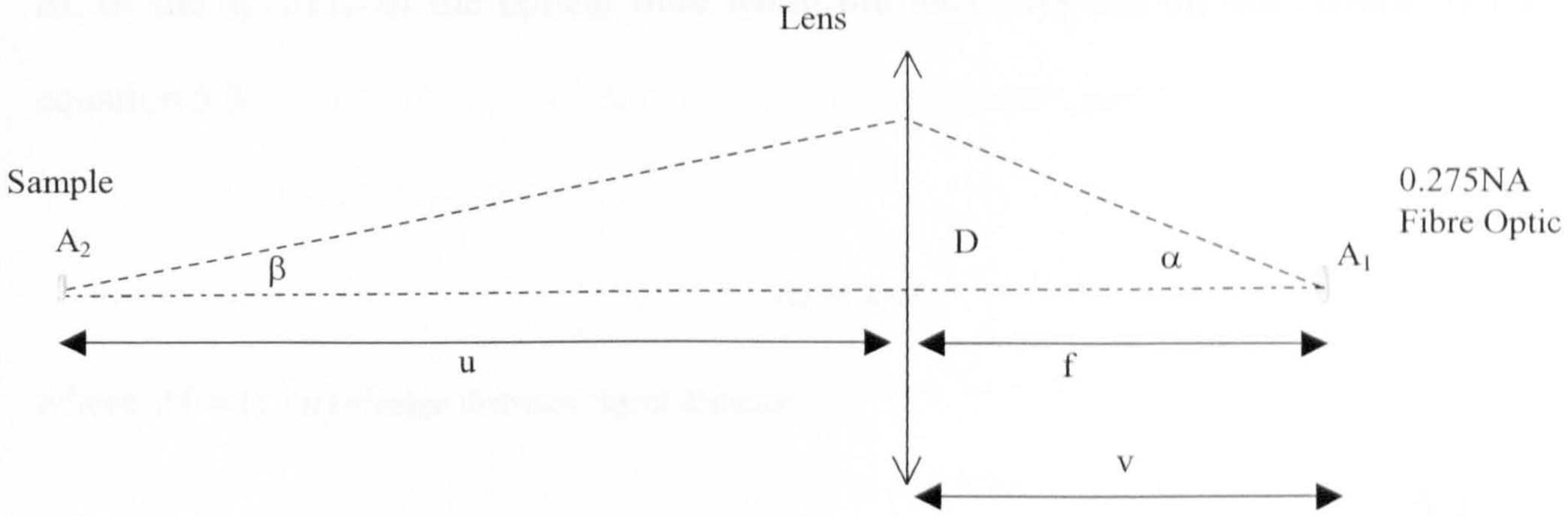

Figure 5.3 Schematic Representation of Detector Head for Collection of Raman Scattered Light

Where A_1 and A_2 refer to the areas of the optical fibre core and the sample area respectively. u and v refer to the object, image distances from the lens, defined by a focal length f. D denotes the radius of the effective collection aperture.

From the thin-lens approximation, the relationship between the focal length, f, the object distance, v, and the image distance, u is given in equation 5.2.

$$\frac{1}{f} = \frac{1}{v} + \frac{1}{u} \qquad \textbf{5.2}$$

The area of the sample interrogated by the detector will be defined by the magnification, M, of the aperture of the optical fibre using the lens. A_2 and A_1 are related by the equation 5.3.

$$A_2 = MA_1$$

where $M = (v/u)$=image distance/object distance

5.3

Ultimately, the numerical aperture of the CCD focussing lens used in the spectrograph limits the instrument collection aperture. This was limited by commercial reasons to f/1.4 in the S100 and S^2R^5 spectrographs. The aperture of this lens places a restriction of the maximum numerical aperture of the optical fibre connecting the spectrograph to the detector. The collection optical fibre used in this experiment has a numerical aperture of 0.275 and a core diameter of 62.5 μm. This does not overfill the aperture of the fibre-collimating lens, and enables most of the light diffracted by the grating to be gathered by the CCD focussing lens. The spectral range is imaged with minor vignetting* towards the edges of the detector. The spectral resolution of the system is closely related to the optical fibre core diameter.

The optical-fibre numerical aperture cannot be varied continuously, and is only available at discrete values influenced by the telecommunications market. Optical

---

* See figure 4.24

fibres are available with core diameters of 50 microns and an NA of 0.49, affording greater light collection and comparable spectral resolution, but the vignetting function of the spectrograph deteriorates as the CCD focussing lens aperture ceases to gather all the light dispersed by the grating.

The numerical aperture of the collection optic where the optical fibre numerical aperture, NA_{fibre}, is less than the collection lens may be determined using equation 5.4.

$$NA_{5m} = \frac{\nu \cdot (NA_{fibre})}{5000} \qquad 5.4$$

where ν is in mm

High-speed CCTV lenses are commercially available with sufficient imaging quality at low cost to be used as a collection optic. The largest aperture, commercially available, lens was found to be a 75mm f/1.4 lens (Pentax, Cosmicar C75014). The numerical aperture of the optical fibre limits the collection aperture diameter to 40.25mm. CCTV lenses are not an ideal for this application since their low cost comes at the expense of imaging quality. They are typically designed for imaging using detector pixel-limited

resolution, and so have a point spread function of approximately 30μm. The optical transfer function of the CCTV lens is shown in figure 5.4.

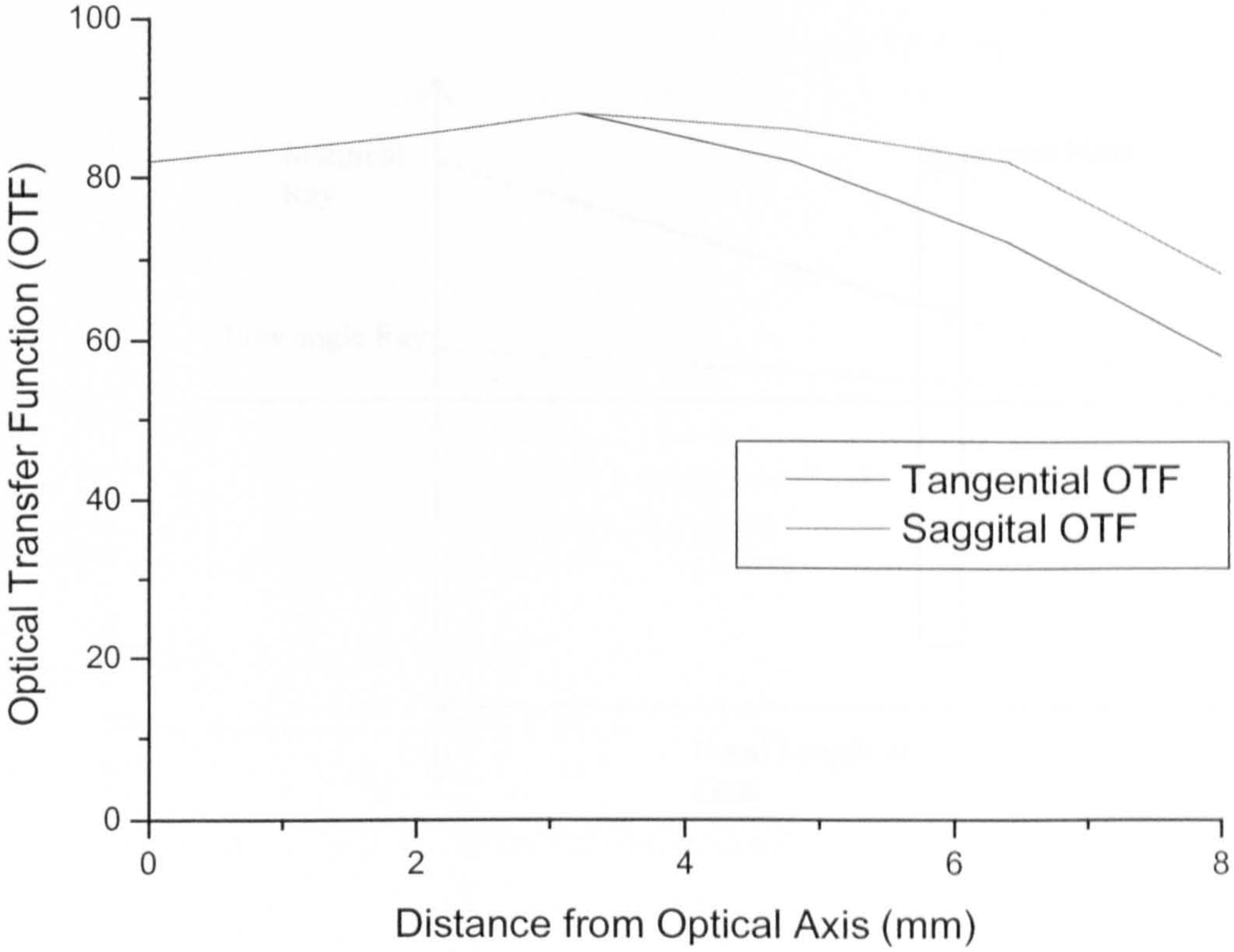

Figure 5.4 Optical Transfer Function of Pentax 75mm, f1.4 CCTV Lens

The rejection of the elastically scattered light was achieved using a proprietary dielectric thin film long-pass filter (Barr Associates, 532LPF), with a high transmissivity. For the purpose of feasibility demonstration, the collection optic was used to focus inelastic scattered light through the filter onto the optical fibre. This enables the full aperture of the collected light to be spectrally filtered using a small filter. This also introduces

spherical aberration into the imaging system, as illustrated in figure 5.5. The focal length of the lens, combined with the long-pass filter, is effectively increased for rays emerging from the lens furthest off axis and reduces the collection efficiency.

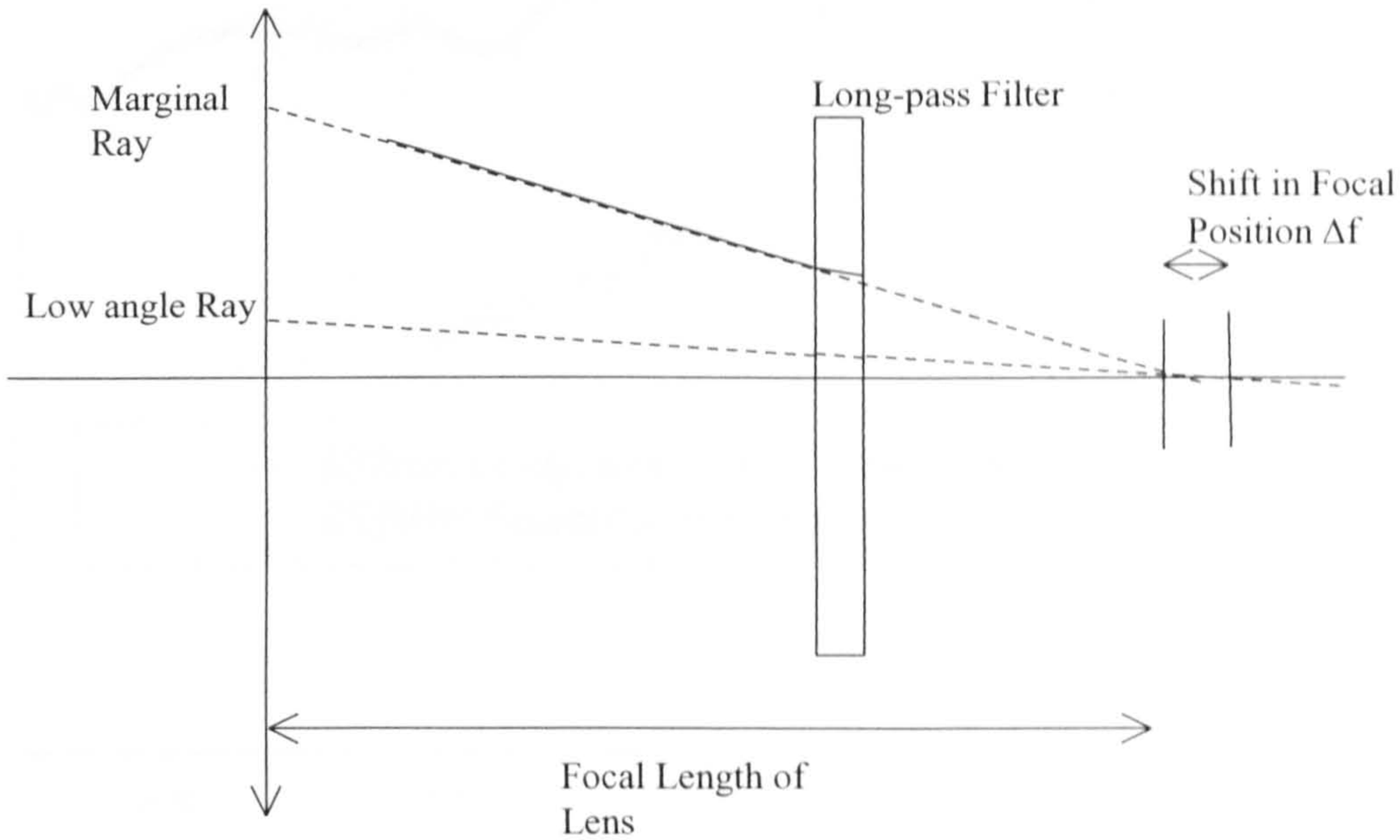

Figure 5.5 Spherical Aberration Introduced by Long-pass Filter

The spectral characteristics of the long-pass filter are polarisation and angle-dependent, but have been measured experimentally. These are shown in figure 5.6 for the most extreme angles of incidence, defined by the optical fibre numerical aperture. The transmissivity in the spectral region of interest to SERRS approaches 98% whilst

maintaining optical density blocking of at least 4.0 at 200cm^{-1} from the excitation wavelength.

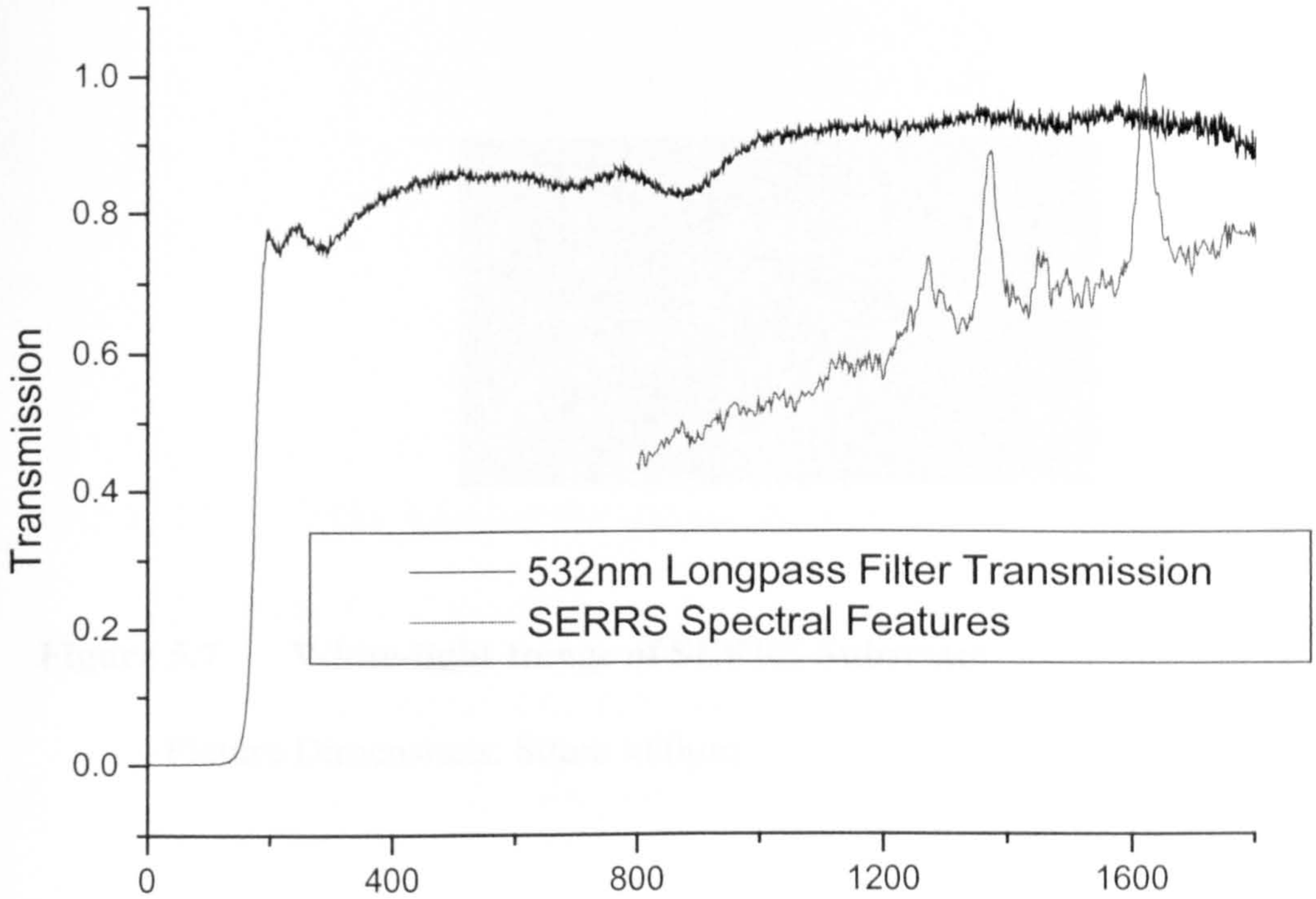

Figure 5.6 Transmission Characteristics of 532nm Longpass Filter

(Spectrum of GM19 Dye Superimposed)

5.2.2 Sample uniformity

The uniformity of signal intensity across the surface of the slide was measured using a System 1000 Raman microscope in conjunction with an encoded-reference XYZ

mapping stage. Excitation of 2mW at 488nm wavelength was focussed to a 1μm diameter spot using a 0.8NA, aplanatic microscope objective (Leica). A white-light image of the sample surface is shown in figure 5.7.

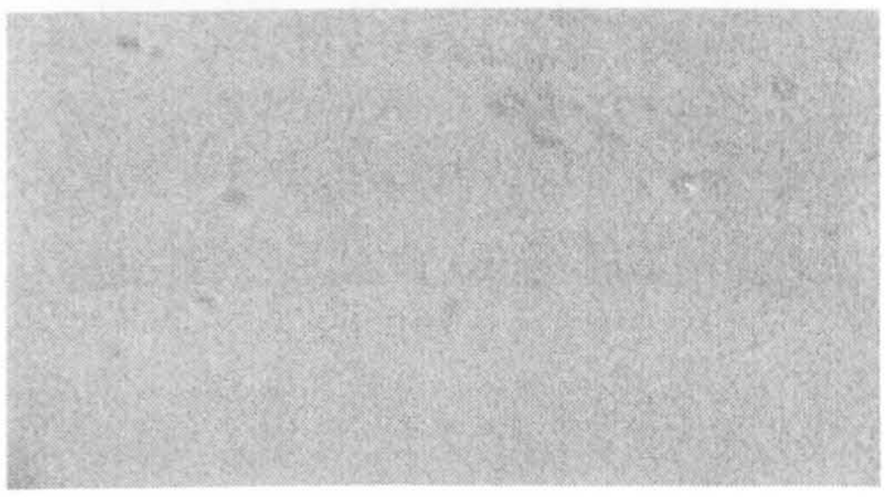

Figure 5.7 White-light Image of SERRS Substrate

Picture Dimensions: 80μm x60μm

The sample was translated at 1μm intervals across an $80x60\mu m^2$ area and spectra obtained over the spectral region 700-1700cm^{-1}. The background-subtracted area under the peak at 1630cm^{-1} was calculated in each point and used to generate the pixel intensity at each point in a false-colour image. This is shown in figure 5.8

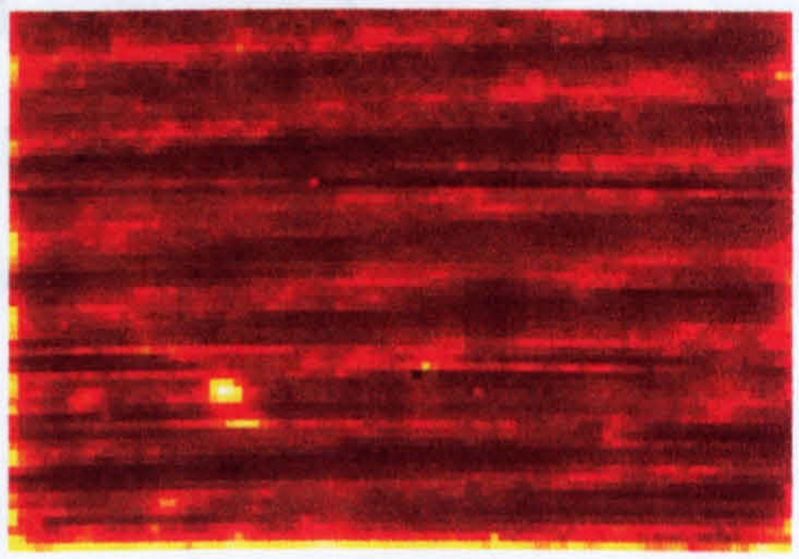

Figure 5.8 Raman Generated Image of the Sample Surface

Experimental Conditions

Integration Time: 0.1s per point

Signal intensity increases from black to yellow

The Raman image of the sample appears highly striated, with two regions of highly scattering material. A possible explanation for this lies in the preparation method, in which the sample is spread across the microscope slide substrate with a spatula. The presence of the bright points may simply arise from sample inhomogeneity. The standard deviation of the signal was found to be 7.4% of the signal average. The presence of the highly scattering centre in figure 5.8 suggests that the sample uniformity could still be improved.

5.3 Signal to Noise and Expected Performance

The limit of detection defines the point at which the weakest spectrum is discriminated from a noisy background. This is characterised by a signal-to-noise ratio of 3:1, although successful detection may be achieved below this using an appropriate algorithm[10].

The effective scaling factor, γ, used to account for the reduction in collected signal using equation 5.1 was calculated to be 50.7 using the collection parameters described in the caption for figure 5.9.

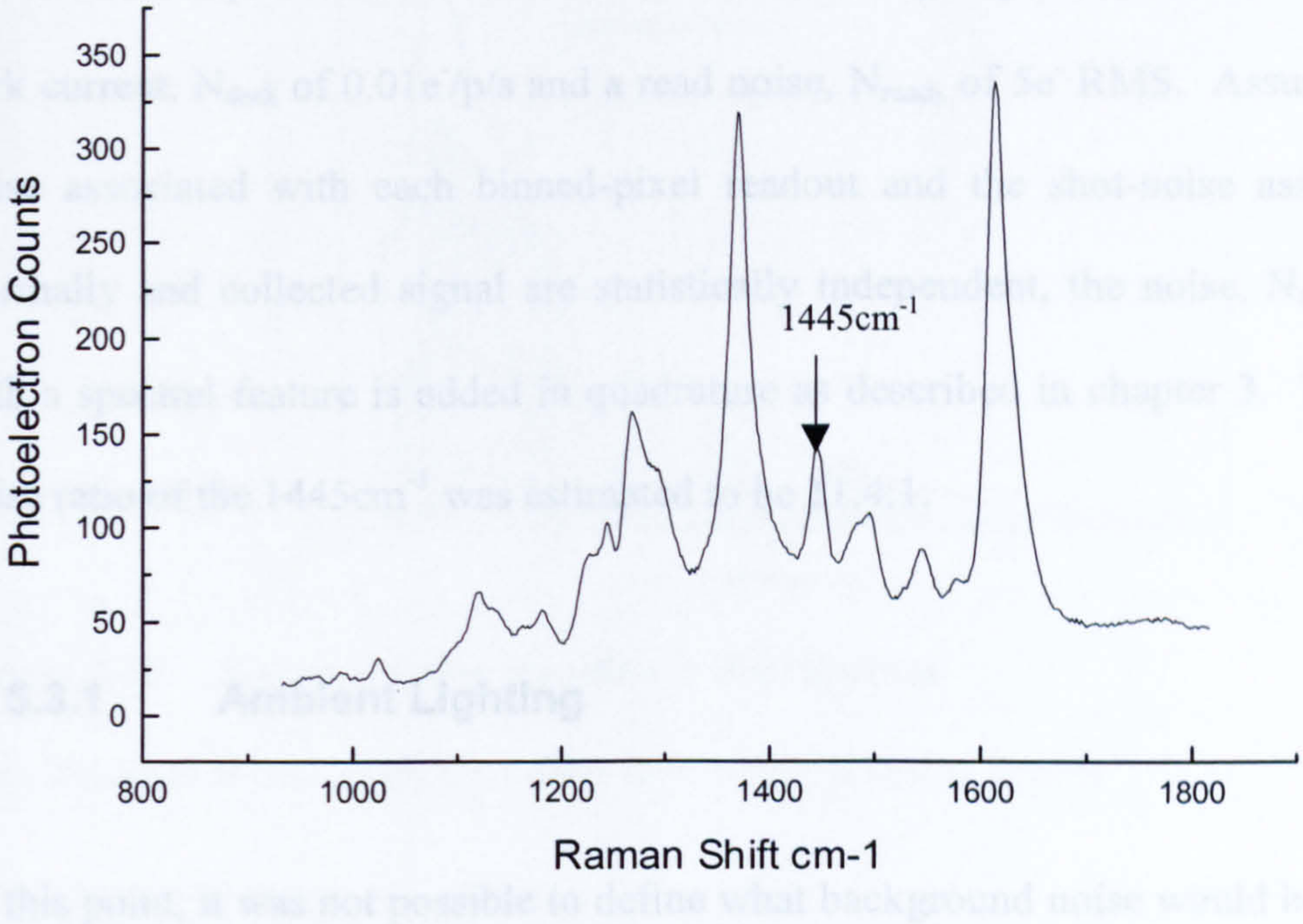

Figure 5.9 Expected Signal Levels for 5-Meter Stand-Off

Experimental Conditions

Excitation: 5.0mW at 532nm

Standoff Distance: 5m

Integration Time: 1sec

Collection Optic: 75mm f/1.4 Lens

Optical Fibre: 0.275NA

For the purpose of this study, it was decided that signal-to-noise calculations would be calculated using the feature at 1445cm^{-1} as this has the narrowest bandwidth of the

weaker spectral features. The signal may be increased by matching the bandwidth of the spectral features to the spectral interval of the pixels. The charge-coupled device used in this experiment was the EEV-CCD0206 chip, operated at -70°C, affording a dark current, N_{dark} of 0.01e^-/p/s and a read noise, N_{read}, of 5e^- RMS. Assuming that the noise associated with each binned-pixel readout and the shot-noise associated with thermally and collected signal are statistically independent, the noise, N_{tot}, associated with a spectral feature is added in quadrature as described in chapter 3. The signal to noise ratio of the 1445cm^{-1} was estimated to be 11.4:1.

5.3.1 Ambient Lighting

At this point, it was not possible to define what background noise would be present due to ambient natural and man-made lighting. The effect of an ambient background, B_A, adds linearly to the inelastic background, B_I.

The instrument capabilities under day conditions were modelled for taking into account the solar irradience distribution[11] shown in figure 5.10.

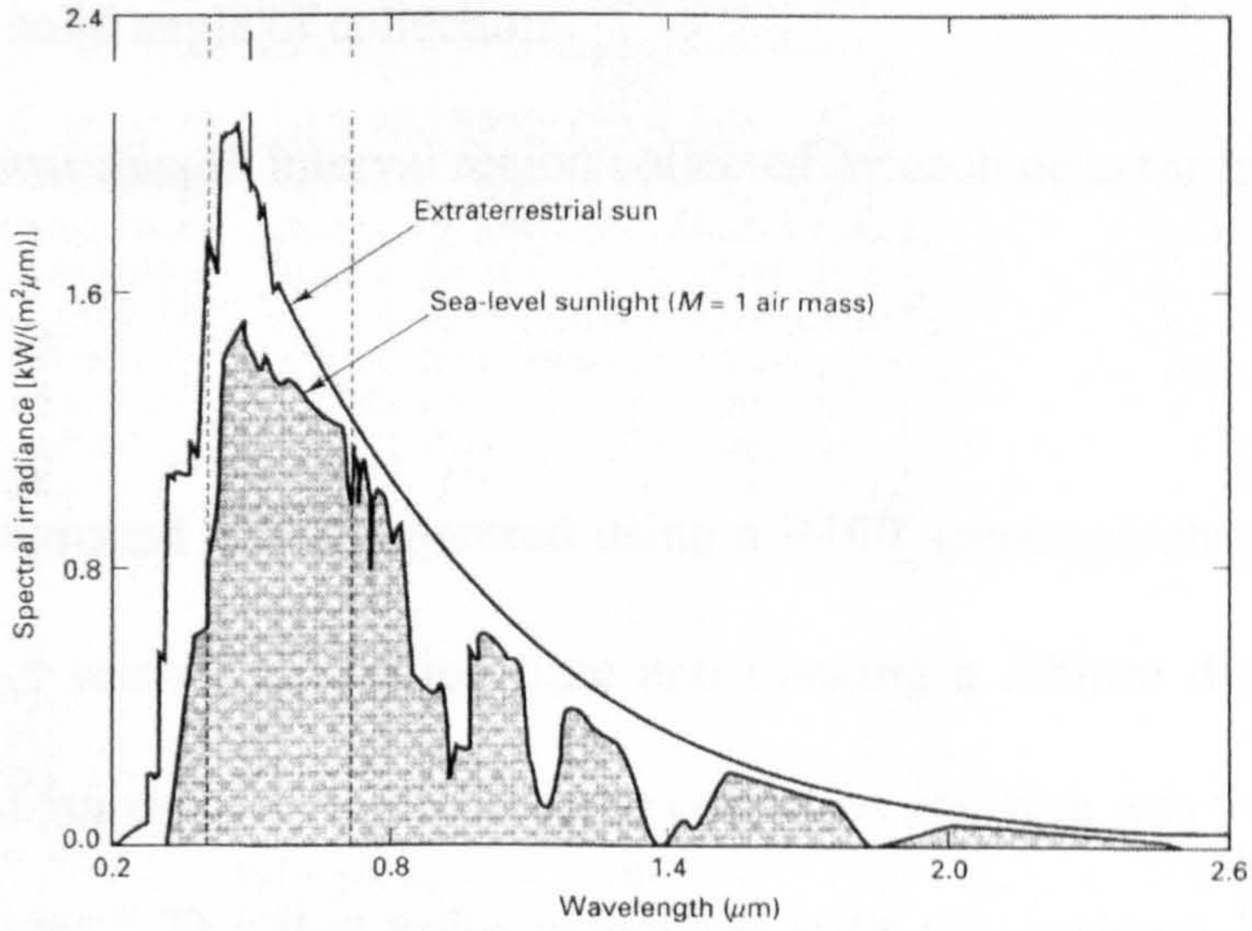

Figure 5.10 Spectral Solar irradience distribution

Data obtained at sea-level, on a clear day, with the sun at Zenith

In the spectral interval detected by the spectrograph, the spectral solar irradience is approximately 1.4kW/m^2/μm. The worst-case example of ambient light interference occurs, when sunlight reflects off a 100% diffusely reflecting sample (approximating a Lambertian source). The signal level, was determined using equation 5.5.

$$n = \frac{\iiint \frac{I_{532}}{\pi} dA d\Omega d\lambda}{\eta_{532}}$$

where

I_{532} is the solar irradience at 532nm

η_{532} is the conversion factor from photons into counts at 532nm

dA is the area imaged by the instrument

dΩ is the solid angle of collection

dλ is the wavelength interval region collected by each detector pixel

5.5

The ambient background signal measured using a R100 spectrograph with 0.25nm per pixel dispersion, 1 second integration time and imaging a 500μm diameter spot size from a distance of 5m using a 75mm diameter collection aperture was found to be $2x10^7$ photoelectron counts. The shot noise associated with this ambient background was found to be $3x10^3$ photoelectron counts. It is a property of an imaging spectrograph that multiple channels can be sampled simultaneously using independent optical fibres imaged by independently addressed regions of the CCD. This allows a background signal to be measured using a second optical fibre mounted in the detector head, to image an off-axis, non-excited, point in the sample and subtracted from the SERRS spectrum numerically.

The graph in figure 5.11 illustrates the theoretical signal-to-noise ratio of the detector as the stand-off distance is increased. The graph of the signal-to-noise ratio, obtained using the 75mm, CCTV lens was curve-fitted using the allometric function, $SN(d) = SN_0 d^{-y}$ (Origin, 6.1) for both the laboratory-ambient lighting and absolutely dark curves. The resulting curve-fit parameters are shown in table 5.1.

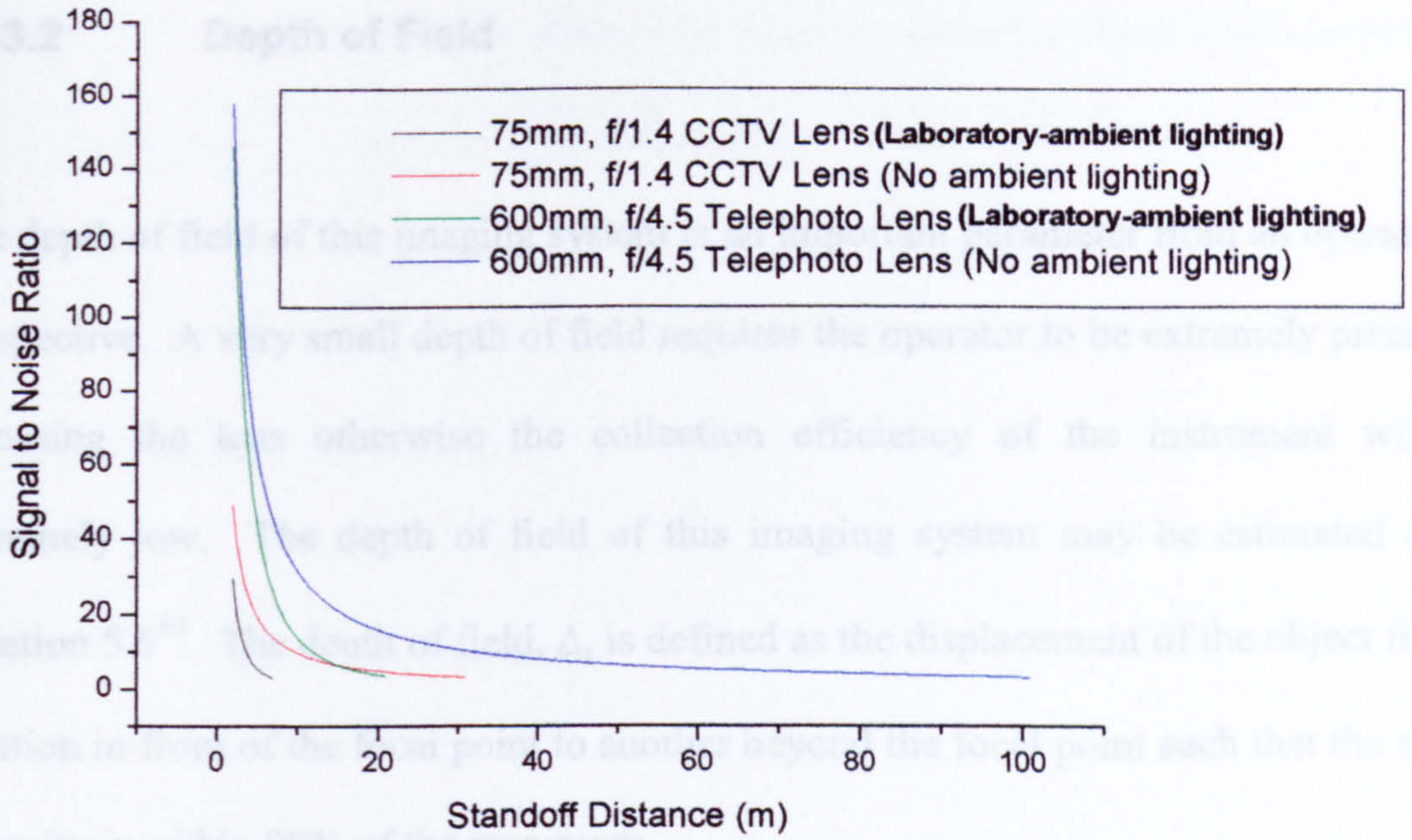

Figure 5.11 Graphical Determination of Maximum Standoff Distance

Table 5.1 Curve-fit Parameters for f/1.4, 75mm camera lens collection

Condition	SN_O	y
Ambient laboratory lighting	102±1.65	-1.79±0.01
Absolute Dark	98.1±0.11	-1.00±0.01

As an estimate of system performance, the experimentally observed values should lie within these two limits.

5.3.2 Depth of Field

The depth of field of this imaging system is an important parameter from an operational perspective. A very small depth of field requires the operator to be extremely precise in focussing the lens otherwise the collection efficiency of the instrument will be extremely low. The depth of field of this imaging system may be estimated using equation 5.6[10]. The depth of field, Δ, is defined as the displacement of the object from a position in-front of the focal point to another beyond the focal point such that the signal intensity is within 90% of the maximum.

$$\Delta = \frac{2\left(\frac{u}{D}\right)\sqrt{\frac{A}{\pi}}u(u-f)f^2}{f^4 - \left(\frac{u}{D}\right)^2\left(\frac{A_1}{\pi}\right)^2 u^2} \qquad 5.6$$

The effect of varying the focal length and the optical fibre connector are summarised in table 5.2. The use of a low numerical aperture optical fibre reduces the depth of field considerably. Reducing the focal length of the camera length increases the depth of field of the lens.

Table 5.2 Projected Depth of Field for Various Detector Head Configurations

Focal length (mm)	Aperture Diameter (mm)	Depth of Field (mm)
600	133	21.3
300	53.7	115
75	41.7	490

where d=0.0625mm; s_0=4000mm;

5.4 Signal Processing

The intended user of this instrument was not expected to be conversant in the use of spectroscopy. The instrument was required to present no data to the operator, other than the serial code of the sample identified. With this in mind, the spectra obtained by the instrument were processed to reduce noise and then matched to reference spectra in a library file.

The recognition of spectra was achieved using the 1st derivative correlation algorithm. This is a proprietary algorithm, supplied by Galactic Industries. Derivitising the spectra first, reduces the presence of background levels, that are present under varying background ambient lighting. Both the unknown and the library data are centred about their respective means before the vector dot products are calculated according to equation 5.7

$$HQI = 1 - \frac{(Lib_m \bullet Unkn_m)^2}{(Lib_m \bullet Lib_m)(Unkn_m \bullet Unkn_m)}$$

where $Lib_m = Lib - \frac{\sum_{i=1}^{n} Lib_i}{n}$ and $Unkn_m = Unkn - \frac{\sum_{i=1}^{n} Unkn_i}{n}$

5.7

Where Lib_i, $Unkn_i$ are the data elements from the library reference and sampled spectra. In the case where the signal-to-noise ratio and baselines in the library and the unknown spectra are similar, the mean values will be effectively the same. However, the mean-centring step makes the Hit Quality index independent of spectra normalisation. If the spectrum is noisy, or there are sharp negative dips in the spectrum (i.e., water vapor, CO_2, etc.), they will be normalized to 0. This causes the baseline in the unknown to be normalized to a value significantly greater than 0. Therefore, the library spectrum and unknown spectrum will not match very well, and incorrect hits will be given. By centring each spectrum about its mean, this problem is avoided.

5.5 Methodology

The apparatus was set-up as shown in figure 5.12 in a darkened laboratory. An f/1.4, 75mm CCTV lens (Pulnix, C25011IR) was coupled to a Renishaw Raman System 100 Analyser using a pair of 0.275NA, 62.5 μm, multi-mode optical fibres, (Fiberguide, Anhydroguide UV/VIS 62.5/125). A 532nm long-pass filter, (Barr Associates) was

positioned in front of the optical fibres at normal incidence to attenuate elastically scattered light from the sample.

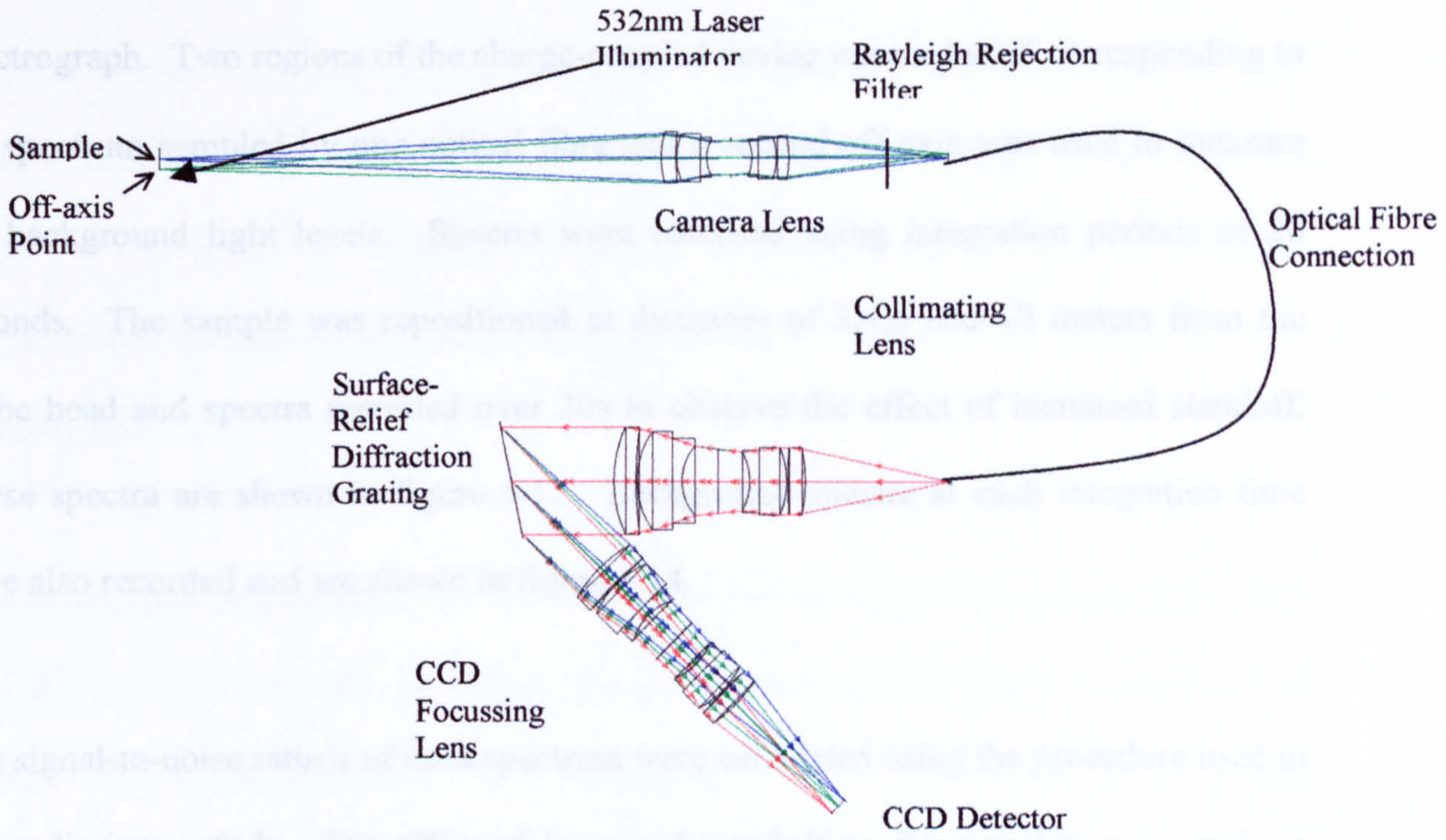

Figure 5.12 Ray trace of Detector Head Set-up (Not to Scale)

The SERRS substrate was used to coat a microscope slide, which was positioned at a standoff of 2 meters from the camera lens front surface. A target was etched into the microscope slide such that measurements could be acquired from approximately the same point. Focussing onto the sample was achieved by passing a Helium-Neon

(Spectra Physics) 632.8nm wavelength laser through the probe optical fibre in reverse and focussing the laser to the tightest possible spot at the sample. Two 532nm wavelength diode laser pen pointers (B&Wtek, BWL-3) were then oriented such that they illuminated the substrate within the focussed Helium-Neon spot. The alignment laser was then disconnected from the probe head, which was then reconnected to the spectrograph. Two regions of the charge-coupled device were selected corresponding to the spectrum sampled by one optical fibre and a second off-axis area used to measure the background light levels. Spectra were recorded using integration periods of 20 seconds. The sample was repositioned at distances of 3,4,6 and 10 meters from the probe head and spectra recorded over 20s to observe the effect of increased standoff. These spectra are shown in figure 5.13. Background spectra at each integration time were also recorded and are shown in figure 5.14.

The signal-to-noise ratio's of each spectrum were calculated using the procedure used in the preliminary study. The effect of increased standoff on the signal-to-noise ratio is shown in figure 5.15. The relationship between signal and the standoff distance was modelled using the allometric relationship, (Origin, 6.1) $SNR(d) = SNR_{0(2m)} d^{-y}$, where $SNR_{0(2m)}$ is the signal to noise ratio at 2m and y is the decay constant of the curve.

A variety of commercially available camera lenses were then used to evaluate the variation in signal-to-noise level at 10m standoff using the same sampling conditions. The lenses used are shown in table 5.3. The recorded spectra are shown in figure 5.16.

Table 5.3 Summary of Commercially Available Camera Lenses

Camera lens	Focal length (mm)	F-Number	Aperture Diameter (mm)
Mamiya	300	5.6	53.6
Canon	600	4.5	133.3
Pentax	75	1.4	41.7

The relationship between the signal-to-noise ratio and the signal observed at each standoff distance from the camera lens is shown in figure 5.17 using log-log axes. The slope of the graph is 0.52±0.03, showing a near shot-noise limited detection performance. A shot-noise limited detection performance would be represented by a slope of 0.5.

The sample was then repositioned at a distance of 5m and then stepped along the optical axis at small intervals with 10 second spectra recorded at each interval to provide an estimate of the depth of focus of the imaging system. The signal level of each spectrum, normalised to the focus intensity, was plotted against displacement from focus and shown in figure 5.18.

The use of the first-derivative correlation algorithm was then investigated using the spectra acquired at each standoff distance with the reference spectrum shown in figure 5.19. At the time there was only one SERRS dye available and so the effect on mixtures analysis was not investigated.

In this experiment, the shot-noise associated with an ambient background and the SERRS-characteristic, inelastic-background predominates over detector read-noise. The analyte spectra are well categorised and the relative intensities of the analyte peaks do not vary greatly between spectra[9]. In each spectrum, only the background intensity is expected to vary under different ambient lighting conditions, which may be removed by taking a first derivative of the spectrum. Maximum-likelihood Poisson's-noise reduction statistical methods have been reported[10] to improve the signal-to-noise ratio of a weak spectrum given a-priori knowledge of the instrument point spread function and the sample spectrum. The use of a maximum-likelyhood Poisson's noise reduction technique (Spectrum Square Associates Inc., US) was employed to investigate the potential improvement in signal-to-noise ratio and the potential for extended standoff range. The signal-to-noise ratio of the analyte spectrum obtained at shown in figure 5.16 was processed with the a-priori reference spectrum shown in figure 5.9. The resultant processed spectrum is overlaid in figure 5.19.

5.6 Results

5.6.1 Signal Levels

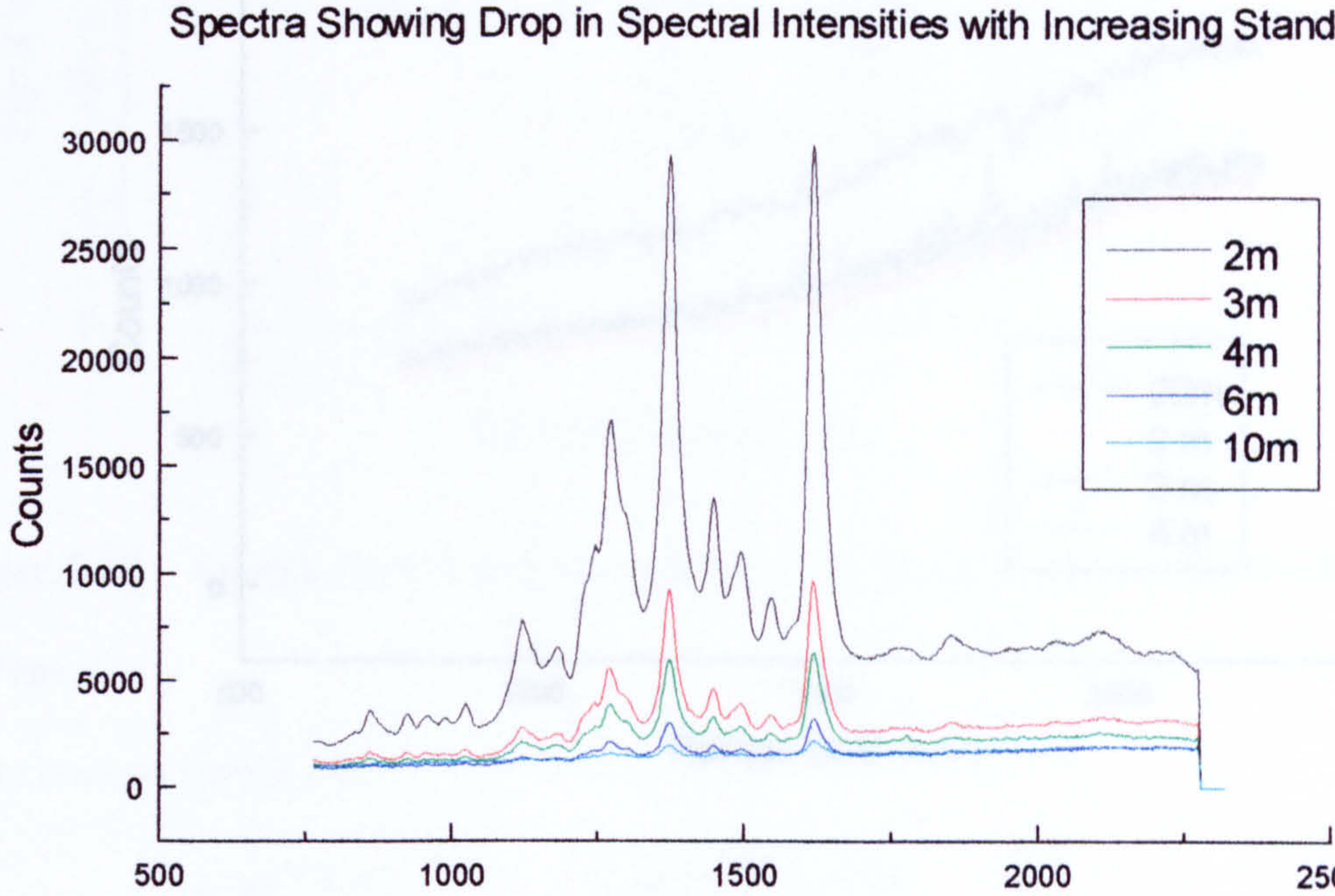

Figure 5.13 Graph Showing Effect on Spectral Intensities as Standoff is Increased

Experimental Conditions

Excitation: 3.6mW at 532nm.

Acquisition Time: 20 s

Instrument: Renishaw System 100

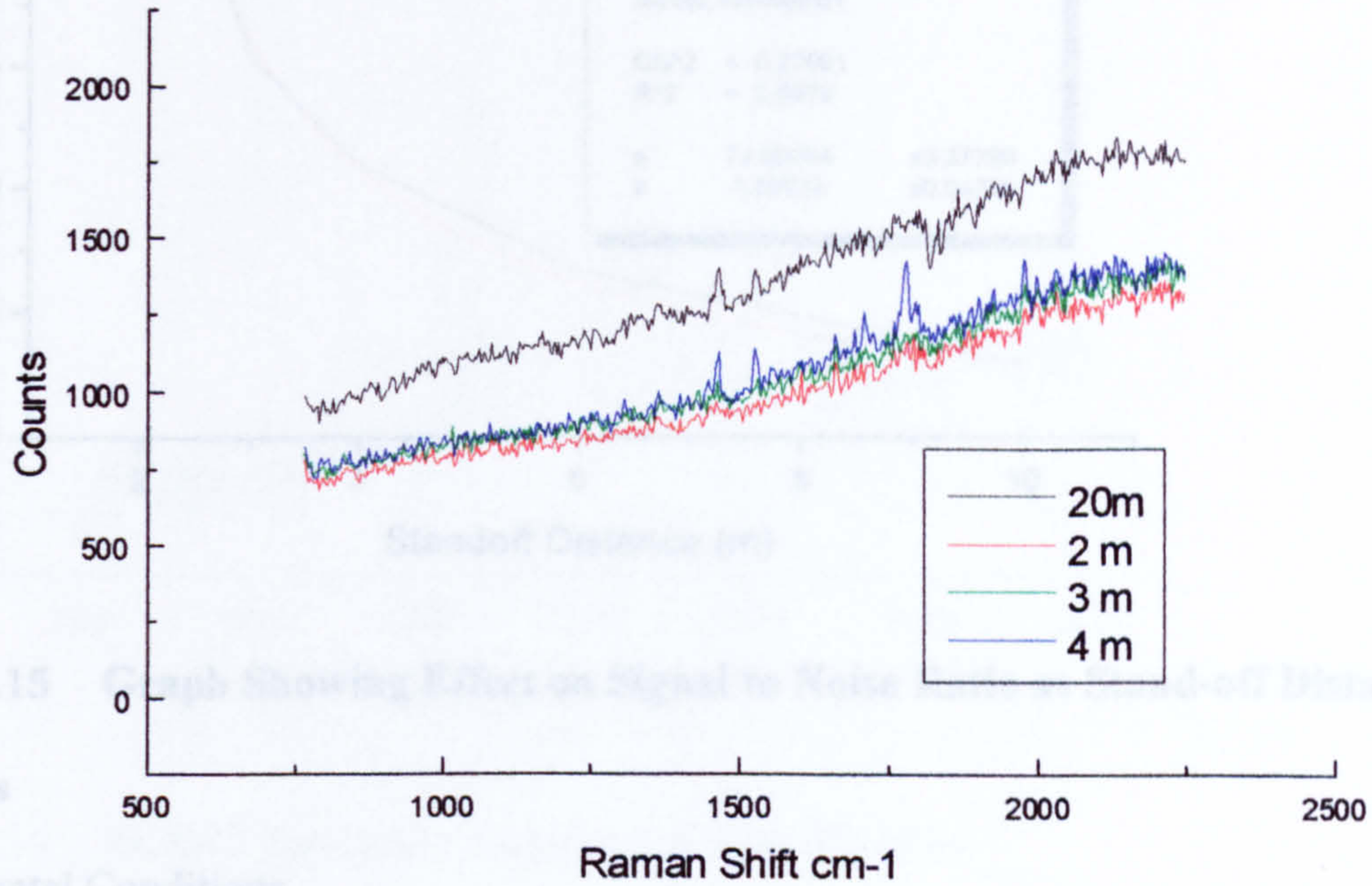

Figure 5.14 Spectra showing Effect of Increased Standoff on Ambient Background

(Peaks shown at long standoff due to fluorescent room lighting)

Integration Time: 20 s

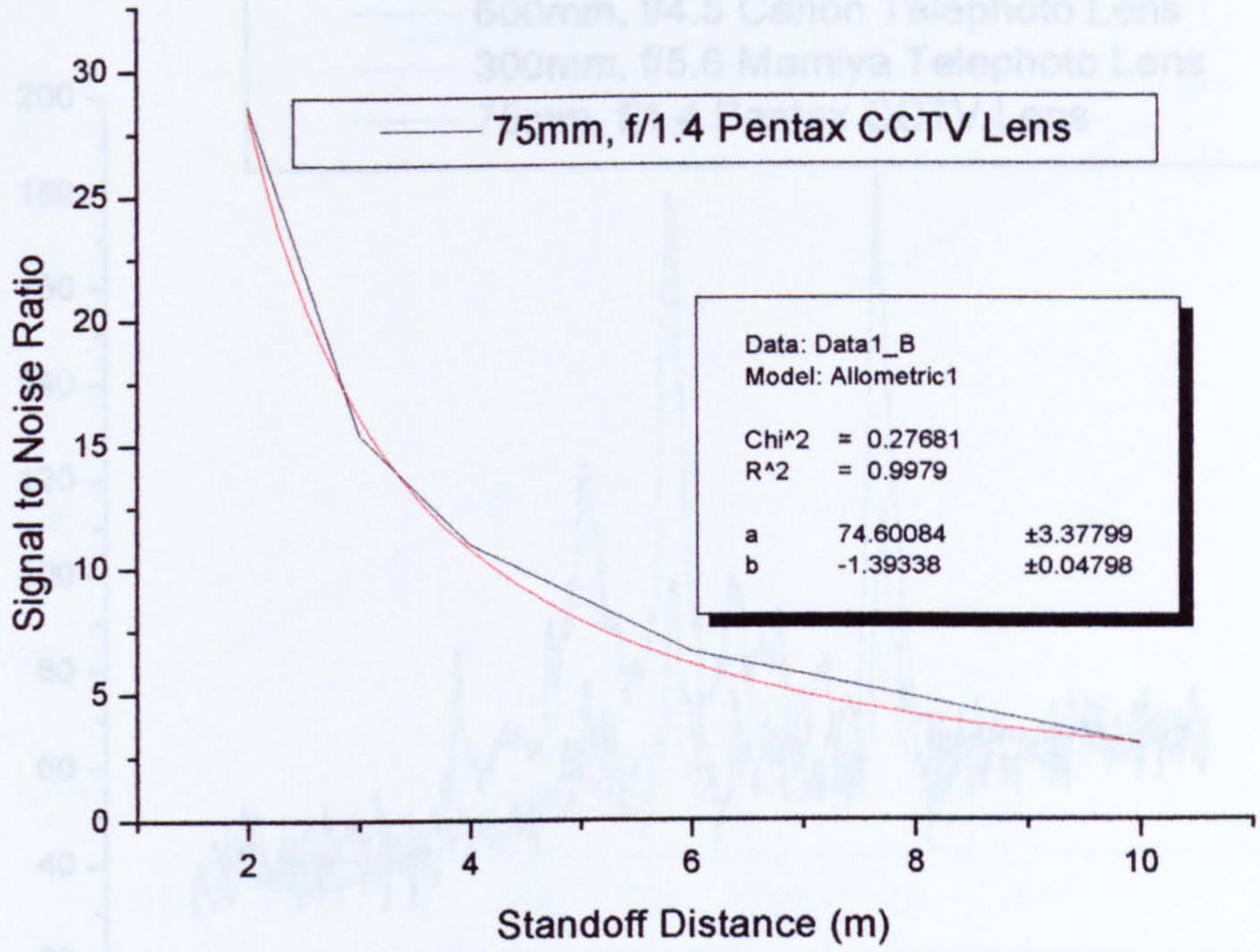

Figure 5.15 Graph Showing Effect on Signal to Noise Ratio as Stand-off Distance Increases

Experimental Conditions

Excitation:	3.6mW at 532nm.
Acquisition Time:	20 s
Instrument:	Renishaw System 100

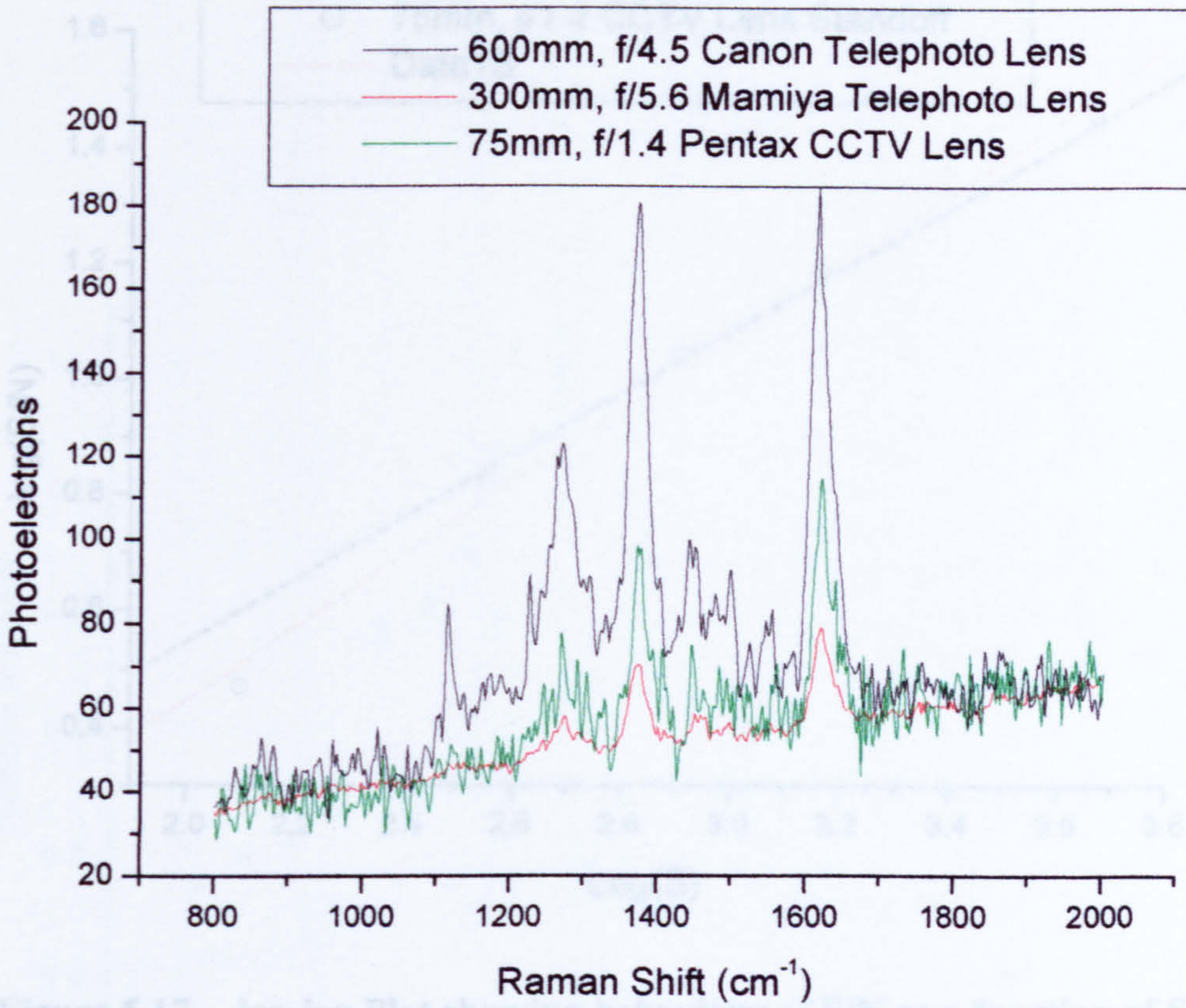

Figure 5.16 SERRS Spectrum Acquired at 10m Standoff

Experimental Conditions

Standoff Distance	10m
Power at Sample	3.6mW
Acquisition Time:	1s
Instrument:	Renishaw System 100

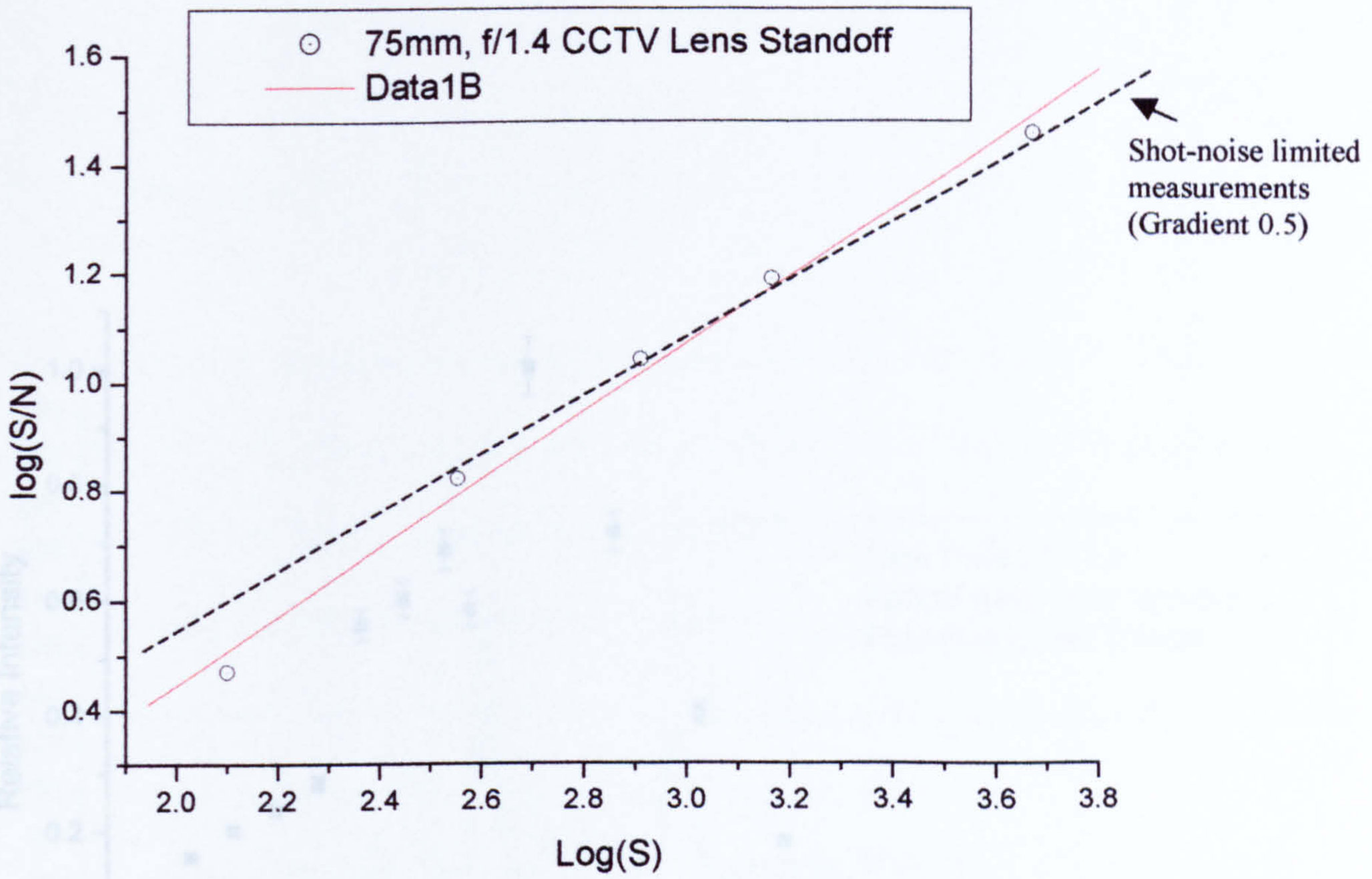

Figure 5.17 log-log Plot showing behaviour of S/N as a function of Signal

Linear Regression for Data1_B:

Y = A + B * X

Parameter	Parameter Value	Error
A	-0.80017	0.09364
B	0.52375	0.03197

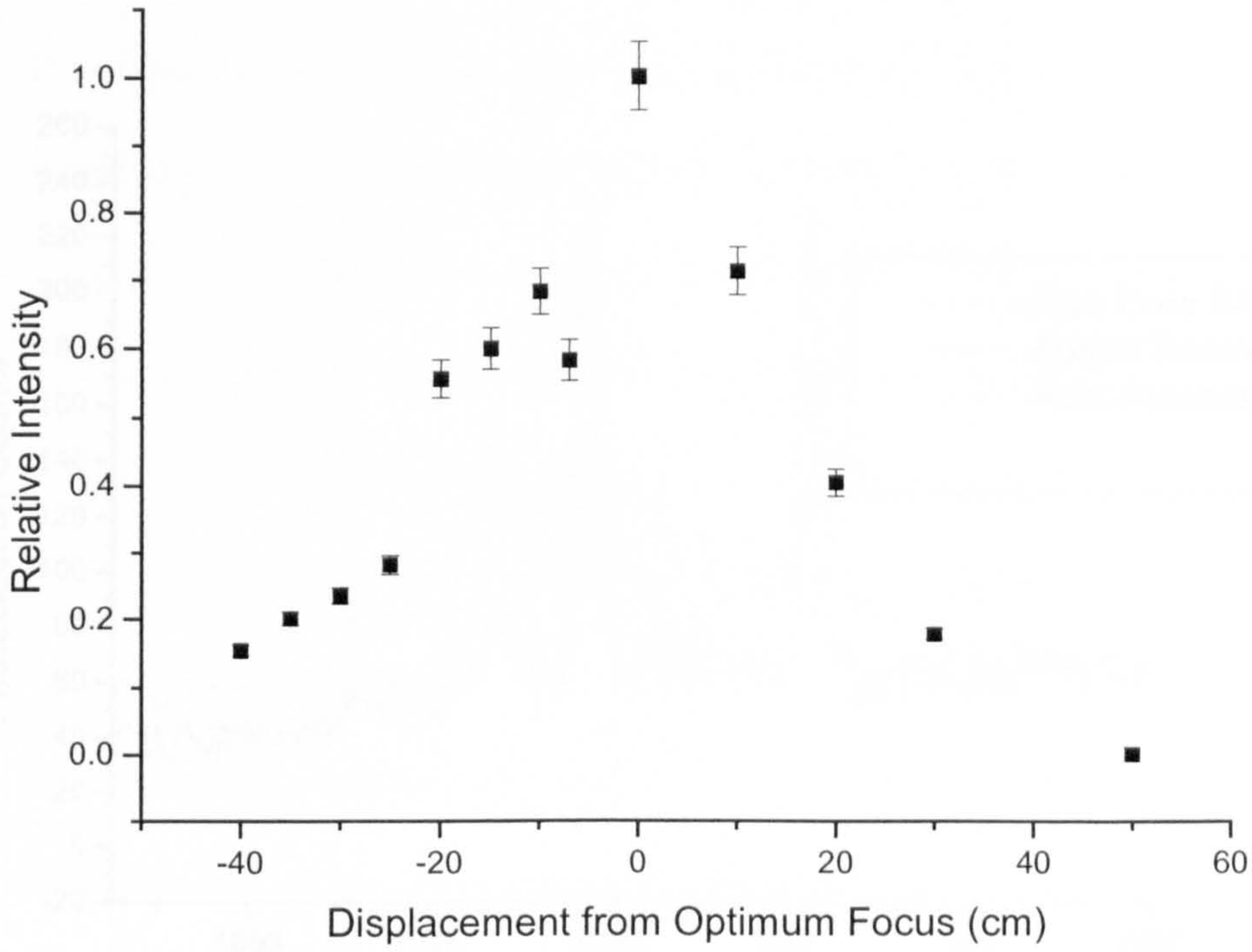

Figure 5.18 Effect of Sample Displacement from Focal Point on Signal Intensity

Experimental Conditions

Acquisition Time: 1 s

Instrument: Renishaw System 100 with 75mm, f1.4 lens

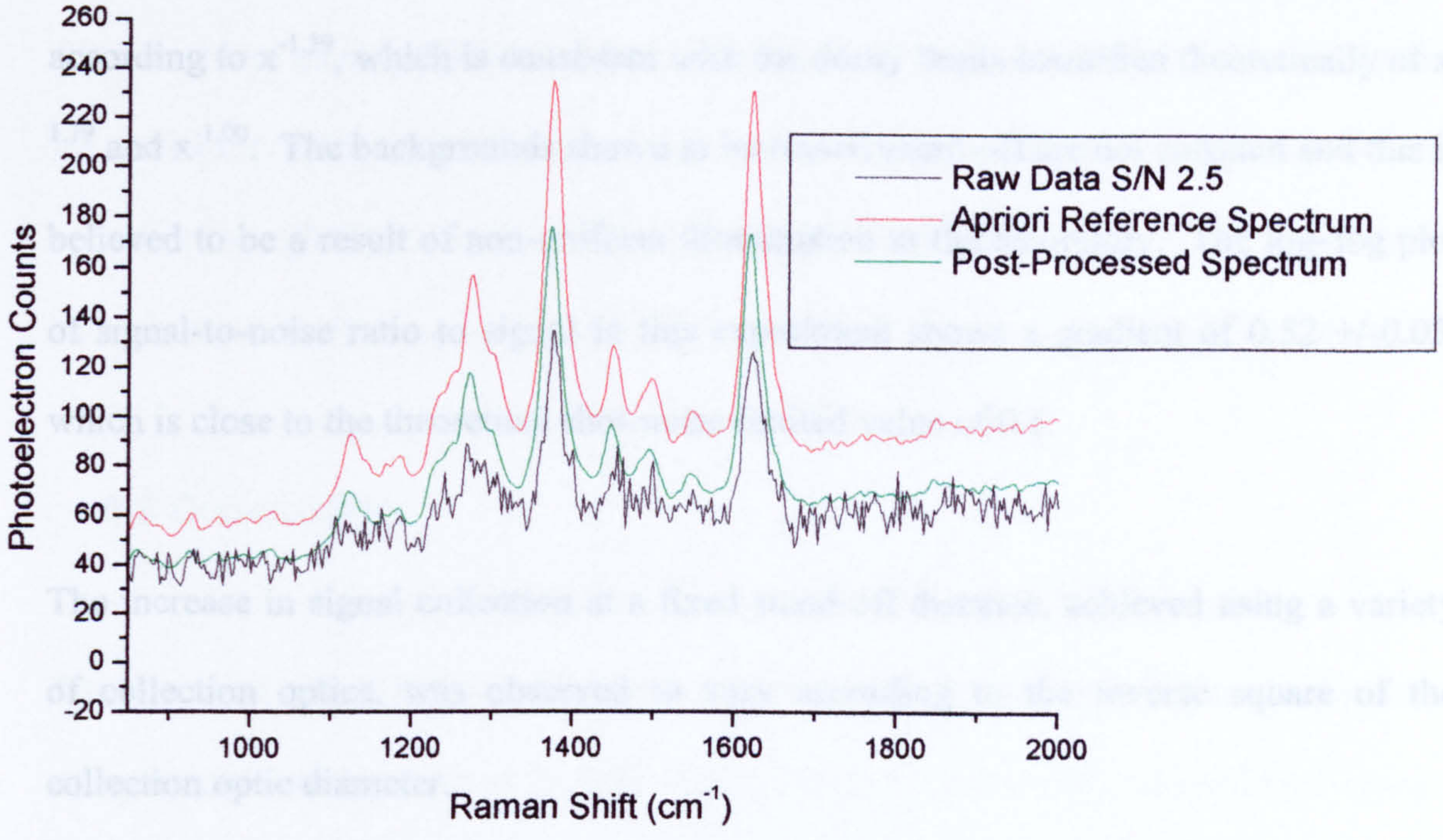

Figure 5.19 Signal to Noise Improvement using Bayesian Methods

5.7 Discussion

The reduction in signal-to-noise ratio at increasing levels of standoff was found to fall according to $x^{-1.39}$, which is consistent with the decay limits identified theoretically of $x^{-1.79}$ and $x^{-1.00}$. The backgrounds shown at increased stand-off are not constant and this is believed to be a result of non-uniform illumination in the laboratory. The log–log plot of signal-to-noise ratio to signal in this experiment shows a gradient of 0.52 +/-0.03, which is close to the theoretical shot-noise limited value of 0.5.

The increase in signal collection at a fixed stand-off distance, achieved using a variety of collection optics, was observed to vary according to the inverse square of the collection optic diameter.

In each instance, the hit-quality index used to compare the spectra with the reference spectrum was greater than 0.87, indicating an excellent match, even at the low signal-to-noise ratios collected at long standoff. An absolute limit to the performance of the hit quality index was not identified. The use of maximum likelihood methods to reduce the intensity of shot-noise in the spectrum and thus increase the signal-to-noise for weak spectra was found to be improved by a factor of 10.

The use of visible excitation at a wavelength so close to the optimum sensitivity of the human eye, 555nm, is an issue that requires address if this instrument were to be utilised

in a covert environment. It is envisaged that an alternative SERRS dye substrate will be developed, requiring excitation in the infra-red, thus moving out of the human eye's responsivity, but within the detectable region of a silicon-CCD. The 532nm long-pass filter could be easily replaced with a near-infrared long-pass filter at 785nm or 850nm for excitation at these wavelengths. The anti-reflection coatings present on most high specification telephoto camera lenses are suitable for use in the near infrared and shouldn't necessitate expensive proprietary coatings.

5.8 Conclusions

The detection of a SERRS substrate was achieved at a standoff distance of 5 metres, using an excitation power of 3.0mW within a single one second accumulation using a 532nm, pulsed laser pen pointer and an f/1.4, 75mm, CCTV camera lens coupled to a Renishaw System 100 using a multi-mode optical fibre. Signal levels acquired are in general agreement with modelled preliminary data. Minimum signal to noise levels were defined by that of the weakest peak at 1445cm^{-1} and at 5m under low-ambient lighting were approximately 10.6:1 with the predominant noise source arising from background-derived shot noise. As expected this value decreases with stronger room lighting.

5.9 References

1. *Public Consultation on Draft Code of Practice on Covert Surveillance.* Section 71 3(a) of Regulation of Investigative Powers Act 2000, Home Office, UK

2. M. Wu, M. Ray, Applied Spectroscopy, 2000, Volume 54, p 800.

3. H.T. Skinner, T.T.Cooney, S.K Sharma, and S.M. Angel, Applied Spectroscopy, 1996, Volume 50, pp 1007 – 1014.

4. T.F. Cooney, H.T. Skinner, S.M. Angel, Applied Spectroscopy, 1996, Volume 50, pp 836-848.

5. T.F. Cooney, H.T. Skinner, S.M. Angel, Applied Spectroscopy, 1996, Volume 50, pp 849-860.

6. W.S. Sutherland, J.P. Alarie, D.L. Stokes, T. Vo-Dinh, Instrumentation Science Technology, 1994, Volume 22, p 231.

7. H.S. Sands, I.P. Hayward, T.E. Kirkbride et al, Journal of Forensic Science, 1998, Volume 43, pp 509-513.

8. A. MccAbe, First Year Thesis Report, Strathclyde Inorganic Chemistry Dept., 2000.

9. I.P. Hayward, T.E. Kirkbride, D.N. Batchelder et al, Journal of Forensic Science, (Sep 1995), Volume 40 (5), pp 883-884.

10. P.A. Jansson, *Deconvolution; with applications in Spectroscopy*, Academic Press, Inc, New York, USA, 1984.

11. F.L. Pedroti, S.J. Pedroti, *Introduction to Optics. Second Edition,*Prentice-Hall International, Inc, London, UK, 1987.

Appendix A

Renishaw RA 200 Forensic Raman Analyser

A.1 Overview

The instrument shown in figure A.1 is the Renishaw RA200 Forensic "Raman-in-a-suitcase" Analyser which was developed as part of this Ph.D and marketed as a concept demonstrator in Pittcon, 2000, South Africa, Japan and Australia by Renishaw Spectroscopy Products Division, UK.

The instrument combines an air-cooled 300mW, 785nm wavelength near-infrared laser with a hand-held probe for screening packages suspected of containing explosives or narcotics. Sampling options are increased by the addition of a class 1 sampling chamber, preventing the need for an operator to wear protective goggles. Both sampling options are linked fibre optically.

The instrument achieves a spectral resolution of $8cm^{-1}$ over a range of $2000cm^{-1}$ (600-$2600cm^{-1}$) encompassing the fingerprint region of most illicit materials. Instrument calibration is achieved using an internal Neon-calibration source.

Detection of Raman scattered flux is achieved using optics optimised for the near-infrared and a deep depletion CCD detector.

Sampling simply requires the operator to strike a single key on an attached laptop PC (not shown). The laptop records the spectrum and operates a spectral correlation algorithm to match the sample to a library of forensically relevant materials. Typical sampling times are of the order of 0.5-1s.

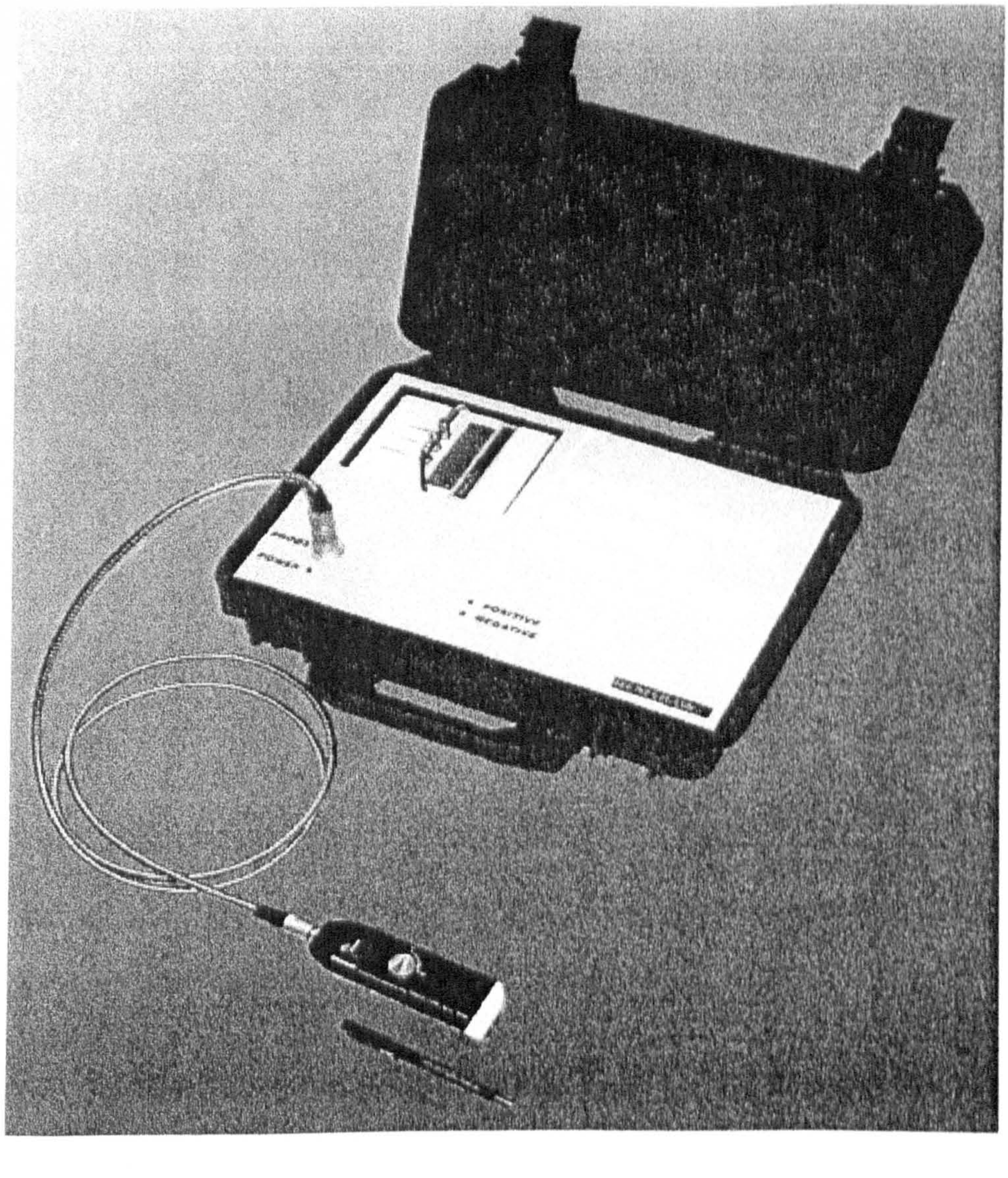

Figure A.1 Renishaw RA200 Forensic Raman Analyser